Time resolved transverse and longitudinal phase space measurements at the high brightness photo injector PITZ

Dissertation
zur Erlangung des Doktorgrades
des Departments Physik
der Universität Hamburg

vorgelegt von
Dmitriy Malyutin
aus Salair

Hamburg

2014

Gutachter der Dissertation:	Prof. Dr. Jörg Roßbach PD Dr. Bernhard Schmidt
Gutachter der Disputation:	Prof. Dr. Jörg Roßbach Dr. Frank Stephan
Datum der Disputation:	19.08.2014
Vorsitzende/Vorsitzender des Prüfungsausschusses:	Prof. Dr. Michael A. Rübhausen
Vorsitzender des Promotionsausschusses:	Prof. Dr. Daniela Pfannkuche
Leiterin de Departamens Physik:	Prof. Dr. Peter Hauschildt
Dekan der Fakultät für Mathematik, Informatik and Naturwissenschaften:	Prof. Dr. Heinrich Graener

Abstract

Short wavelength, high intensity Free Electron Lasers (FELs) require a high brightness electron beam, i.e. the beam should have small transverse and longitudinal sizes, small divergence and energy spread and high peak current. Therefore, the detailed characterization of the beam is required.

The Photo Injector Test facility at DESY, Zeuthen site (PITZ), was established as a test stand of the electron source for Free electron Laser in Hamburg (FLASH) and the European X-ray Free Electron Laser (XFEL). The PITZ beamline consists of various types of diagnostic devices for the detailed bunch characterization. Mainly, the transverse phase space characterization is performed at PITZ, but longitudinal phase space measurements are also of great importance for full characterization of high brightness electron bunches from the photo injector.

One of the ways to measure the longitudinal phase space of electron bunch is an RF deflector. It deflects particles transversely with respect to the movement direction of the bunch in a linear dependence on their longitudinal coordinates within the bunch. As a result it gives the possibility to perform measurements of the bunch longitudinal properties in combination with a following transverse beam characterization. Using additionally a dispersive section the longitudinal phase space can be obtained as well.

Another approach to measure the longitudinal phase space of the bunch is a tomographic method based on measurements of the momentum spectra while varying the electron bunch energy chirp. The energy chirp at PITZ can be applied and changed by varying the RF phase of the CDS booster – the accelerating structure installed downstream the gun. The resulting momentum distribution can be measured with a dipole spectrometer downstream. As a result, the longitudinal phase space at the entrance and exit of the CDS booster can be reconstructed over a wide range of bunch charges.

In this thesis both methods for longitudinal phase space measurements are described in detail. Measurement techniques are introduced. Numerical simulations of the measurements are performed and studied. Results of the first longitudinal phase space measurements at PITZ using the tomographic technique are presented.

Zusammenfassung

Höchstintensive Freie Elektronen Laser (FEL) für kurze Wellenlängen benötigen einen hochbrillanten Elektronenstrahl, das heißt, der Strahl sollte eine geringe transversale und longitudinale Größe haben. Er muss eine kleine Divergenz, eine schmale Energieverteilung sowie einen hohen Spitzenstrom besitzen. Zur Überprüfung des geforderten Eigenschaften ist eine detaillierte Charakterisierung des Strahls notwendig.

Der Photoinjektor Teststand bei DESY, Standort Zeuthen (PITZ), wurde als Teststand für die Elektronenquellen des Freien Elektronen Lasers in Hamburg (FLASH) und des European X-ray Free Electron Lasers (XFEL) eingerichtet. Er enthält verschiedene Diagnosegeräte für die detaillierte Charakterisierung von Elektronenpaketen. Schwerpunkt der Untersuchung ist die Charakterisierung des transversalen Phasenraums. Aber auch die Untersuchung des longitudinalen Phasenraums ist vor großer Bedeutung.

Eine Methode den longitudinalen Phasenraum von Elektronenpaketen zu messen basiert auf einem HF-Deflektor. Dieser lenkt Teilchen transversal zu ihrer Bewegungsrichtung ab, und zwar in linearer Abhängigkeit von ihrer longitudinalen Position im Paket. Damit ist die Möglichkeit zur Messung von longitudinalen Eigenschaften der Elektronenpakete gegeben, die mit einer nachfolgenden transversalen Strahlcharakterisierung kombiniert werden kann. Zusätzlich kann mit einer Elektronenspektrometers des longitudinalen Phasenraums gemessen werden.

Eine weitere Möglichkeit zur Messung des longitudinalen Phasenraums der Elektronenpakete ist die Tomographie. Sie beruht die auf der Messung des Impulsspektrums des Elektronenstrahls bei unterschiedlicher Energie-Zeit Abhängigkeit. Bei PITZ kann eine Energie-Zeit-Abhängigkeit durch Variierung der HF-Phase des Nachbeschleunigers (CDS booster) kontrolliert auf den Elektronenstrahl eingeprägt werden. Daher wird die durch eine Veränderung der HF-Phase der Nachbeschleunigerkavität die Energie-Zeit-Abhängigkeit des Elektronenstrahls verändern. Die daraus resultierende neue Impulsverteilung wird mit einem Dipolspektrometer gemessen werden. Auf diese Weise kann der longitudinale Phasenraum am Eingang und Ausgang des Nachbeschleunigers über einen weiten Bereich der Ladung der Elektronenpakete rekonstruiert werden.

In dieser Arbeit werden beide Methoden zur Messung des longitudinalen Phasenraums detailliert beschrieben und neue Messtechniken werden vorgestellt. Die numerischen Simulationen der Messungen wurden durchgeführt. Die Resultate von Messungen des longitudinalen Phasenraums, die bei PITZ zum ersten Mal mit Hilfe der Tomographietechnik durchgeführt wurden, werden in dieser Arbeit dargestellt.

Contents

List of acronyms:

ART……...Algebraic Reconstruction Algorithm

ASTRA……...……...A Space Charge Tracking Algorithm

BPM……..... Beam Position Monitor

BSA……... Beam Shaping Aperture

CCD…….. Charge-Coupled Device

CDS…….. Cut Disk Structure

DCM……. Dark Current Monitor

EMSY……Emittance Measurement SYstem

FC……. Faraday Cup

FEL……Free Electron Laser

FLASH…….. Free electron LASer in Hamburg

FWHM…….. Full Width at Half Maximum

HEDA……High Energy Dispersive Arm

ICT…… Integrating Current Transformer

LEDA…… Low Energy Dispersive Arm

MENT……... Maximum ENtropy Technique

MMMG……. Maximum Mean Momentum Gain

OSS……... Optical Sampling System

OTR…….. Optical Transition Radiation

PITZ…….. Photo Injector Test facility at DESY, Zeuthen site

PST…… Phase Space Tomography

RF……. Radio Frequency

RMS…….. Root Mean Square

TDS……... Transverse Deflecting Structure

XFEL…….X-ray Free Electron Laser

YAG…….. Yttrium Aluminum Garnet

Chapter 1

Introduction

In the last years the accelerator community working on synchrotron and Free Electron Laser (FEL) band light sources has focused on maximizing the electron beam brightness, i.e. the number of the charged particles per unit volume in the six-dimensional phase space of the beam. Such high brightness electron beams serve for the production of high intensity, high brightness synchrotron and FEL light, which can be used, for example, to see atomic details of viruses, make a film of chemical reactions or study matter under extreme conditions.

The sources of synchrotron radiation can be characterized by their brilliance or spectral brightness. Brilliance is defined as the number of photons, emitted by the source per time unit and in solid angle, per surface of the source, and in a bandwidth of frequencies around the given one. The units in which it is usually expressed are photons/s/mm^2/mrad^2/0.1% BW, where 0.1% BW denotes a bandwidth of $10^{-3} \cdot \omega$ centered at the frequency ω of the emitted light.

One of the possible ways to create a light source with a very high brilliance is a Free Electron Laser (FEL). In FELs the free ultra-relativistic electrons in vacuum are grouped in an electron bunch and pass through a structure with a periodical magnetic field, which is perpendicular to the moving direction (undulator). As a result, the electron bunch emits synchrotron radiation in forward direction. To amplify the light intensity an optical resonator based on two mirrors can be used for low photon wavelength. Subsequent electron bunches passing through the undulator, generate synchrotron light, and, as a result, the light stored in the optical resonator is amplified, what gives the Light Amplification by Stimulated Emission of Radiation (LASER). Such a type of accelerators is also called low gain FEL.

For wavelengths shorter than about 100 nm it is difficult to produce mirrors with high reflectivity which can be used for the optical resonator. Therefore, the FELs for such wavelengths should be realized as a single-pass high-gain machine. For this task a special regime of accelerator operation can be realized. The light, emitted by some part of the electron bunch, passing through the undulator, interacts with a part of the bunch ahead and causes an energy modulation of the electrons in the front, i.e. some electrons gain energy and some lose energy. This causes that the electron bunch going through the undulator with a sinusoidal trajectory experiences a micro-bunching inside the bunch. Within a so called coherence length these micro-bunches radiate coherently which causes a large amplification of the radiation since now the radiation power is proportional to the

number of particles involved squared. Such a specific process of the light emission from the electron bunch in the undulator is called Self Amplified Spontaneous Emission (SASE) [1]. An experimental demonstration of the SASE mechanism with a gain of $3 \cdot 10^5$ has been carried out in the infrared wavelength range in 1998 (see [2] and [3]).

For such an operation type of FEL however there are quite strong requirements on the electron beam quality at the undulator entrance: small transverse emittance, small energy spread and high beam peak current (high brightness). All this parameters are included in the normalized 6D beam emittance at given bunch charge. While this emittance cannot be decreased during transport and acceleration, the electron bunch must be well prepared already in the injector part of the accelerator, i.e. at the electron source.

The Photo Injector Test facility at DESY, Zeuthen Site (PITZ) was built as a test stand [4] for the electron sources for FLASH and the European XFEL [5]. A normal conducting L-band 1.6-cell copper gun cavity with a Cs_2Te photocathode produces 7 MeV electron bunches with up to 24 ps bunch length and up to several nC charge. Then the electrons are further accelerated by an accelerating structure to an energy of up to 27 MeV. Downstream the accelerating structure the PITZ beamline consists of different diagnostics for detailed measurements of the electron beam properties. Characterization of the electron bunch transverse phase space at PITZ is mainly done by a slit scan technique [6]. For electron bunch length measurements and longitudinal phase space measurements a streak camera system was used in the last years (see [7] and [8]) in the straight section and in dispersive sections, respectively. From a recently installed RF deflector a much better time resolution and new possibilities for studies of the bunch longitudinal properties compared to the streak camera measurements are expected. Additionally to the measurements with the RF deflector or with the streak camera, the electron bunch longitudinal phase space can be also measured with a tomographic technique [9]. This technique uses measured momentum distributions from the longitudinal phase space rotated by an accelerating structure. From the restored phase space the slice energy spread, the time-energy correlation and the beam current distribution can be extracted. In contrast to a measurement with the RF deflector and with the streak camera, this method is a multi-shot technique as the set of momentum distributions cannot be measured at ones.

The goal of this work is to study the possible ways of performing time resolved transverse and longitudinal phase space measurements with high resolution at the PITZ facility. These measurements would allow the full characterization of the low emittance, high brightness beams from an electron source like a photocathode gun. To perform time resolved measurements at a sub-picosecond scale an RF deflector, which is also called transverse deflecting structure (TDS), was installed at PITZ at the end of 2011. Due to safety limitations the delivered modulator of the RF system for the TDS could not be put into operation up to now and a new modulator is currently ordered. Therefore this

thesis has to concentrate on numerical studies of the implementation of the TDS at PITZ and on measurements of the longitudinal phase space at PITZ using tomographic technique.

In Chapter 2 of the thesis the basic beam dynamics is described. Phase space, emittance and Twiss parameters are introduced. The PITZ facility is shortly described in Chapter 3. The beamline components related to the thesis topic are described there in more detail. The basic principles of the measurements with RF deflectors are introduced in Chapter 4. Techniques for longitudinal phase space measurements, longitudinal profile measurements and transverse slice emittance measurements are introduced. The longitudinal resolution and its limitations are discussed. Simulations for all type of measurements are performed and results are presented in Chapter 5. This includes: longitudinal phase space measurements, bunch length and longitudinal profile measurements and transverse slice emittance measurements. The tomography method for longitudinal phase space measurement is described in Chapter 6. The algebraic reconstruction technique for tomography is introduced. The measurement technique for the longitudinal phase-space measurements is described. Simulations of the measurements with the tomographic technique are performed in Chapter 7. Experimental measurements at the PITZ facility are carried out for various electron bunch temporal profiles and charges and results are shown in Chapter 8. The strategy of the measurements and the varied machine parameters are presented. The data analysis procedure is introduced. The results are summarized in Chapter 9. Future measurements and plans are suggested and discussed.

Chapter 2

Beam dynamics

The force required to accelerate and bend a charged particle beam or to provide focusing to hold the particles close to the ideal path in an accelerator is known as the Lorentz force and is derived from electric and magnetic fields [10]:

$$\vec{F} = e\vec{E} + e\left[\vec{v} \times \vec{B}\right], \tag{2.1}$$

where e is the particle charge, $\vec{E}$ and $\vec{B}$ are the electric and magnetic field vectors, respectively, and $\vec{v}$ is the velocity vector of the particle. The basic formulation of beam dynamics relies only on linear fields which are independent or only linearly dependent on the distance of a certain particle from the ideal trajectory. Linear beam dynamics deals with the mathematical description of particle trajectories in the presence of linear fields only. The general task in beam optics is to transport charged particles from point A to point B along the design path.

In the following sections the equation of motion, phase space, beam emittance and transport matrix formalism will be described. They will be used in Chapter 4 to describe the working principles of an RF deflector and its applications. A model of the particle acceleration by an RF cavity will be presented here as well. It will be used to depict the tomographic technique for the longitudinal phase space measurements presented in Chapter 6.

2.1 Equations of motion

Considering the presence of only z-dependent magnetic fields $B_x(z)$ and $B_y(z)$ from dipole and quadrupole magnets, where z is the particles coordinate along the design trajectory, x is the horizontal transverse coordinate with respect to the design orbit and y is the vertical transverse coordinate, and absence of longitudinal field $B_z(z) = 0$ one obtains:

$$B_x(z) = -g(z) \cdot y, \tag{2.2}$$

$$B_y(z) = B_0(z) - g(z) \cdot x, \tag{2.3}$$

here the presence of only a vertical dipole field $B_0(z)$ and a quadrupole gradient $g(z)$ was considered. The equations of motion for a particle in such fields will have the following form [10]:

$$x'' - \left(k(z) - \frac{1}{\rho(z)^2}\right) \cdot x = \frac{1}{\rho(z)} \delta p, \tag{2.4}$$

$$y'' + k(z) \cdot y = 0, \tag{2.5}$$

where $\rho(z) = p_0/eB_0(z)$ is the Larmor radius and $k(z) = eg(z)/p_0$ is the normalized quadrupole gradient along the trajectory, p is the particle momentum, p_0 the design reference momentum and the relative momentum δp is:

$$\delta p = \frac{p - p_0}{p_0}. \tag{2.6}$$

For the particles having the design momentum $p = p_0$ the equations of motion are simplified:

$$x'' + K_x(z) \cdot x = 0, \tag{2.7}$$

$$y'' + K_y(z) \cdot y = 0, \tag{2.8}$$

where $K_x(z) = \frac{1}{\rho(z)^2} - k(z)$ and $K_y(z) = k(z)$. Eq. (2.7) and (2.8) are also known as Hill's equations of linear transverse particle motion.

A general solution for Eq. (2.7) for the particle motion in the x-plane can be written in the form [10]:

$$x(z) = \sqrt{\varepsilon \beta(z)}\, cos\, (\psi(z) + \psi_0), \tag{2.9}$$

where ε is the emittance (see section 2.1.1), $\beta(z)$ is so called the beta function, $\psi(z) + \psi_0$ is the betatron phase function at the current z position, ψ_0 is the betatron phase at initial position, $\psi(z)' \cdot \beta(z) = 1$ and an analogy solution exists for the y-plane.

The phase advance between two points z_0 and z_1 along the trajectory is expressed as the difference $\Delta\psi$ between the values of the betatron phase function at these two points and can be calculated as follows:

$$\Delta\psi = \psi(z_1) - \psi(z_0) = \int_{z_0}^{z_1} \frac{1}{\beta(z)} dz. \tag{2.10}$$

2.1.1 Beam emittance

Each particle of a beam can be represented as a point in the six-dimensional phase space (x, p_x, y, p_y, z, δp_z) at any point along the beamline. In the case when there is no coupling between the x and the y transverse planes and no coupling between the transverse and the longitudinal particle motion one can split the six-

dimensional phase space into three independent two-dimensional phase space planes (x, p_x), (y, p_y) and (z, δp_z). In the paragraphs that follow only the two-dimensional phase space will be considered, if not mentioned otherwise.

The beam emittance characterizes the volume in the phase space which is occupied by the beam. Its numerical value, multiplied by π, is equal to the area occupied by the beam in the phase space. The emittance, in the corresponding 2-d plane, is a measure of the transverse or longitudinal temperature of the beam and depends on the source characteristics of the beam or on effects like quantized emission of photons into synchrotron radiation and its related excitation and damping effects.

The definition of the RMS transverse emittance is:

$$\varepsilon_0 = \sqrt{\langle x^2 \rangle \langle x'^2 \rangle - \langle x x' \rangle^2}. \tag{2.11}$$

where x is the particles transverse coordinates, x' is the particles transverse divergences calculated as $x' = p_x/p_0$ and p_0 is the particles longitudinal momentum.

If the beam experiences acceleration during its propagation, the emittance described according to Eq. (2.11) is not conserved. For such cases the normalized transverse emittance can be introduced. The normalized RMS emittance is defined as RMS transverse emittance multiplied by $\beta_0\gamma_0 = p_0/mc$:

$$\varepsilon_n = \beta_0\gamma_0\varepsilon_0, \tag{2.12}$$

where $\beta_0 = v/c$, v is the particle speed, c is the speed of light, $\gamma_0 = = (1 - {\beta_0}^2)^{-1/2}$ is the relativistic Lorentz factor and m is the mass of the particle.

2.1.2 Phase space ellipse and Twiss parameters

Liouville's theorem states that under the influence of conservative forces the particle density in phase space stays constant [10]. It provides a powerful tool to describe the beam in the phase space. The knowledge of the area occupied by the particles in the phase space at the beginning of a beam transport line allows to determine the location and distribution of the beam at any other place along the transport line without the need to calculate the trajectory of every individual particle. All the particles in the phase space can be surrounded by an ellipse – the phase space ellipse, described by [10]:

$$\gamma x^2 + 2\alpha x x' + \beta x'^2 = \varepsilon, \tag{2.13}$$

where α, β, γ, and ε are the ellipse parameters, see Fig. 2.1. The area enclosed by the ellipse is the beam geometrical emittance ε defined by

$$\int_{ellipse} dx\, dx' = \pi\varepsilon, \tag{2.14}$$

while the parameters α, β, and γ determine the shape and orientation of the ellipse (see Fig. 2.1).

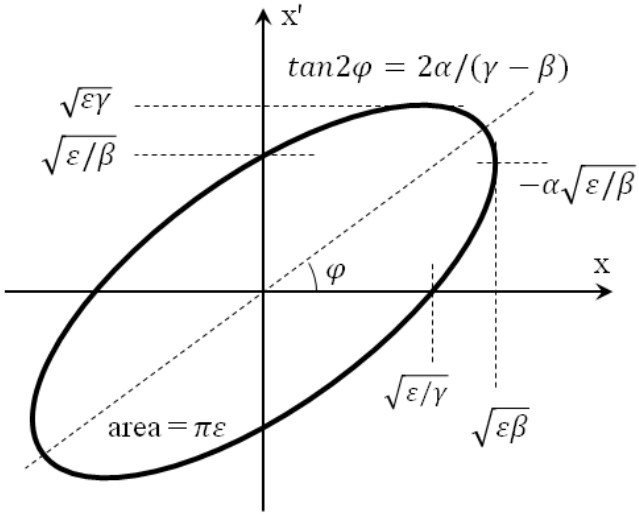

Fig. 2.1: Phase space ellipse and Twiss parameters [10]: β corresponds to the beta function, α corresponds to the alpha function and γ corresponds to the gamma function at the current longitudinal coordinate z.

The parameters α, β, and γ are known as betatron parameters, see Eq. (2.9), and also known as Twiss or lattice functions or Courant-Snyder parameters and the following equations are valid [10]:

$$\gamma\beta - \alpha^2 = 1, \tag{2.15}$$

$$\alpha(z) = -\frac{1}{2}\beta'(z), \tag{2.16}$$

The RMS beam size $\langle x^2 \rangle$, beam divergence $\langle x'^2 \rangle$ and covariance $\langle xx' \rangle$ can be calculated as follows [10]:

$$\langle x^2 \rangle = \varepsilon_0\beta, \tag{2.17}$$

$$\langle x'^2 \rangle = \varepsilon_0\gamma, \tag{2.18}$$

$$\langle xx' \rangle = -\varepsilon_0\alpha, \tag{2.19}$$

where ε_0 is the RMS emittance, defined in Eq. (2.11).

2.2 Transport matrices

The transformation of the beam particles spatial coordinates and divergences between two points z_0 and z_1 along a trajectory can be expressed by the six-dimensional transport matrix *M*:

$$\begin{pmatrix} x \\ x' \\ y \\ y' \\ z \\ \delta p \end{pmatrix}_{z_1} = \begin{bmatrix} M_{1,1} & \cdots & M_{1,6} \\ \vdots & \ddots & \vdots \\ M_{6,1} & \cdots & M_{6,6} \end{bmatrix} \cdot \begin{pmatrix} x \\ x' \\ y \\ y' \\ z \\ \delta p \end{pmatrix}_{z_0}, \tag{2.20}$$

where x, x', y, y' z, δp are the particles spatial coordinates, divergences and longitudinal momentum deviation at the start position z_0 and at the end position z_1. The matrix M is the transport matrix between the start and the end position. Without correlation between the X and the Y transverse planes and absence of correlation between the transverse and the longitudinal motion, the particles spatial coordinates and divergences can be described separately for each transverse plane with a two-dimensional transport matrix *M*:

$$\begin{pmatrix} x \\ x' \end{pmatrix}_{z_1} = \begin{bmatrix} M_{1,1} & M_{1,2} \\ M_{2,1} & M_{2,2} \end{bmatrix} \cdot \begin{pmatrix} x \\ x' \end{pmatrix}_{z_0}. \tag{2.21}$$

In terms of the betatron function, see Eq. (2.9), the transport matrix between the two points will have the following view ([10] p. 170):

$$M = \begin{bmatrix} \sqrt{\frac{\beta_1}{\beta_0}}(cos\Delta\psi + \alpha_0 sin\Delta\psi) & \sqrt{\beta_1\beta_0}sin\Delta\psi \\ \frac{\alpha_0 - \alpha_1}{\sqrt{\beta_1\beta_0}}cos\Delta\psi - \frac{1 + \alpha_1\alpha_0}{\sqrt{\beta_1\beta_0}}sin\Delta\psi & \sqrt{\frac{\beta_0}{\beta_1}}(cos\Delta\psi - \alpha_1 sin\Delta\psi) \end{bmatrix}, \tag{2.22}$$

where α_0, α_1, β_0 and β_1 are the Twiss parameters at the beginning and at the end points, respectively, $\Delta\psi$ is phase advance of the betatron function between start and end points.

2.2.1 Drift space and quadrupole transport matrices

For a drift space, the two-dimensional transport matrix is defined as:

$$M_d = \begin{bmatrix} 1 & l \\ 0 & 1 \end{bmatrix}, \tag{2.23}$$

where l is the drift length.

For an ideal focusing quadrupole magnet (hard-edge model without the fringe fields) the transport matrix has the form [10]:

$$M_{qf} = \begin{bmatrix} cos\,\varphi & \frac{1}{\sqrt{k}} sin\,\varphi \\ -\sqrt{k} sin\,\varphi & cos\,\varphi \end{bmatrix}, \tag{2.24}$$

and for an ideal defocusing quadrupole magnet:

$$M_{qd} = \begin{bmatrix} cosh\,\varphi & \frac{1}{\sqrt{k}} sinh\,\varphi \\ \sqrt{k} sinh\,\varphi & cosh\,\varphi \end{bmatrix}, \tag{2.25}$$

where k is the quadrupole strength $k = eg/p$, e is the particle charge, g is the quadrupole gradient, p is the particle momentum, $\varphi = l_{eff}\sqrt{k}$, where l_{eff} is the effective length of the quadrupole magnet.

2.2.2 Emittance measurements using quadrupole scan

The resulting transport matrix of a quadrupole magnet followed by a drift space will be the result of the product of the drift transport matrix and the quadrupole transport matrix as follows:

$$M = \begin{bmatrix} 1 & l \\ 0 & 1 \end{bmatrix} \begin{bmatrix} cos\,\varphi & \frac{1}{\sqrt{k}} sin\,\varphi \\ -\sqrt{k}\, sin\,\varphi & cos\,\varphi \end{bmatrix}, \tag{2.26}$$

Knowing the particle initial coordinate x_0 and divergence x_0' at the quadrupole entrance, from Eq. (2.26) one can get the particle transverse coordinate x downstream the drift space:

$$x = x_0\left(cos\,\varphi - l\sqrt{k}\, sin\,\varphi\right) + x_0'\left(l\, cos\,\varphi + \frac{1}{\sqrt{k}}\, sin\,\varphi\right). \tag{2.27}$$

In case of $\varphi \ll 1$, known as the thin lens approximation, Eq. (2.27) can be simplified:

$$x = x_0\left(1 - l \cdot l_{eff} \cdot k\right) + x_0'(l\ + l_{eff}), \tag{2.28}$$

and the RMS beam size can be calculated from the following equation:

$$\begin{gathered} \langle x^2 \rangle = \langle {x_0}^2 \rangle \left(1 - l \cdot l_{eff} \cdot k\right)^2 + \\ +2\langle x_0 {x_0}' \rangle \left(1 - l \cdot l_{eff} \cdot k\right)(l\ + l_{eff}) + \langle {x_0}'^2 \rangle (l\ + l_{eff})^2. \end{gathered} \tag{2.29}$$

The right part of Eq. (2.29) is a second order polynomial of *k*. Measuring the transverse beam size $\langle x^2 \rangle$ as a function of the strength of the quadrupole magnet *k* and afterwards fitting the measured data by a second order polynomial, one can find the unknown parameters $\langle {x_0}^2 \rangle$, $\langle {x_0}'^2 \rangle$ and $\langle x_0 {x_0}' \rangle$. In other words, the measured beam size as a function of the strength of the quadrupole magnet is fitted according Eq. (2.29) varying three unknown parameters: $\langle {x_0}^2 \rangle$, $\langle {x_0}'^2 \rangle$ and $\langle x_0 {x_0}' \rangle$. As a result the RMS emittance and Twiss parameters can be calculated according Eq. (2.11) and Fig. 2.1 in section 2.1.2.

2.2.3 Sector magnet transport matrix and momentum measurements

Up to this point it was considered that all particles have the same constant longitudinal momentum. Besides the particle transverse coordinate and divergence, the transport matrix for dipole magnets should include the relative momentum deviation $\delta p = \frac{\Delta p}{p}$ from the design reference particle momentum:

$$\begin{pmatrix} x \\ x' \\ \delta p \end{pmatrix}_{z_1} = \begin{bmatrix} M_{1,1} & M_{1,2} & M_{1,3} \\ M_{2,1} & M_{2,2} & M_{2,3} \\ M_{3,1} & M_{3,2} & M_{3,3} \end{bmatrix} \begin{pmatrix} x \\ x' \\ \delta p \end{pmatrix}_{z_0}. \tag{2.30}$$

In the deflecting plane of a pure sector magnet with bending angle θ, bending radius ρ and constant bending field along the beam trajectory the transport matrix has the following form (see [10] and Appendix 1):

$$M_x = \begin{bmatrix} cos\,\theta & \rho sin\,\theta & \rho(1-cos\theta) \\ -\frac{1}{\rho} sin\,\theta & cos\,\theta & sin\,\theta \\ 0 & 0 & 1 \end{bmatrix}. \tag{2.31}$$

The direction of bending is negative with respect to the x axis. For the opposite direction of bending, coinciding with the x axis, this matrix can be calculated from Eq. (2.31) by changing the sign of θ and ρ:

$$M'_x = \begin{bmatrix} cos\,\theta & \rho sin\,\theta & -\rho(1-cos\theta) \\ -\frac{1}{\rho} sin\,\theta & cos\,\theta & -sin\,\theta \\ 0 & 0 & 1 \end{bmatrix}. \tag{2.32}$$

In the nondeflecting plane, the sector magnet behaves like a drift space with length $l = \rho \cdot \theta$:

$$M_y = \begin{bmatrix} 1 & l & 0 \\ 0 & 1 & 0 \\ 0 & 0 & 1 \end{bmatrix}. \tag{2.33}$$

More complete representations of the sector dipole magnet as a transport matrix can be found in Appendix 1.

In the case of a sector magnet and a drift space with length L downstream the magnet, the resulting transport matrix in the deflecting plane can be calculated as a product of the magnet matrix and the drift matrix:

$$M = \begin{bmatrix} 1 & L & 0 \\ 0 & 1 & 0 \\ 0 & 0 & 1 \end{bmatrix} \begin{bmatrix} cos\,\theta & \rho sin\theta & \rho(1-cos\theta) \\ -\frac{1}{\rho} sin\,\theta & cos\theta & sin\theta \\ 0 & 0 & 1 \end{bmatrix}. \tag{2.34}$$

Knowing the initial particle coordinates x_0, divergences x_0' and relative momentum δp one can calculate the particle transverse coordinates x downstream the dipole and the drift space:

$$x = x_0(cos\theta - \frac{L}{\rho}sin\theta) + x_0'(Lcos\theta + \rho sin\theta) + \delta p \cdot D, \quad (2.35)$$

where

$$D = Lsin\theta + \rho(1 - cos\theta) \quad (2.36)$$

is the dispersion downstream the drift space. Eq. (2.35) shows that a particle transverse coordinate on a screen has a linear dependence on its momentum. This gives the possibility to perform measurements of the beam momentum and momentum distribution by measuring the beam transverse projection on a screen downstream a dipole magnet.

The resolution for such momentum measurements will be limited by the sum of the first two terms on the right side of Eq. (2.35):

$$x_0(cos\theta - \frac{L}{\rho}sin\theta) + x_0'(Lcos\theta + \rho sin\theta). \quad (2.37)$$

Adjusting the beam parameters one can optimize this sum to be as small as possible to improve the momentum resolution.

2.3 Particle acceleration in an RF cavity

The acceleration of ultra-relativistic charged particles in a standing wave accelerating structure can be represented in the following way. The amplitude of the electric field on the axis of the standing wave structure at a specific time t is a function of the longitudinal coordinate along the structure and this field oscillates in time according to the harmonic law:

$$E_z(z,t) = E_0(z) \cdot sin(\omega t + \varphi), \quad (2.38)$$

where $E_z(z,t)$ is the longitudinal electric field on the axis of the structure, $E_0(z)$ is the electric field amplitude as a function of the longitudinal coordinate, $\omega = 2\pi f$, where f is the RF frequency, t is the time and φ is the initial RF phase of the structure when a particle enters it. Here it is assumed that the structure consists of several identical cells, so $E_0(z)$ is a periodic function. Therefore, to have the most efficient acceleration, the time of flight of the particle through one cell should be equal to the half period of the RF. The total acceleration of the whole structure can be calculated by multiplying the acceleration of one cell by the total number of cells.

The momentum of a particle passing one cell of an accelerating structure is:

$$p_z = p_0 + \int_0^T eE_0(z) \cdot sin(\omega t + \varphi) dt \tag{2.39}$$

where p_z is the momentum of the particle downstream the structure, p_0 is the momentum of the particle upstream the structure, e is the electrical charge of the particle and T is the time of flight of the particle through the cell. Solving for the sine function and taking into account that $z = ct$ for ultra-relativistic particles the momentum is:

$$\begin{aligned} p_z = p_0 + e \cdot cos(\varphi) \int_0^T E_0(ct) \cdot sin(\omega t) dt + \\ + e \cdot sin(\varphi) \int_0^T E_0(ct) \cdot cos(\omega t) dt \end{aligned} \tag{2.40}$$

The second integral in Eq. (2.40) will be zero since it integrates an odd function in a half period (around *T*/2). Here it is assumed that $E(z)$ is an even function around the cell center. As a result the particles momentum gain after the whole accelerating structure is:

$$p_z = p_0 + V \cdot cos(\varphi), \tag{2.41}$$

where $V = Ne \int_0^T E(ct) \cdot sin(\omega t) dt$ is the maximum momentum gain by a particle passing through the accelerating structure and N is the number of the structure cells. The dependence of the particle momentum gain as a function of the phase of the structure in Eq. (2.41) will be the same for traveling wave structures, since in this case the charged particles are always moving synchronously with the RF wave.

Fig. 2.2 shows a model of the acceleration of a bunch of charged particles by an RF cavity. The resulting momentum of a particle coming to the cavity at phase φ is:

$$p_z = p_0 + V \cdot cos(\varphi - \varphi_0). \tag{2.42}$$

Here φ_0 is the phase for which a single particle, entering the cavity at this phase, will obtain the highest possible momentum gain (for the whole bunch such phase is also called Maximum Mean Momentum Gain (MMMG) phase). In Fig. 2.2 the RF phase of the electric field in the cavity is increasing from left to right. The head of the bunch is coming first to the cavity meaning that it comes in the earlier phase than the tail. In other words, the bunch head in this figure is on the left side and the tail is on the right side.

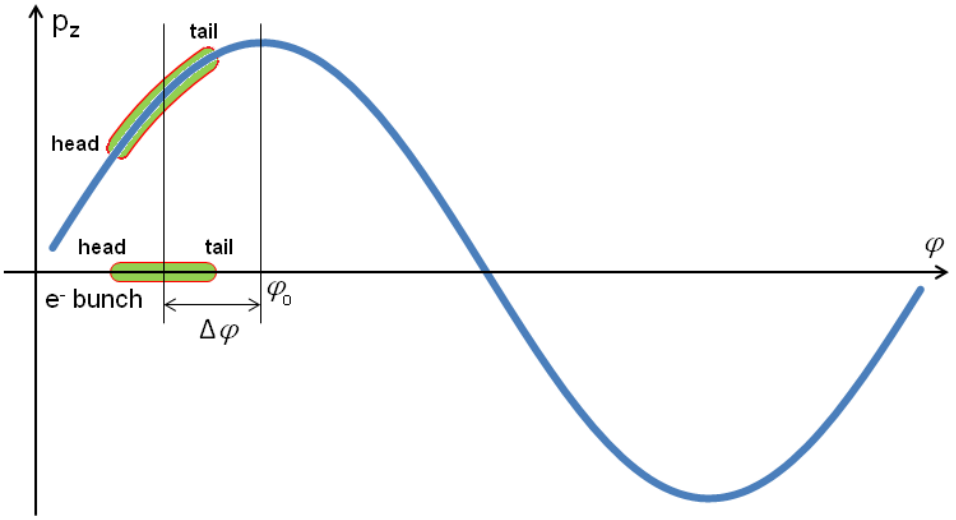

Fig. 2.2: Model of the acceleration of a bunch of charged particles by an RF cavity. The particle momentum gain is shown with the blue curve as a function of the RF phase at which the particles enter the cavity.

As a result, if the whole bunch is coming to the cavity earlier than the phase φ_0 with a phase difference of $\Delta\varphi$, the tail of the bunch will get higher acceleration than the head. As a result the whole bunch will obtain a momentum chirp – particles in the bunch will have a correlation between their longitudinal momenta and longitudinal position within the bunch. The time momentum chirp k of the bunch can be estimated as a first order derivative of Eq. (2.42) with an inversed sign:

$$k = -\frac{dp_z}{dt} = V\omega \cdot sin(\Delta\varphi), \tag{2.43}$$

where V is the maximum momentum gain induced by the accelerating cavity, $\omega = 2\pi f$ and f is the operating RF frequency of the accelerating cavity, $\Delta\varphi$ is the phase at which the bunch enters the cavity relative to the phase φ_0. For the case shown in Fig. 2.2 the momentum chirp k which the bunch gains from the accelerating structure is negative since $\Delta\varphi$ is negative.

Chapter 3

The Photo Injector Test facility at DESY, Zeuthen site

One of the key parameters for the injector part of accelerator based light sources is the electron bunch normalized transverse emittance. For example, for the successful operation of the European X-ray Free Electron Laser (XFEL) the transverse slice emittance should not exceed 1.4 mm mrad for 1 nC bunch charge at the undulator entrance [11]. To demonstrate that the electron source could fulfill such a requirement the Photo Injector Test facility at DESY, Zeuthen site (PITZ), was built [4]. PITZ aims to develop and characterize the electron source for Free electron LASer in Hamburg (FLASH) and the European XFEL in Hamburg.

The current schematic layout of the PITZ beamline is shown in Fig. 3.1. The main components of the PITZ setup are a photocathode laser system, an RF photo-electron gun, an accelerating structure, a Cut Disk Structure (CDS) – also called booster cavity, three dipole spectrometers – one in the low energy section downstream the gun (Low Energy Dispersive Arm – LEDA), a second one in the high energy section downstream the accelerating structure (the first High Energy Dispersive Arm – HEDA1) and a third one at the end of the PITZ beamline (the second High Energy Dispersive Arm – HEDA2), three Emittance Measurement Stations (EMSYs), a Transverse Deflecting Structure (TDS) and a Phase Space Tomography module (PST).

The working principle of the PITZ setup is shortly described in the following. The laser beam of the photocathode laser system is imaged on the cathode surface and causes photoemission. The emitted electrons are accelerated in the RF fields of the gun cavity creating an electron bunch with the energy at the level of about 6.5 MeV. The resulted beam momentum can be measured with the LEDA dipole located downstream. The CDS booster further accelerates the electron bunch up to an energy of 26 MeV, which can be measured with the HEDA1 and HEDA2 dipoles.

Several diagnostic components between the gun and the booster are used: two Faraday Cups (FCs) and one Integrating Current Transformer (ICT) for bunch charge measurements and a few screen stations for transverse beam position and beam size measurements.

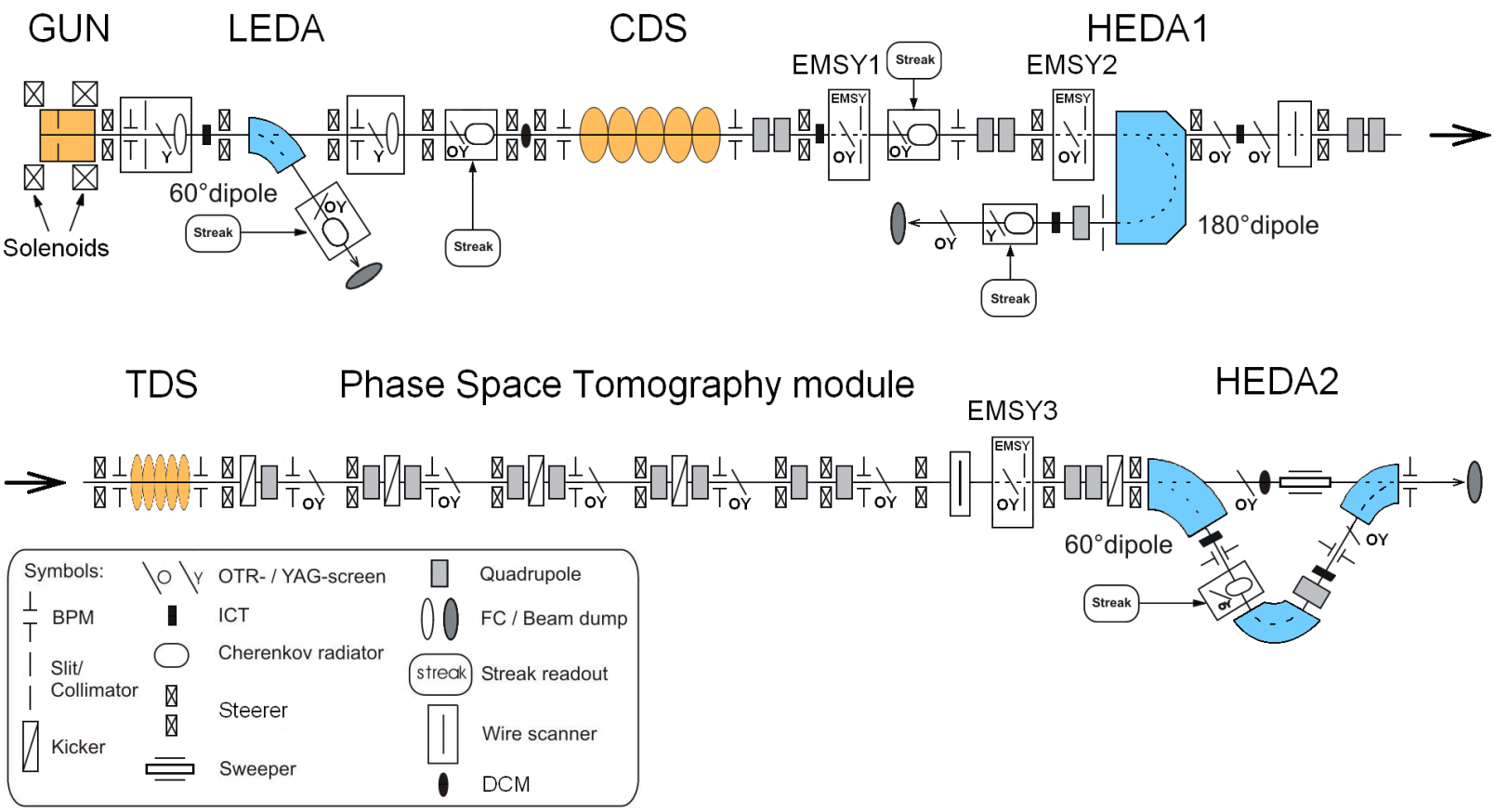

Fig. 3.1: PITZ beamline schematic layout. The beam propagates from left to right.

Downstream the booster cavity the beamline consists of different types of diagnostic devices for detailed electron bunch characterization. There are several ICTs for bunch charge measurements. Three dedicated screen stations can be used for beam position and beam size measurements as well as for transverse emittance measurements utilizing the slit scan technique [6]. A tomography module located further downstream the booster is also used for measurements of the transverse phase space and can simultaneously restore the horizontal and vertical transverse planes in contrast to the slit scan technique, see [12] and [13] for details.

The newly installed TDS cavity gives the possibility for time resolved, longitudinal bunch profile and transverse slice emittance measurements. The first screen in the dispersive section HEDA2, together with the TDS cavity, can be used for longitudinal phase-space measurements. The achievable time resolution for the longitudinal phase-space measurements is expected to be better than 0.3 ps. The momentum resolution can be estimated as 10 keV/c for such measurements, see Chapter 4.

In the following sections the PITZ beamline components related to the thesis topic will be described in more detail.

3.1 Photocathode laser system

The laser system at PITZ serves as a source of the specially shaped photon pulses used to generate the electron pulses from the photocathode. The PITZ laser system was designed and built by the Max Born Institute (MBI), Berlin [14]. The system consists of a Yb:YAG oscillator, a longitudinal pulse shaper, amplifier stages and conversion crystals. This system can produce up to 800 ultraviolet laser pulses within a pulse train with 1 μs pulse separation and with a train repetition rate of 10 Hz. The temporal distribution of the laser pulses can be adjusted with a pulse shaper from typically 2 ps FWHM Gaussian profile to a flat-top profile with a duration of about 21 ps FWHM and 2 ps rise and fall times [15]. The transverse size of the laser spot at the cathode can be controlled with a Beam Shaping Aperture (BSA) in the range from about 50 μm up to a couple of millimeters. The pulse energy of the beam can be varied from 0 up to about 1.0 μJ per pulse at the cathode.

The Yb:YAG oscillator produces laser pulses with a wavelength of 1030 nm. Then the pulse shaper is installed to allow manipulation of the laser pulse temporal profile. Further, the laser pulse energy is amplified and infrared laser pulses are converted to ultraviolet in two steps with the frequency doubling crystals: at the first crystal to 515 nm and then at the second one from 515 nm to the 257.5 nm. The output laser wavelength is in the range of high spectral sensitivity for the Cs_2Te photocathodes and the resulting quantum efficiency for this wavelength and this type of photocathode can be around 10% [16].

The transverse laser profile can be measured at the position of the virtual cathode located at the same distance from the BSA and had the same imaging of

the laser beam as the real photocathode. The temporal laser profile can be measured using the Optical Sampling System (OSS) with temporal resolution of about 1 ps [17].

3.2 RF gun

The normal conducting 1.3 GHz L-band 1.6-cell copper gun cavity with a Cs_2Te photocathode accelerates electron bunches up to 6.5 MeV energies, Fig. 3.2. The cavity is surrounded by two solenoids: the main solenoid to focus the beam and counteract its expansion due to space charge forces and the bucking solenoid to compensate the longitudinal magnetic field from the main solenoid on the cathode surface in order to minimize the residual angular momentum of the emitted electrons.

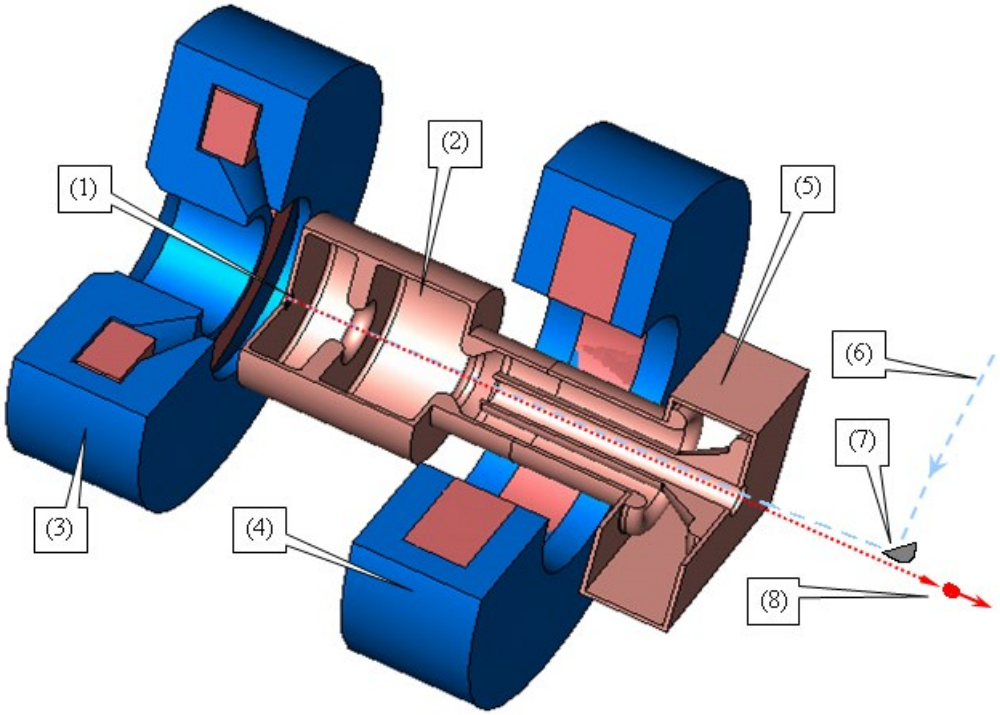

Fig. 3.2: PITZ RF gun, 3D model. (1) is the Cs_2Te photocathode, (2) is the 1.6-cell L-band (1.3 GHz) standing wave copper RF gun cavity, (3) and (4) are the bucking and the main solenoids correspondingly, (5) is the coaxial RF coupler, (6) shows the trajectory of the UV laser beam, (7) is the in vacuum mirror, (8) depict the electron bunch trajectory.

As it can be seen in Fig. 3.2, the laser beam (6) is reflected by a vacuum mirror (7) and thus impinges the photocathode (1) close to normal incidence. As a result of

the photoemission process electrons grouped in an electron bunch are created. This bunch is accelerated inside the cavity (2) with RF fields feed through the coaxial coupler (5). Afterwards the bunch is focused by the main solenoid (4) and propagates along the PITZ beamline (8). The Bucking solenoid (3) compensates the longitudinal magnetic field from the main solenoid (4) on the cathode surface (1).

The gun is fed by a 10 MW klystron and can be operated with up to 700 μs RF pulse duration, 7 MW peak RF power (corresponds to about 60 MV/m on-axis peak electric field on the cathode surface) and 10 Hz repetition rate.

3.3 CDS Booster

For further acceleration of the electron bunch coming from the gun a CDS booster is used. The CDS booster was designed by the Institute for Nuclear Research (INR, Troitsk, Russia) and built by DESY (Hamburg, Germany). This 1.3 GHz L-band standing wave 14-cells copper structure was designed for RF pulses with duration up to 900 μs, 8 MW RF peak power, 10 Hz repetition rate and with a maximum accelerating gradient of 14 MV/m [18]. It results in a bunch energy gain of 20 MeV and a final bunch energy of about 26 MeV.

A 3D model of the PITZ CDS booster cavity is presented in Fig. 3.3.

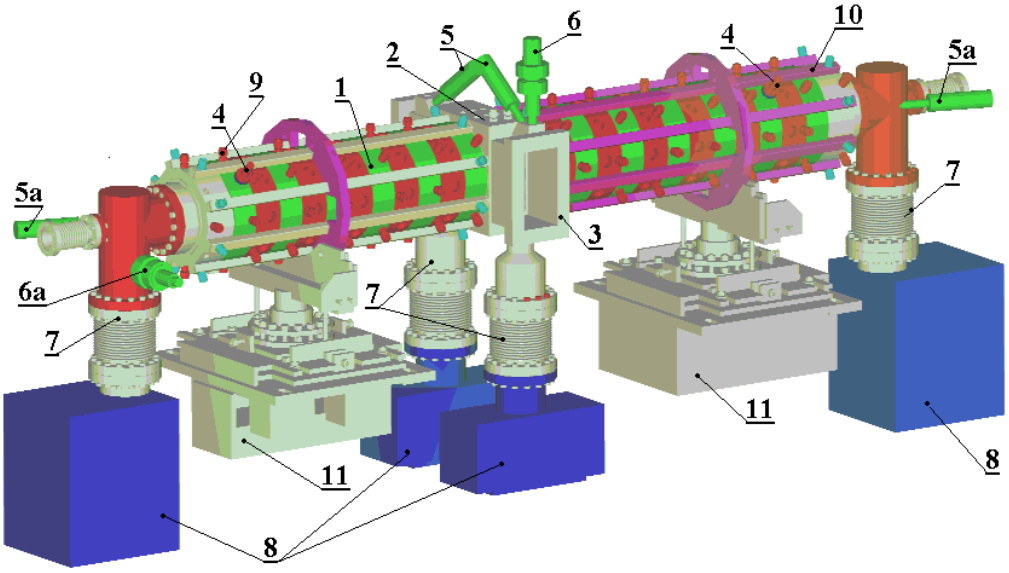

Fig. 3.3: 3D model of the CDS booster [19]. 1 regular cells, 2 RF coupler cell, 3 RF input flanges, 4 RF probes, 5 photo multiplier detectors, 5a spare photo multipliers, 6 vacuum gauge, 6a spare vacuum gauge, 7 pumping tubes with bellows, 8 ion pumps, 9 inner cooling circuit outlets, 10 outer cooling circuit, 11 support and alignment system. The beam propagates from right to left.

3.4 Screen stations

A number of screen stations can be used for measurements of the transverse beam distribution and transverse position of the beam along the PITZ beamline. The screen stations are equipped with one or both types of the following screens: Yttrium Aluminum Garnet powder coated (YAG) screens or/and Optical Transition Radiation (OTR) screens [20]. The YAG screens have a high sensitivity and therefore are suitable for low intensity beam observations in the low energy section as well as in the high energy section. For the high intensity beams YAG screens saturate and cannot be used. The OTR screens have a relatively small sensitivity for low energy, low intensity electrons and therefore are used in the high energy section of the PITZ beamline for measurements and observations of high intensity long bunch trains with high energy and high total average current.

The two screen orientations used at PITZ are 45° and 90° with respect to the direction of the beam propagation as shown in Fig. 3.4. For the 90° orientation a mirror on a silicon substrate behind the screen is used to reflect the light emitted from the screen to a CCD camera. The optical readout system for each screen includes at least the following components: the screen, the mirror, the lens and the CCD camera.

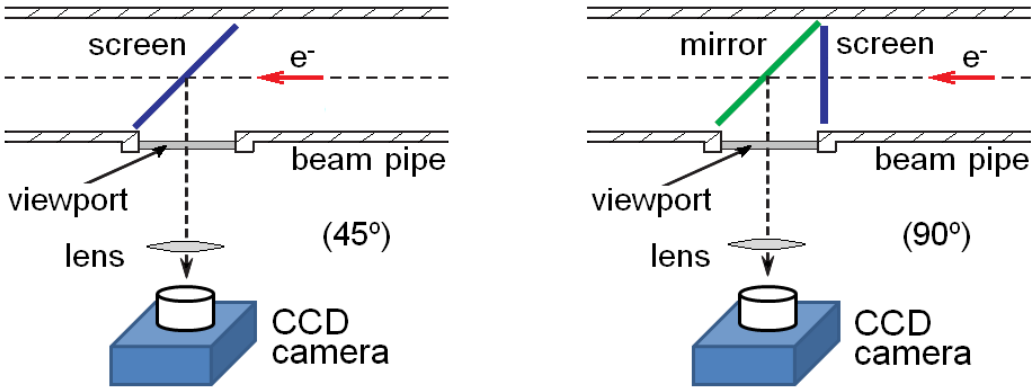

Fig. 3.4: Two types of screen orientation used in the PITZ beamline: 45°, left image, and 90°, right image [20]. The beam propagates from right to left.

For the YAG screens both types of orientation are used in the PITZ beamline. For OTR screens mainly the 45° orientation is used, since the maximum light intensity is radiated at the 45° angle.

The spatial resolution for the transverse beam size measurements will be limited by the alignment of the optical readout system, by the lens imperfections and by the size of the pixel of the CCD camera. The resolution limit from the alignment can be roughly estimated as 50 µm. The corresponding scaling

parameters for the screens in the PITZ beamline related to the thesis are shown in Table 3.1. Usually one of the two lenses for each screen can be used: the first, to see the whole screen, and the second, to have a zoomed image of the area of interest.

Table 3.1: Scaling parameters of the screens.

Screen station	Screen orientation	Focal length of lens, [mm]	Scale, [μm/pix]	Comment
Disp2.Scr1	45º	50	115	HEDA1 observation screen
		120	35	
Disp3.Scr1	90º	80	63	HEDA2 observation screen
		200	19	
High1.Scr5	90º	100	74	HEDA1 reference screen
		160	39	
		250	13	
PST.Scr1	90º	140	75	Screen for TDS measurements
		200	46	

For example, for the HEDA1 observation screen Disp2.Scr1 for the lens 50, the scale is 115 μm/pix. One pixel of the CCD camera for such scale will correspond at this screen to a relative momentum spread of 115 μm/0.6 m = $2 \cdot 10^{-4}$, what is about 4 keV/c for 22 MeV/c beam (0.6 m is the dispersion at the screen position, see section 3.5). This parameter will limited the momentum distribution measurements as one cannot measure the size less than one pixel. Moreover, one can expect here an additional error from the optics alignment of about 1.8 keV/c (= 22 MeV/c * 50 μm/0.6 m). The same calculations for the HEDA2 observation screen and the lens 80 give about 1.5 keV/c for one pixel, and an additional error from the optics alignment of about 1.2 keV/c.

For transverse projected emittance measurements using the slit scan technique [6] three dedicated Emittance Measurement SYstems (EMSYs) are used at PITZ located at different position along the beamline (see Fig. 3.1). Each EMSY has two actuators, a vertical and a horizontal one, with four defined positions: two slit masks with 10 and 50 μm slit opening (both slits are 1 mm thick), YAG screen or OTR screen (for the second actuator) and initial empty position. The actuators have to be inserted separately to the beam path to take a beam image from the screen or to cut a small part of the beam (beamlet) by a slit mask. The image of the beamlet is observed at another screen station downstream of EMSY. Combining together all the beamlets for different positions of the EMSY slit the transverse phase space can be reconstructed and the transverse emittance can be calculated [21].

3.5 The first High Energy Dispersive Arm

The first High Energy Dispersive Arm (HEDA1) is located about 8 m downstream the electron gun, see Fig. 3.1, and is used for measurements of the beam momentum distribution with a mean momentum up to 40 MeV/c [22]. It consists of a 180° vertical dipole magnet Disp2.D1, a moveable slit mask and a quadrupole magnet Disp2.Q1, used for slice emittance measurements [23], two screen stations Disp2.Scr1 and Disp2.Scr2 and a beam dump, Fig. 3.5.

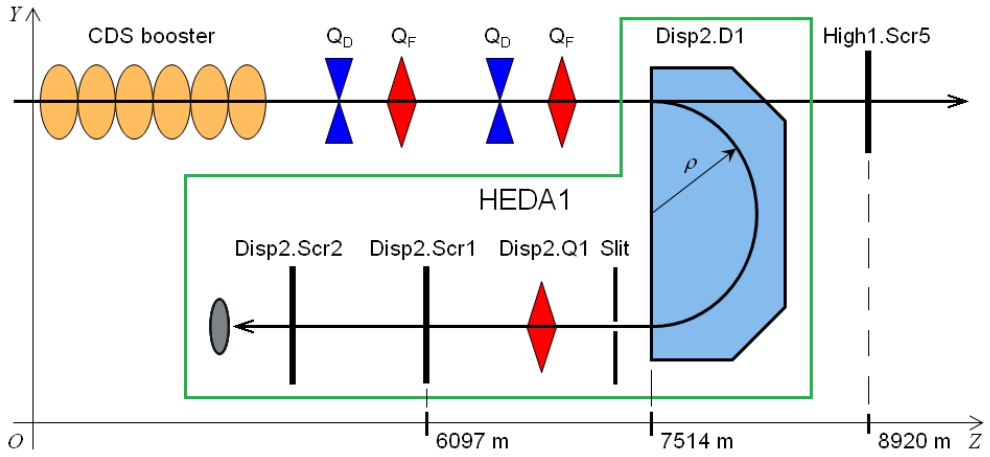

Fig. 3.5: HEDA1 momentum measurement setup. The beam propagates from left to right.

The momentum distribution is measured as a vertical profile of the beam on the observation screen Disp2.Scr1. A reference screen – High1.Scr5 and four quadrupole magnets upstream the dipole can be used to optimize the setup for the best momentum resolution [7].

The momentum p_0 of a reference particle, traveling on a design trajectory and impinging on the vertical center of the observation screen Disp2.Scr1 after the dipole can be calculated as:

$$p_0 = eB\rho, \tag{3.1}$$

where e is the electron charge, B is the magnetic field inside the dipole and ρ is the bending radius of the dipole. The vertical coordinates of the other particles in the bunch on the observation screen can be calculated using the following equation (see Eq. (2.35) for the dipole bending angle $\theta = 180°$):

$$y = y_0 + y_0'L - \delta p \cdot D, \tag{3.2}$$

where y is the particle vertical coordinate on the observation screen, y_0 and y_0' are the particle vertical coordinate and the particle vertical divergence at the dipole entrance, L is the drift length between the dipole exit and the observation

screen, δp is the particle relative momentum with respect to the ideal reference particle $\delta p = (p - p_0)/p_0$ and $D = 2\rho$ is the dispersion for the 180° dipole magnet, where $\rho = 0.3$ m is the bending radius of this dipole at PITZ. The sign was flipped compared to Eq. (2.35) to keep the same direction of the y axis. The horizontal coordinates of the particles on the observation screen can be calculated from the beam transport through a drift space with length equal to $\pi\rho + L$, see Eq. (2.23).

The first two terms in the right part of equation (3.2) describe the transformation of particle's coordinate after the drift space with length L and define the beam size there. The last term shows a linear dependence of the particles vertical coordinate on the observation screen Disp2.Scr1 on its momentum. The best momentum resolution is achieved if the sum of two first terms is the smallest for all particles, or, in other words, the vertical beam size after a drift with a length L is the smallest. To adjust the momentum resolution the reference screen High1.Scr5 is installed in the straight section at the same distance L downstream the dipole entrance as the screen Disp2.Scr1 is downstream the dipole exit [7]. The vertical beam size σ_y can be measured there and adjusted by tuning the quadrupole magnets upstream the dipole magnet to have the vertical beam size as small as possible. As a result, the relative resolution of the momentum measurements can be estimated as:

$$\delta p = \frac{\Delta p}{p} = \frac{\sigma_y}{D}. \tag{3.3}$$

Longitudinal phase space measurements can be performed in this section as well using the streak camera readout at the observation screen Disp2.Scr1 [7], [8].

3.6 The second High Energy Dispersive Arm

The second High Energy Dispersive Arm (HEDA2) at PITZ was designed and manufactured in a collaboration between Laboratoire de l'Accélérateur Linéaire (LAL, Orsay, France) and DESY. This dispersive section is located about 17 m downstream the electron gun. HEDA2 is designed for high resolution momentum distribution measurements of the electron beam with beam mean momentum up to 40 MeV/c, longitudinal phase-space measurements with slice momentum spread resolution down to 1 keV/c and for transverse slice emittance measurements [24].

The HEDA2 setup is shown in Fig. 3.6 and consists of three dipole magnets D1, D2 and D3, a quadrupole magnet Disp3.Q1, used for slice emittance measurements, three beam position monitors (BPMs), two ICTs and two screen stations Disp3.Scr1 and Disp3.Scr2. Each screen station has two screens - YAG and OTR, which can be used for the electron beam observations and measurements. The third dipole D3 is used to bend the electron beam trajectory back to the straight section and send the beam to the beam dump at the end of the PITZ beamline.

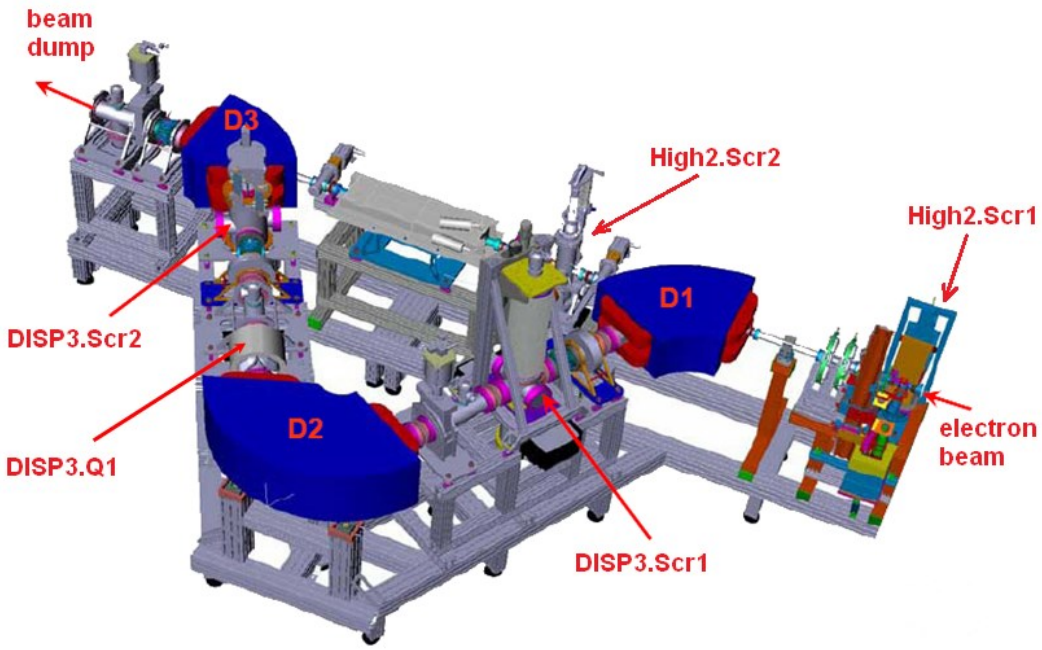

Fig. 3.6: 3D model of HEDA2. The section consists of: three dipole magnets D1, D2 and D3, two screen station Disp3.Scr1 and Disp3.Scr2, a quadrupole magnet Disp3.Q1, three BPMs and two ICTs. The beam propagates from right to left.

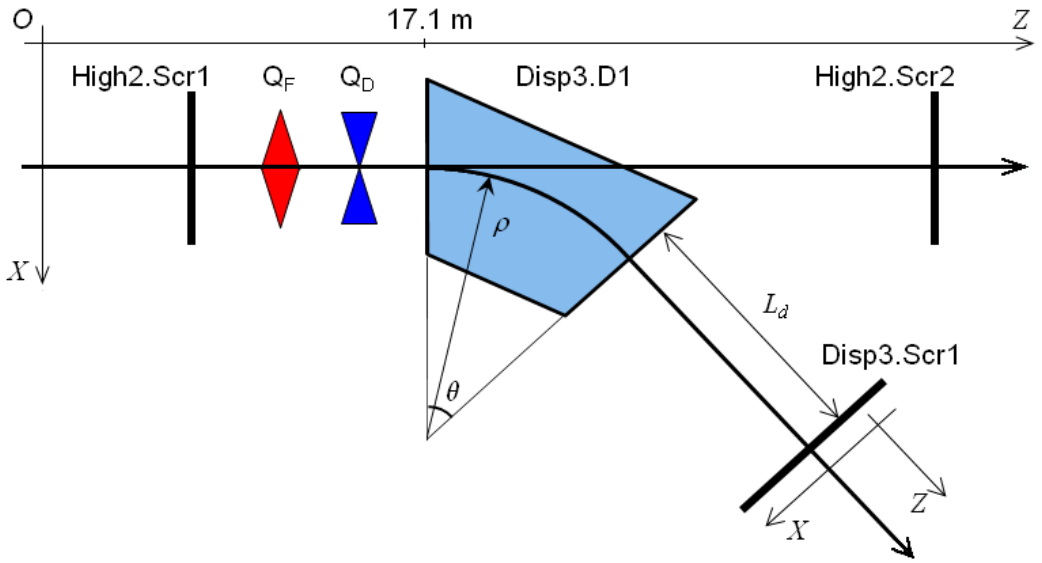

Fig. 3.7: Layout of the HEDA2 section part related to the beam momentum measurements. The beam propagates from left to right. The vertical axis *Y* points out from the drawing plane.

The momentum distribution is measured as a horizontal profile of the beam image at the observation screen Disp3.Scr1, see schematic layout in Fig. 3.7. The two quadrupole magnets upstream the dipole and the screens High2.Scr1 upstream and High2.Scr2 downstream the dipole can be used to optimize the setup for the best momentum resolution.

The beam position on the observation screen Disp3.Scr1 downstream the dipole magnet depends on the beam momentum, the magnetic field and the length of the particle path inside the dipole. The momentum p_0 of the reference particles which are on the design trajectory and hit the screen center with zero horizontal coordinate can be calculated from Eq. (3.1). For the other particles, having momentum p, the horizontal coordinate on the observation screen Disp3.Scr1 can be calculated from the equation:

$$x = x_0 R_{1,1} + x_0' R_{1,2} + \delta p \cdot D, \tag{3.4}$$

where $R_{1,1} = -0.510$, $R_{1,2} = 0.870$ m and $D = -0.906$ m (see Eq. (2.35) for the dipole bending angle $\theta = 60°$, bending radius $\rho = 0.6$ m and $L_d = 0.7$ m). x is the particle horizontal spatial coordinate on the observation screen, x_0 is the horizontal spatial coordinate at the dipole entrance and x_0' is the particle horizontal divergence at the dipole entrance. The last term in the right part of Eq. (3.4) shows a linear dependence of the particles horizontal coordinate on the screen as a function of the particle momentum – particles with higher momentum will be deflected towards the negative *X* coordinate. The dispersion is negative while the bending direction coincides with the direction of the x axis, Fig. 3.7 and Eq. (2.31) and Eq. (2.32).

The best momentum resolution will be achieved if the sum of two first terms in the equation will be the smallest for all the particles in the beam. This condition can be written in the following inequality:

$$\left| x_0 R_{1,1} + x_0' R_{1,2} \right| < |\delta p_0 \cdot D|, \tag{3.5}$$

where δp_0 will be the relative momentum resolution. The solution of this inequality for the defined δp_0 can be represented as an area in the transverse phase space for some given range of the horizontal coordinate x which, for example, corresponds to the diameter of the beam pipe of the accelerator beamline, Fig. 3.8. The red line represents the zero sum of the left part of inequality (3.5) and the light blue parallelogram represents the area which inner points satisfy the condition of the inequality for some given range of the horizontal coordinate x. From the other side, if the area, occupied by the particles, is known (the transverse phase space of the bunch) the relative momentum resolution δp_0 can be estimated as the width of the area around the red line multiplied by $R_{1,2}$ and divided by D:

$$\delta p_0 = \frac{\sigma_{x_0'} R_{1,2}}{D}, \tag{3.6}$$

where $\sigma_{x_0'}$ is the vertical RMS width of the phase space around the red line, which is the non-correlated RMS divergence.

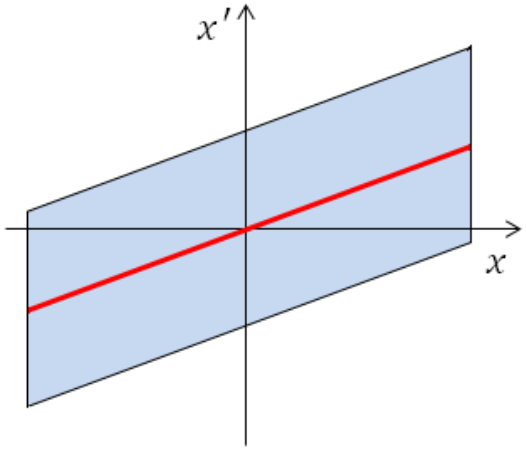

Fig. 3.8: Solution of inequality (3.5) represented as a blue area in the transverse phase space and the red line shows the zero sum of the left part of this inequality.

For example, if one takes the beam with 1 mm mrad normalized transverse RMS emittance and stretches it along the red line up to the full range in the x axis – 30 mm wide, Fig. 3.8. Assuming the uniform particle distribution in the transverse phase space, the non-correlated RMS divergence $\sigma_{x_0'}$ of this beam can be estimated as $3 \cdot 10^{-6}$ for 22 MeV/c beam momentum. As a result the relative momentum resolution δp_0 will be about $3 \cdot 10^{-6}$, and in absolute values it is 60 eV/c. For the similar beam parameters the numerical simulations gives worse momentum resolution of about 0.2 keV/c. Such big difference relative to the rough estimation comes from the fact that the dipole is not linear element for such a wide beam and in result the particles motion cannot be fully described by the matrix formalism.

In an experiment the best momentum resolution in the HEDA2 section can be achieved adjusting the quadrupole magnet upstream the dipole magnet in such a way that the smallest electron bunch horizontal size at the observation screen Disp3.Scr1 is achieved.

Additionally to the beam momentum measurements the electron bunch longitudinal phase space can be measured at the first screen Disp3.Scr1 after the Disp3.D1 dipole using the TDS cavity, Fig. 5.13. The electron bunch image on the screen will show the bunch longitudinal phase space, where the image's horizontal axis corresponds to the momentum and the vertical axis corresponds to

the longitudinal coordinate within the electron bunch (see more details in Chapter 5).

The vertical slice emittance measurements can be done with a quadrupole scan technique using the quadrupole magnet Disp3.Q1 and the second observation screen Disp3.Scr2 of HEDA2. To select a longitudinal slice of the bunch the horizontal slit at the Disp3.Scr1 station will be used when a linear correlation between the beam particles momenta and longitudinal coordinates will be realized with booster off-crest operation [23].

Chapter 4

The Transverse Deflecting Structure

RF deflecting structures are widely used for the characterization of electron bunch longitudinal properties such as bunch longitudinal profile or even bunch longitudinal phase space [25], [26], [27]. Also, the bunch transverse slice emittance can be measured [28]. Such RF structures are also known as transverse deflecting structures (TDS) because they deflect particles of the beam transversely with respect to their design trajectories.

The first iris-loaded RF deflecting structure was built at SLAC in the 1960's for particle separation and called LOLA for the first letters in the names of its inventors [29]. In 2003 this structure was installed at the FLASH linac (DESY, Hamburg) [26]. Later it was decided to use a similar type of RF deflector for the European X-ray Free Electron Laser: one downstream the gun and two downstream of each of the two bunch compressors [30]. A prototype of the structure for the XFEL was designed and manufactured by the Institute for Nuclear Research (INR, Troitsk, Russia) in 2012 and is currently installed at the PITZ facility [31], [32]. This PITZ TDS has the aim to prove the required performance for all TDS subsystems as well as serve as a diagnostics tool for PITZ.

The Transverse Deflecting Structure (TDS) for PITZ was designed and manufactured by the Institute for Nuclear Research (INR, Troitsk, Russia) as a prototype of the TDS cavity for the European XFEL injector [31]. The structure deflects the electrons vertically in linear dependence on the longitudinal coordinate of the particles inside the bunch, what in result allows measurements of the longitudinal bunch properties (see more details in Chapter 5). A 3D model of the TDS cavity installed at PITZ is shown in Fig. 4.1. A 3D model of a regular TDS cell is shown in Fig. 4.2; the direction of the beam deflection is vertical. The corresponding sizes are shown in Table 4.1, where Rh is the stabilization holes radius, Rc is the cell inner radius, Ra is the aperture radius, L is the distance between stabilization hole and the cavity center and d is the cell length equal to one third of the RF wavelength.

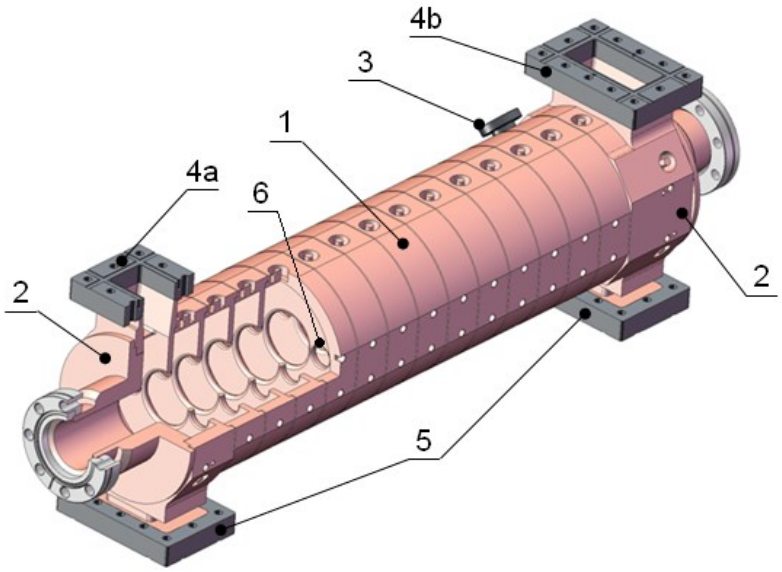

Fig. 4.1: 3D model of the transverse deflecting structure installed in the PITZ beamline [31]. 1 is the regular cells, 2 are the RF input and output coupler cells, 3 is the RF probe, 4a and 4b are RF input and RF output flanges, respectively, 5 are RF flanges for pumping. The beam propagates from right to left.

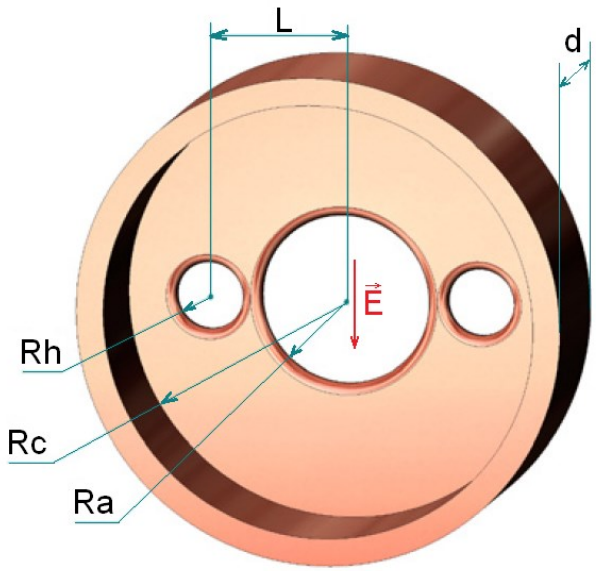

Fig. 4.2: A 3D model of the TDS regular cell. The direction of the electric field E in the cell center is vertical. Rh is the stabilization holes radius, Rc is the inner radius of the cell, Ra is the aperture radius, L is the distance between stabilization hole and the cavity center and d is the cell length.

Table 4.1: TDS cell parameters.

Rh	Rc	Ra	L	d
9.0 mm	55.27 mm	21.55 mm	34.65 mm	33.31 mm

The PITZ TDS, Fig. 4.1, is a traveling wave 3 GHz RF copper structure with two stabilizing holes to have an RF field mode with vertical deflecting electric field (LOLA type structure [29]). It operates in $2\pi/3$ mode, i.e. the length of three cells (three times d in Table 4.1) corresponds to one period of the RF wave. The coupling between cells is made such that the RF phase velocity of the structure is the speed of light in the vacuum.

The structure consists of 14 regular cells, Fig. 4.2, including RF input and output coupler cells, 2 in Fig. 4.1. The total length of the structure including the vacuum flanges is 0.7 m. The main design parameters of the TDS cavity are summarized in Table 4.2 and the calculated RF parameters of the TDS cavity are shown in Table 4.3 [31], [33].

Table 4.2: TDS main parameters.

RF frequency	2997 MHz
Number of cells	16
Deflecting Voltage	0.2 – 1.7 MV (2.5 MW)
Pulse duration	0.7 – 3.1 μs
Filling time	< 120 ns
Filling + decay time	< 200 ns

Table 4.3: Calculated RF parameters for the TDS.

RF frequency, $\boldsymbol{f}$	2997.2 MHz
Group velocity, $\boldsymbol{\beta_{gr}}$	-0.01587
Shunt impedance, $\boldsymbol{r_{sh}}$	16.85 MOhm/m
Quality factor, $\boldsymbol{Q}$	11780
Attenuation, $\boldsymbol{\alpha}$	0.168 m^{-1}

The total deflecting voltage of the cavity is adjustable in the range from 0.2 MV to 1.7 MV (corresponding to about 2.5 MW RF peak power in the cavity), depending on the type of measurement and the required time resolution (see

Chapter 5). The duration of the flat part of the RF pulse in the cavity is adjustable in the range from 0.7 μs up to 3.1 μs. The short filling and decay time of the TDS RF pulse and the adjustable duration aim to select from one up to three (in case of a time delay between the bunches of 1 μs) electron bunches from a long bunch train for further analysis and not to disturb any other bunches in the train.

4.1 TDS basic operation principle

When passing the PITZ TDS cavity with RF fields switched on a particle on the axis of the structure is under the action from both the transverse electric and magnetic fields orthogonal to each other. The total transverse deflecting force amplitude Amp_F can be calculated from the Lorenz force law, Eq. (2.1):

$$Amp_F = e\left|\vec{E}_{Re} + i\vec{E}_{Im} + \left[\vec{v} \times (\vec{B}_{Re} + i\vec{B}_{Im})\right]\right|, \tag{4.1}$$

and transverse deflecting force phase $Phase_F$:

$$tan(Phase_F) = \frac{\vec{E}_{Im} + \left[\vec{v} \times i\vec{B}_{Im}\right]}{\vec{E}_{Re} + \left[\vec{v} \times i\vec{B}_{Re}\right]}, \tag{4.2}$$

where $\vec{E}_{Re}$, $\vec{E}_{Im}$, $\vec{B}_{Re}$ and $\vec{B}_{Im}$ are the real and imaginary parts of the numerically calculated electric and magnetic fields, respectively [31]. The calculated transverse (vertical) deflecting force amplitude along the deflector axis z (a) and deflecting force phase (b) are shown in Fig. 4.3. The resulted force which particle see during traveling through the cavity is:

$$F = Amp_F \cdot cos(Phase_F + \omega t), \tag{4.3}$$

When an electron bunch propagates through the traveling wave structure, the electrons always see a constant phase of the deflecting force: $Phase_F + \omega t = Const$, Fig. 4.3 (b). In other words, the bunch is propagating through the structure together with the RF field. As a result, if one part of the bunch starts to propagate through the structure at some RF phase, when all RF fields are zero, this part will go through the whole structure and will not see any deflecting force on its way. But if one part of a bunch comes to the structure at some other RF phase, this part will always see the RF field at this phase and therefore see a nearly constant deflecting force along the structure.

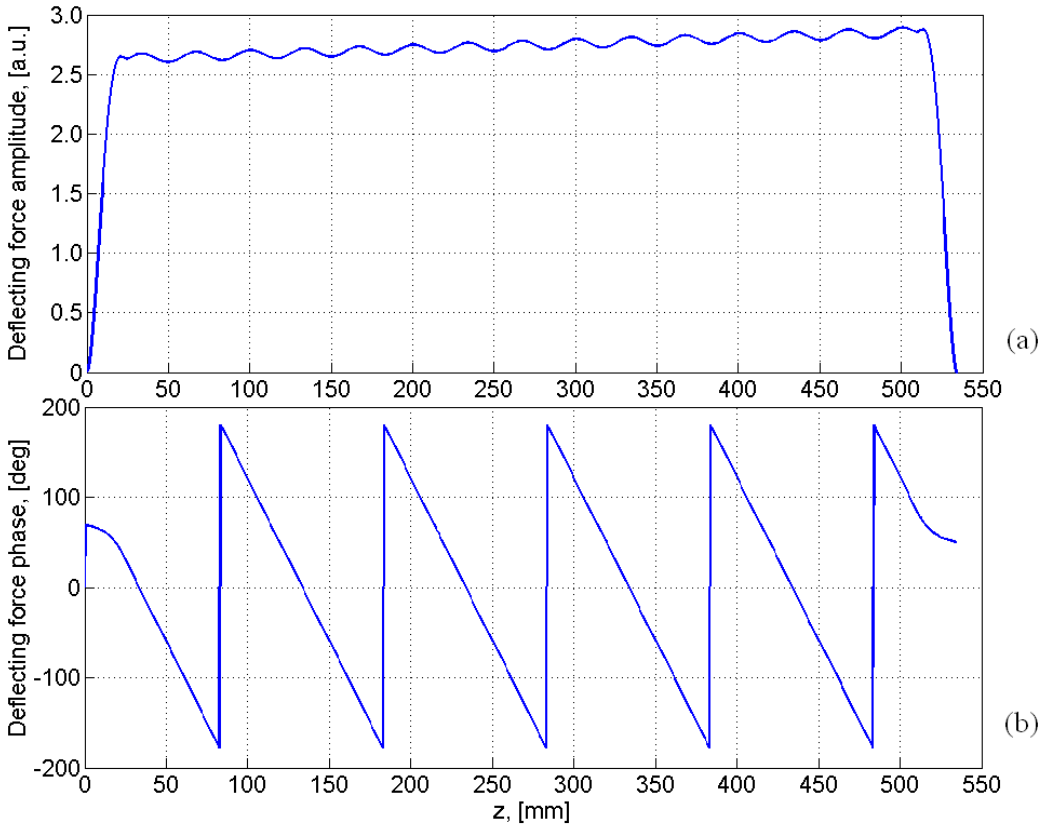

Fig. 4.3: Calculated transverse deflecting force amplitude of the TDS cavity as a function of the longitudinal coordinate within the structure (a) and the deflecting force phase along the z axis (b) at the current moment $t = 0$ [31]. The beam propagates from left to right. RF is feed from the right side.

For the case that the electron bunch length is much shorter than the RF wavelength of the deflecting cavity and the bunch center propagates through the structure at the "zero" RF phase, the strength of the deflection of each longitudinal slice of the bunch can be estimated. With these conditions the deflecting angle of each electron depends linearly on its longitudinal coordinate inside the bunch.

The basic operation principle of the TDS is illustrated in Fig. 4.4. An electron bunch propagates from the left to the right side, passing through the deflecting structure. After a drift space it is imaged on an observation screen. The structure deflects the electrons of the bunch vertically in linear dependence on their longitudinal coordinates within the bunch, which as a result enables measurements of the longitudinal bunch properties.

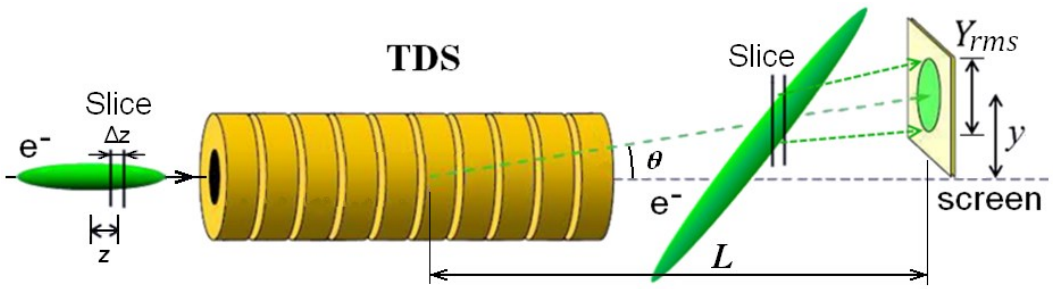

Fig. 4.4: Illustration of the TDS operation principle. An electron bunch propagates from the left to the right side, passing through the deflecting structure. After a drift space it is imaged on a screen. A bunch longitudinal slice with length Δz at the position z, relative to the bunch center, is deflected by the cavity and is imaged on the screen having, as a result, mean vertical position y and vertical size Y_{rms}.

Let's assume Δz that initially there is a slice of the electron bunch with length Δz and with longitudinal position inside the bunch z relative to the bunch center (see Fig. 4.4). As the bunch propagates through the structure, the mean vertical position of the slice at the observation screen downstream the cavity can be obtained as:

$$y = tan(\theta) \cdot L = \frac{\Delta p_{\perp}}{p} \cdot L = \frac{eV_0 k}{pc} z \cdot L, \tag{4.4}$$

where θ is the deflection angle, L is the drift distance between the TDS center and the screen, $\Delta p_{\perp}$ is the transverse momentum applied to the slice by the TDS cavity, p is the bunch longitudinal momentum, e is the electron charge, V_0 is the amplitude of the deflecting voltage, k is the wave number ($k = 2\pi f/c$), f is the RF frequency, c is the speed of light. Here it was also assumed that the TDS is much shorter than the drift space between the TDS and the screen afterwards. Introducing the TDS shear parameter S as:

$$S = \frac{eV_0 k}{pc} L, \tag{4.5}$$

one can get that the slice vertical position on the screen as:

$$y = S \cdot z. \tag{4.6}$$

From Eq. (4.6) one can see that the vertical position of the bunch slice on the screen is proportional to the slice position within the bunch, and the coefficient of proportionality is the TDS shear parameter. In the general case, if there are magnetic elements between the TDS and the observation screen, the shear

parameter can be calculated using the matrix formalism introduced in section 0. From Eq. (2.22), using the matrix element $M_{1,2}$ one can get the shear parameter as [34]:

$$S = \sqrt{\beta_y(s) \cdot \beta_y(s_0)} \cdot sin(\Delta\psi_y) \cdot \frac{eV_0 k}{pc}, \tag{4.7}$$

where $\beta_y(s)$ is the vertical beta function at the observation screen, $\beta_y(s_0)$ is the vertical beta function at the TDS center, $\Delta\psi_y$ is the vertical betatron phase advance defined between the TDS center and the observation screen and s is the longitudinal coordinate along the beamline.

4.2 Longitudinal resolution

Due to the deflection of the electron bunch by the TDS cavity the vertical size of the longitudinal slices, at the position of observation screen, will be defined not only by the beam emittance and the beamline optics but also by the slice length upstream and the strength of the deflection introduced by the TDS [35]:

$$Y_{rms}{}^2 = \beta_y(s) \cdot \varepsilon_y + (S \cdot \Delta z)^2, \tag{4.8}$$

where ε_y is the vertical geometrical emittance at the screen position, $\beta_y(s)$ is the vertical beta function at the screen position, Δz is the slice length and S is the TDS shear parameter.

Knowing the slice vertical position on the screen and its vertical size, one can estimate the longitudinal resolution. Assume that there are two slices. The first is at the bunch center, the second one has a longitudinal position z_1 within the bunch, relative to the bunch center and they both have a length of Δz. In order to resolve these two slices on the screen downstream the TDS cavity, it is necessary that the vertical position of the second slice on the screen is bigger than the vertical size of the first slice. From Eq. (4.4) and Eq. (4.8) one can obtain:

$$S \cdot z_1 \geq \sqrt{\beta_y(s) \cdot \varepsilon_y + (S \cdot \Delta z)^2}. \tag{4.9}$$

With the assumption that the slice length is negligible the distance between the two slices must be bigger than:

$$z_1 \geq \frac{\sqrt{\beta_y(s) \cdot \varepsilon_y}}{S}, \tag{4.10}$$

or, in the general case the shear parameter S from Eq. (4.7) can be included so that:

$$z_1 \geq \frac{\sqrt{\varepsilon_y}}{\sqrt{\beta_y(s_0)} \cdot sin(\Delta\psi_y)} \cdot \frac{pc}{eV_0 k}. \tag{4.11}$$

The obtained parameter z_1 corresponds to the minimal distance between two slices which can be resolved in such measurements, i.e. the longitudinal resolution.

An example of the dependence of the longitudinal resolution as a function of the TDS total deflecting voltage for different vertical beam size in the TDS is shown in Fig. 4.5 for a beam geometrical emittance of $\varepsilon_y = 2.2 \cdot 10^{-2}$ mm mrad (normalized $\varepsilon_N \sim 1$ mm mrad), beta function phase advance between the TDS and the screen $\Delta\psi_y = 110°$, particle momentum $p = 23$ MeV/c, and RF frequency of the TDS $f_{RF} = 3$ GHz..

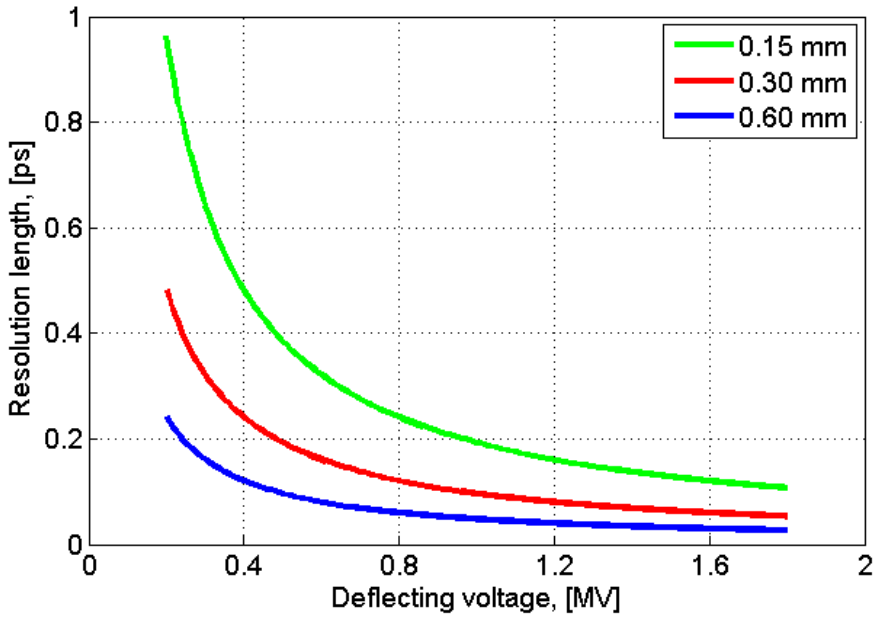

Fig. 4.5: TDS longitudinal resolution as a function of the total deflecting voltage of the TDS cavity for a vertical beam size in the TDS of 0.15 mm – the green curve, 0.3 mm – the red curve and for 0.6 mm – the blue curve.

From this plot one can see that with a higher deflecting voltage the longitudinal resolution gets better. Moreover, analyzing Eq. (4.11), one can see that a bigger beta function in the TDS, i.e. a bigger beam size, will give a better (smaller) longitudinal resolution, Fig. 4.5.

4.3 Induced slice momentum spread

The working principle of the TDS cavity is based on the Panofsky-Wenzel theorem [36]. The theorem states that the longitudinal gradient of the transverse force is proportional to the transverse gradient of the longitudinal force:

$$\frac{\partial}{\partial z} F_{\perp} = -\nabla_{\perp} F_{\parallel}. \tag{4.12}$$

In other words, transverse streaking is possible only when a transverse gradient of the longitudinal field is present.

In a cylindrical coordinate system for the lowest order deflecting mode of the RF field of the TDS cavity, first order solution gives the longitudinal component of the electric field as [29]:

$$E_z(r, \varphi, z) = E_0\, k\, r\, cos(\varphi), \tag{4.13}$$

where r, φ, z are the cylindrical coordinates, E_0 is electric field amplitude, k is wave number. This field has 90° phase advance relative to the deflecting force and for the zero crossing phase is at maximum. As a result from Eq. (4.13), the additional longitudinal momentum of the particle, which have non-zero vertical coordinate can be calculated as:

$$\Delta p_{\parallel} = \int eE_z(r, \varphi, z)\, dt = \int eE_0\, k\, y\, \frac{dz}{c} = y \int eE_0\, k \frac{dz}{c}, \tag{4.14}$$

where $r\, cos(\varphi) = y$. Introducing the TDS total deflecting voltage as:

$$V_0 = \int E_0\, dz, \tag{4.15}$$

and dividing both parts of the Eq. (4.14) by the beam momentum p_0, the relative RMS TDS induced momentum spread for the whole electron bunch is:

$$\sigma_{\delta} = \frac{eV_0 k}{p_0 c} \cdot \sigma_y. \tag{4.16}$$

An example of the slice momentum spread downstream the TDS cavity as a function of the TDS cavity deflecting voltage is shown on the Fig. 4.6 for several vertical RMS beam sizes inside the cavity (see section 5.3.2 and Fig. 5.14), RF frequency f_{RF} = 3.0 GHz and beam mean momentum p_0 = 23 MeV/c. From this plot one can see that the TDS induced slice momentum spread is linearly growing with the deflecting voltage in contrast to the longitudinal resolution, see Fig. 4.5. As a result, for the vertical beam size of 0.3 mm and for maximum TDS deflecting voltage of 1.7 MV, the TDS induced slice momentum spread is about 32 keV/c.

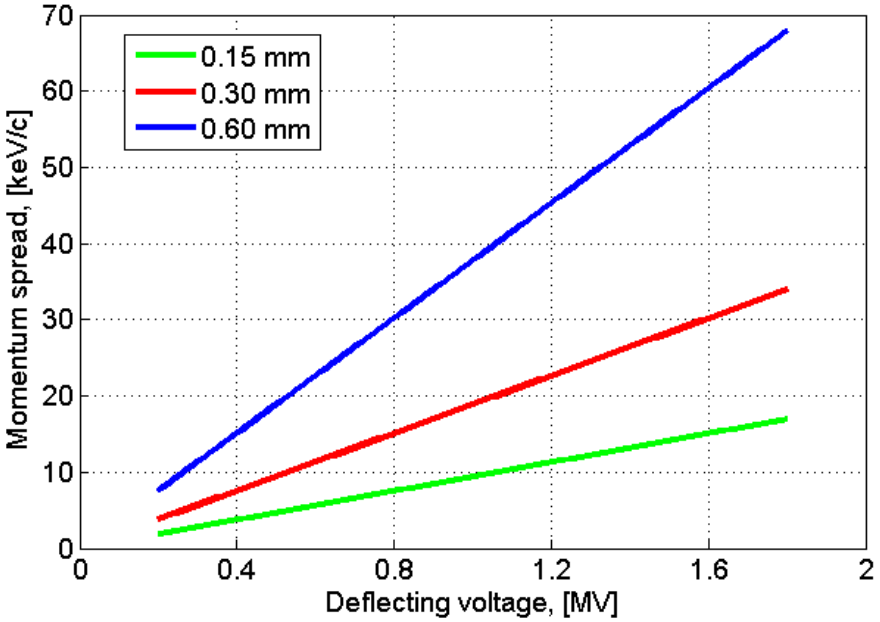

Fig. 4.6: The TDS induced slice momentum spread as a function of the total deflecting voltage of the TDS cavity for a vertical RMS beam size in the TDS of 0.15 mm – the green curve, 0.3 mm – the red curve and for 0.6 mm the blue curve.

Also a higher value of the vertical beta function in the TDS (or the vertical beam size σ_y) will result in higher induced momentum spread, or in other words, maintaining a small beam size in the TDS cavity will minimize the induced slice momentum spread.

4.4 TDS transport matrix

For beam transport studies in the vertical deflecting direction and the longitudinal phase space, the propagation of the beam through the TDS cavity can be represented by the four-dimensional transport matrix [37]:

$$\begin{pmatrix} y \\ y' \\ z \\ \delta p \end{pmatrix} = \begin{bmatrix} 1 & L_s & \frac{KL_s}{2} & 0 \\ 0 & 1 & K & 0 \\ 0 & 0 & 1 & 0 \\ K & \frac{KL_s}{2} & \frac{K^2 L_s}{6} & 1 \end{bmatrix} \cdot \begin{pmatrix} y \\ y' \\ z \\ \delta p \end{pmatrix}_0 , \tag{4.17}$$

where L_s is the structure length and $K = eV_0k/p_0c$, k is the wave number ($k = 2\pi f/c$), y and y' are the vertical coordinate and divergence, z and δp are the longitudinal coordinate and the relative momentum deviation, respectively. For the horizontal, not deflecting, plane the TDS acts like a drift space with length L_s, as it was described in section 2.2.1.

4.5 TDS calibration

In order to perform different measurements with the TDS cavity one needs to know the TDS shear parameter S defined in Eq. (4.5) and Eq. (4.7). It can be calculated from Eq. (4.7) or it can be measured in an experiment. The vertical mean position of the electron bunch on the observation screen downstream the TDS cavity depends on the phase of the TDS RF field at which the electron bunch propagates (see section 4.1). Let's assume that the bunch enters later than the "zero" RF phase with a time delay of Δt. In other words, the bunch is shifted longitudinally by length of $\Delta z = \beta c \cdot \Delta t$ from the "zero phase" field, see Fig. 4.7.

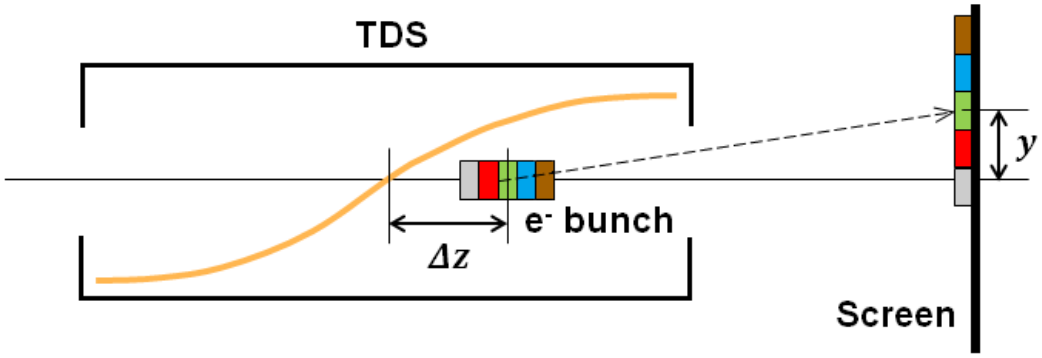

Fig. 4.7: Illustration of the TDS calibration principle. The bunch propagates from left to right. The bunch center of mass is shifted by Δz relative to the RF "zero phase" of the deflecting field (yellow curve). As a result, the bunch is deflected vertically by y on the observation screen.

As a result, the whole bunch will get a transverse kick and the resulting vertical mean position on the screen can be calculated from Eq. (4.4):

$$y = S\,\beta c\,\Delta t, \tag{4.18}$$

where S is the TDS shear parameter, βc is the speed of the bunch. If one rewrites the time delay in terms of the RF phase delay of $\Delta\varphi = 2\pi f \Delta t$, then:

$$y = S\,\beta c\frac{\Delta\varphi}{2\pi f} = S\,\beta c\frac{\Delta\phi}{360^o\,f}, \tag{4.19}$$

where $\Delta\phi$ is the RF phase delay in degrees, f is the RF frequency. From Eq. (4.19) one can see that the vertical mean position of the bunch on the screen depends linearly on the TDS RF phase.

As a summary, to measure the TDS shear parameter in an experiment, one should measure the vertical mean position on the screen as a function of the TDS RF phase. A linear fit of the data will result in the TDS shear parameter S:

$$S = K\frac{360^o \cdot f}{\beta c}, \tag{4.20}$$

where K is the first order term of the linear fit, i.e. slope. An example of a simulation of the TDS calibration for a deflecting voltage of V_0 = 0.15 MV is shown in Fig. 4.8.

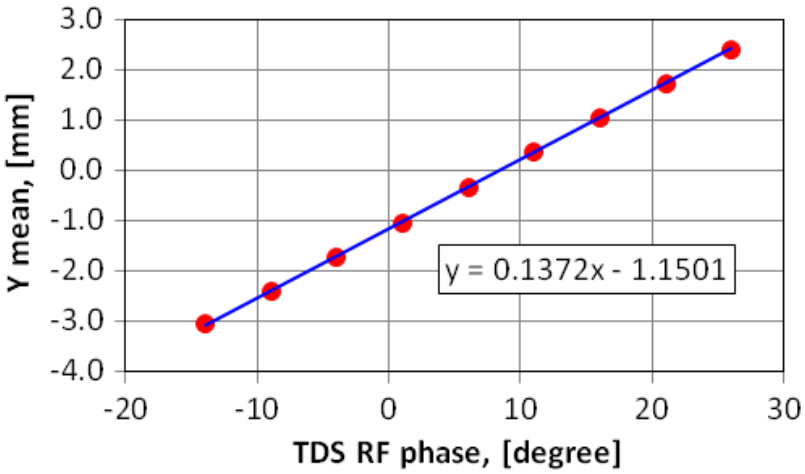

Fig. 4.8: TDS calibration at the observation screen PST.Scr1, located 12.278 m downstream the gun, for a deflecting voltage of the cavity of 0.15 MV. The bunch vertical mean position as a function of the TDS RF phase is shown with red dots and a linear fit is shown with the blue line.

The vertical axis in Fig. 4.8 corresponds to the vertical mean position of the electron bunch on the screen and the horizontal axis corresponds to the TDS RF phase in degrees. From the linear fit of the data one can calculate the slope as K = 0.1372 mm/deg. For an RF frequency of f = 3 GHz and β = 1, Eq. (4.20) gives the TDS shear parameter S = 0.494.

Chapter 5

Simulations of measurements with the TDS

The TDS installed at PITZ will allow to perform the following measurements of the electron bunch:

- longitudinal bunch profile measurements,
- transverse slice emittance measurements,
- longitudinal phase space measurements.

Numerical simulations reproducing all the measurement procedures with the TDS can be performed using the particle tracking code ASTRA [38].

Since a bunch charge of 1 nC is mostly studied at PITZ [4] and will be used as the nominal charge for the operation of the European XFEL [5], all simulations presented in this chapter were performed for 1 nC bunch charge and about 23 MeV/c bunch mean momentum as typical for PITZ.

5.1 Longitudinal bunch profile measurements

The TDS cavity installed at PITZ will give the possibility to measure the bunch length and the longitudinal profile with high time resolution. For such measurements one needs to focus the beam vertically on one of the observation screens downstream the TDS and then switch on the TDS. As a result, the vertical profile of the beam image on the screen will correspond to the longitudinal profile of the beam.

5.1.1 Measurement setup

The part of the PITZ beamline related to the bunch length measurement is shown in Fig. 5.1. Six quadrupole magnets High1.Q1 – Q6 upstream the TDS cavity can be used for the beam matching and focusing. The quadrupole PST.QM1 located downstream the TDS can be used for additional beam focusing on the observation screen PST.Scr1 – the first observation screen downstream the TDS cavity at 12.278 m from the gun.

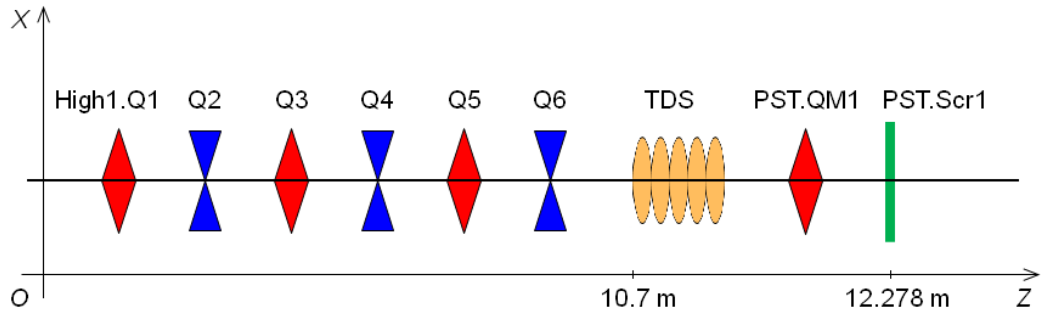

Fig. 5.1: Measurement setup for bunch length measurements with the TDS cavity. The beam propagates from left to right.

The distance between the TDS center and observation screen PST.Scr1 is 1.278 m and is sufficient to stretch the 6 mm long bunch up to 36 mm vertically (the size of the observation screen), see Eq. (4.5), for the maximal TDS deflecting voltage of 1.7 MV. Also the inner diameter of the beam pipe of 35 mm is limiting further stretching of the bunch.

5.1.2 Beam transport

The main goal of the beam transport is to focus the beam vertically on the observation screen downstream the TDS, see Fig. 5.1, so that the highest longitudinal resolution (see section 4.2) is obtained. Fig. 5.2 shows an example of such a beam transport for 1 nC bunch charge where the bunch transverse RMS size is given as a function of the longitudinal coordinate along the beamline. High1.Q1, Q2, Q3, Q5 and Q6 quadrupoles were used (see Fig. 5.1).

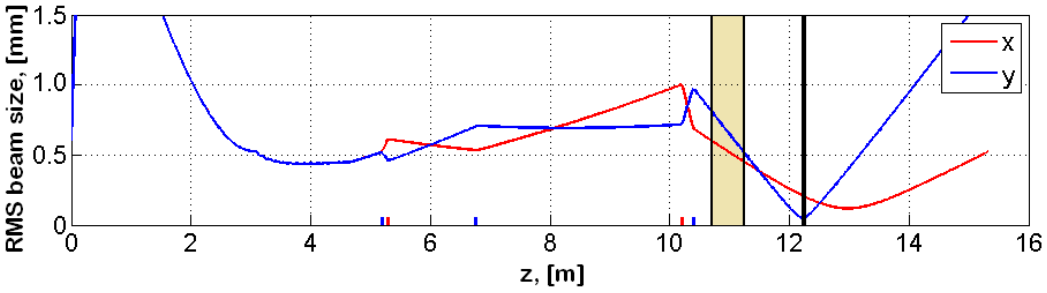

Fig. 5.2: Transverse RMS size of the electron bunch along the beamline for bunch length measurements. The red curve shows the horizontal and the blue curve shows the vertical bunch RMS size. The yellow stripe shows the TDS position. The vertical black line at about 12 m shows the position of the observation screen PST.Scr1.

The vertical size of the electron beam on the observation screen, achieved in this example, is 50 μm. According to inequality (4.10) this will result in a longitudinal resolution of 8 μm for maximum TDS deflecting voltage V = 1.7 MV, which corresponds to TDS shear parameter of $S = 6.2$.

For measurements of the longitudinal profile it is not needed to have a small transverse size in the TDS cavity as it is required for longitudinal phase space measurements, see sections 4.3 and 5.3.2, since the induced slice energy spread has only neglectable influence on the longitudinal bunch profile measurements.

5.1.3 Simulation results

As it was already mentioned, the first step before the measurements is to obtain the TDS shear parameter for a certain observation screen, i.e. do the TDS calibration. The TDS shear parameter calculated from the calibration for a 0.15 MV deflecting voltage is $S = 0.51$ according Eq. (4.20). Assuming a linear dependence of the shear parameter on the TDS deflecting voltage, see section 4.1, 0.6 MV deflecting voltage will correspond to a TDS shear parameter $S = 2.0$ and 1.2 MV will correspond to a shear parameter $S = 4.1$.

Results of the simulated beam images on the observation screen PST.Scr1 for 1 nC bunch charge and three different TDS deflecting voltages of 0.0 MV, 0.6 MV and 1.2 MV are presented in Fig. 5.3.

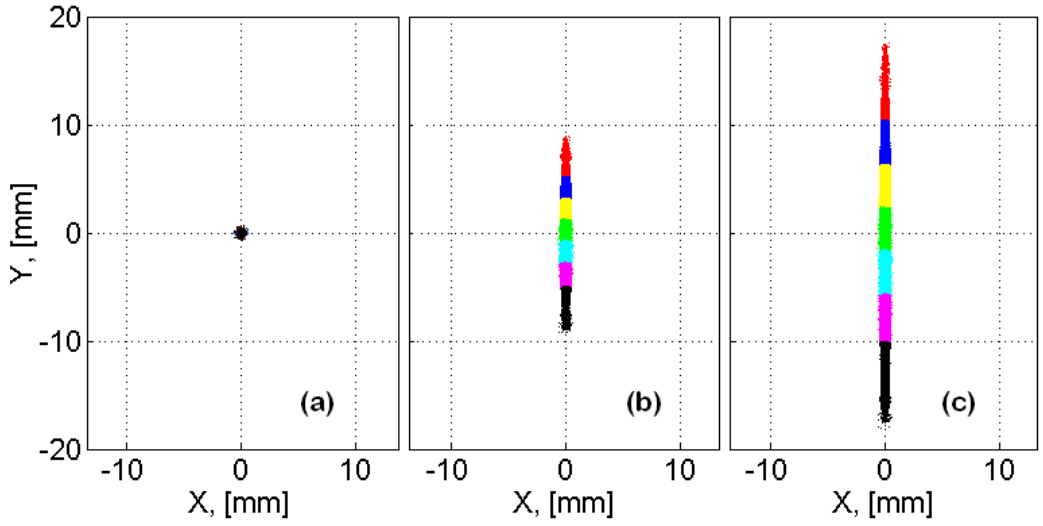

Fig. 5.3: Beam images on observation screen PST.Scr1 for 0.0 MV (a), 0.6 MV (b) and 1.2 MV (c) TDS deflecting voltage.

The color code in this figure is used for illustration and represents how the seven subsequent longitudinal slices of the electron bunch having equal charges are distributed on the screen. The picture in Fig. 5.3 (a) shows the beam image on the

PST.Scr1 when the TDS is switched off. From this image one can obtain bunch transverse sizes and, from the vertical size of 50 μm one can estimate the longitudinal resolution knowing the TDS shear parameter. The picture in Fig. 5.3 (b) shows the beam image with the TDS switched on and a TDS deflecting voltage of 0.6 MV. According to the calibration, this voltage corresponds to a TDS shear parameter S = 2.0 and, thus, the longitudinal resolution for this case is 25 μm or 80 fs. The picture in Fig. 5.3 (c) shows the beam image with a TDS deflecting voltage V = 1.2 MV, which corresponds to a TDS shear parameter S = 4.1. This will give a longitudinal resolution of 12 μm or 40 fs.

The resulting bunch longitudinal profile is shown in Fig. 5.4 with the red curve. The profile is calculated as the vertical profile of the beam image, shown in Fig. 5.3 (c) and scaled with the TDS shear parameter S = 4.1 to get longitudinal coordinate within the bunch, see Eq. (4.6). The original bunch longitudinal profile (calculated from the simulated particle distribution) is shown in Fig. 5.4 with the blue curve. Both profiles are calculated dividing the range of the longitudinal axis from -5 mm to 5 mm into 200 longitudinal slices with the slice length of 50 μm. On the observation screen it corresponds to the vertical distance of 0.2 mm, which is resolvable with this screen, which resolution is about 20 um.

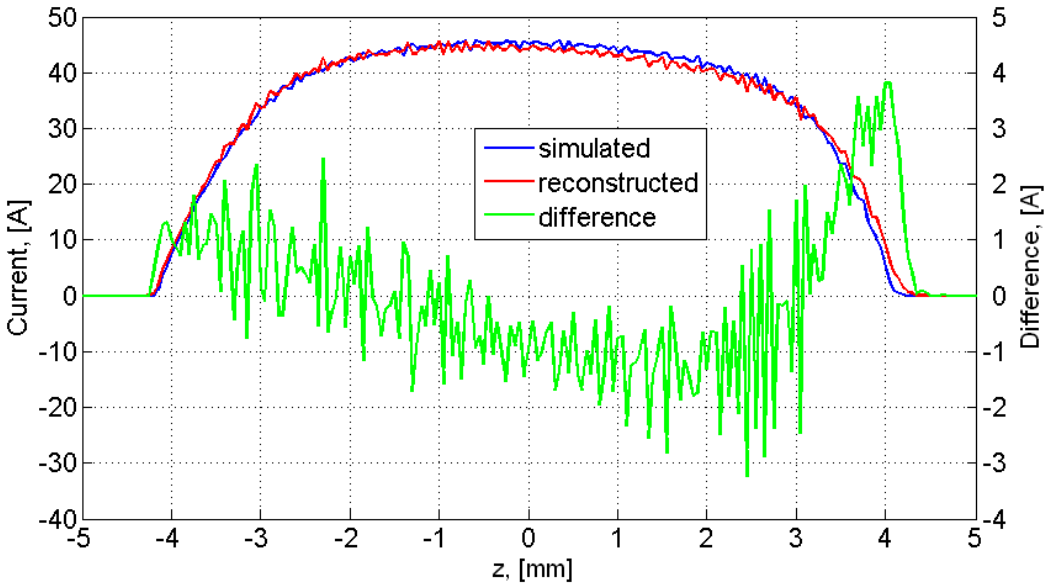

Fig. 5.4: Comparison of the reconstructed bunch longitudinal profile, shown with the red curve, with the original (simulated) one, shown with the blue curve. The difference between two profiles is shown with the green curve. The plots are normalized to the bunch charge to show the current distribution.

The simulation results of the bunch longitudinal profile measurements, presented in Fig. 5.4, show good agreement between the reconstructed bunch

longitudinal profile and the original simulated one. The maximal difference between two profiles is about 4 A, the green curve in Fig. 5.4. The reconstructed bunch longitudinal profile, the red curve in Fig. 5.4, is a bit longer than the original simulated one, the blue curve, what come from the limited resolution of this measurement, e.g. not zero vertical beam size on the observation screen with the TDS switched off. The noise in the reconstruction and in the difference, Fig. 5.4, comes from the relative low particle statistics for such detailed binning: for this simulation 200000 particles were used.

5.2 Slice emittance measurements

As the TDS deflects the beam vertically, it will allow measurements of the horizontal slice emittance. As a result of such vertical deflection, the vertical axis of the beam image on the screen will contain information about the longitudinal profile of the bunch and will be used to define the longitudinal slices within the bunch. The horizontal axis will correspond to the horizontal sizes of the defined longitudinal slices of the bunch. Using the resulting bunch image on the screen the slice emittance can be calculated applying the quadrupole scan emittance measurement technique to the horizontal slice of each longitudinal slice, as it was described earlier in section 2.2.2.

5.2.1 Measurement setup

The part of the PITZ setup dedicated to the slice emittance measurements with the TDS is the same as for the bunch length measurements shown in Fig. 5.1. Five quadrupole magnets High1.Q1 – Q5 upstream the TDS cavity will be used for the beam matching up to the TDS. The last quadrupole in front of the TDS – High1.Q6 will be used to perform the quadrupole scan for the horizontal axis on the first observation screen PST.Scr1 downstream the TDS.

With the TDS switched on different electron bunch longitudinal slices will receive different vertical kicks from the deflector and as a result they will have different vertical coordinates on the observation screen. Measuring the horizontal sizes of each of them as a function of the current of the quadrupole High1.Q6 gives the necessary information to obtain the emittance value from the quadrupole scan. The procedure of measuring the horizontal size of each slice and estimation of how many slices can be resolved will be described in the following sections.

5.2.2 Beam transport

An example of the vertical and the horizontal RMS beam sizes along the beamline are shown in Fig. 5.5. The idea of the beam transport here is to realize the quadrupole scan for the horizontal beam size on the observation screen

downstream the TDS while the vertical beam size is kept small in order to obtain high longitudinal resolution, i.e. to resolve more longitudinal slices.

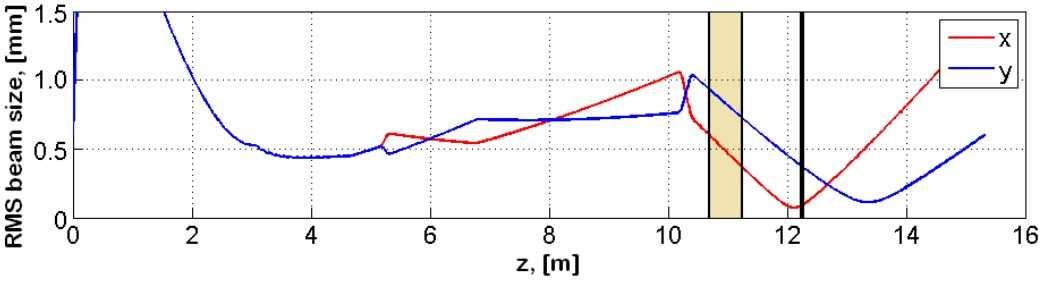

Fig. 5.5: Transverse RMS size of the electron bunch along the beamline for slice emittance measurements. The red curve shows the horizontal and the blue curve shows the vertical RMS bunch sizes. The TDS cavity is shown as a yellow stripe and the observation screen PST.Scr1 is shown as a single vertical black line at about 12 m.

5.2.3 Measurement procedure

For the slice emittance measurements the image of the bunch on the observation screen is cut in several horizontal stripes having vertical width *dY*, see Fig. 5.6, which will correspond to the bunch longitudinal slices. Each color of the bunch part in this figure corresponds to one of seven longitudinal bunch slices with equal charge, chosen in front of the quadrupole.

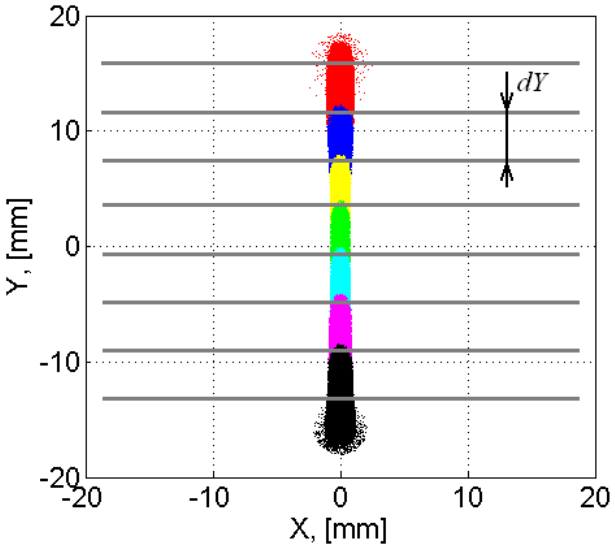

Fig. 5.6: Bunch image on the observation screen downstream the TDS cavity. The seven colors represent seven consequent longitudinal slices of the bunch with equal charge. The image is cut in equal horizontal stripes with width *dY*.

From this figure, one can see that the border between two consequent slices is not a perfect horizontal line: the slices are overlapping with each other. This effect comes from the not-zero vertical beam size when the TDS is switched off and will limit the temporal resolution for such measurements.

After the image is cut, see Fig. 5.6, the emittance calculation can be performed for each horizontal stripe separately using the quadrupole scan. The vertical position of a stripe on the screen, divided by the TDS shear parameter (see section 4.1), will give the longitudinal position of the corresponding slice within the bunch. As a result, the slice emittance as a function of the slice longitudinal coordinate within the bunch can be obtained. The connection between the stripes and longitudinal slices is not perfect, defined stripe width *dY* will not strictly correspond to the slice length, see section 5.2.5. Moreover during the quadrupole scan some particles from the one stripe may come to the neighboring stripe.

5.2.4 Simulation results

An example of the simulated quadrupole scan for the middle slice of the bunch is presented in Fig. 5.7, where the red diamonds are the squared horizontal slice RMS size σ_x^2 shown as a function of the quadrupole gradient. The data are fitted with a second order polynomial, which will give in result emittance value as it was described in section 2.2.2.

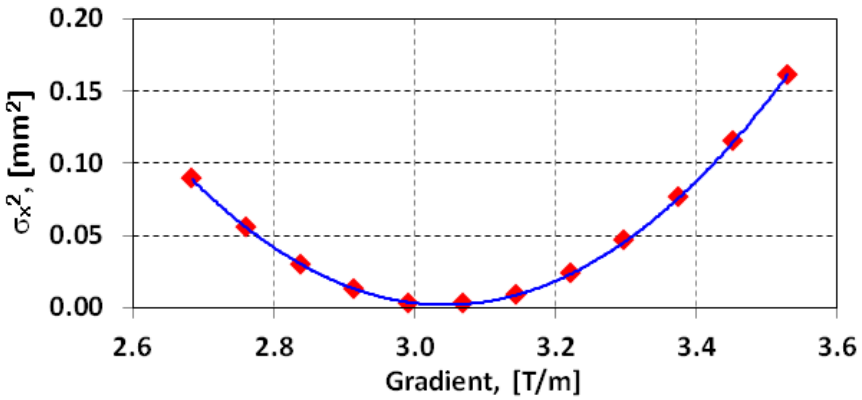

Fig. 5.7: An example of a quadrupole scan for the middle slice of a bunch. The red rhombs correspond to simulation data, the blue curve is a second order polynomial fit.

A result of the calculated slice emittance for 17 slices is shown in Fig. 5.8, where the red triangles are the calculated slice emittance using the quadrupole scan, i.e. simulated measurements, and the blue diamonds are the slice emittance calculated directly from the simulated particles distribution.

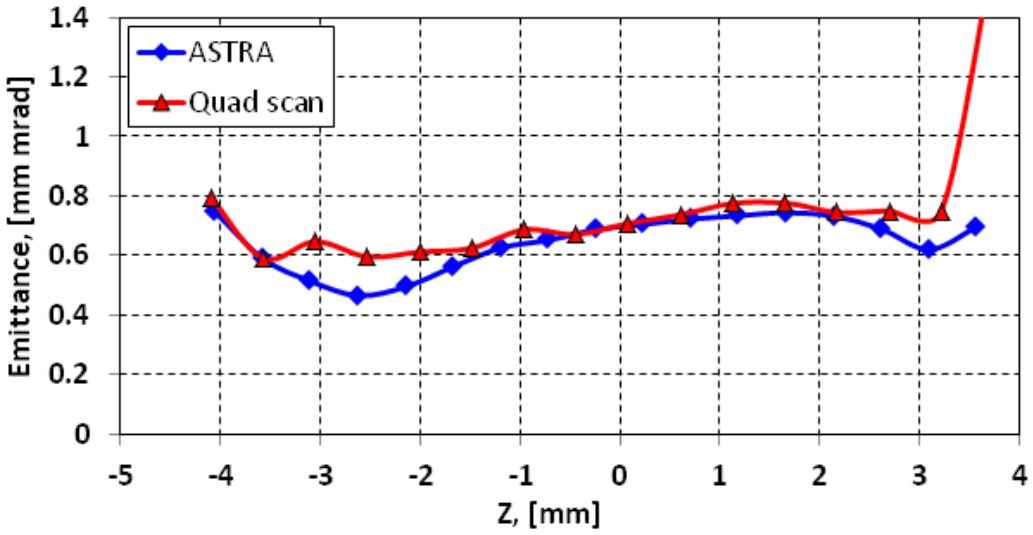

Fig. 5.8: Simulated slice emittance measurements using quadrupole scan (red triangles, Quad scan) and simulated initial slice emittance (blue diamonds, ASTRA) with space charge forces taken into account.

These results show that there is almost no difference between the calculated and the initial slice emittance in the middle of the bunch, for slices between -1 and +1 mm. This difference grows towards the head and the tail of the bunch and can be explained by the presence of space charge forces which are not taken into account in the quadrupole scan analysis and this can be proven by additional simulations. It can also arise from the bunch energy spread as the electrons in the bunch have different energy and thus all the electrons together cannot be focused perfectly like a mono-energetic beam, i.e. from chromatic effect. A simulation with a mono-energetic beam doesn't show a big difference in the calculated slice emittance values using a quadrupole scan: the energy spread in the bunch being in the order of 100 keV is sufficiently small.

In Fig. 5.9 results of the calculated slice emittance are shown for the simulation without taking into account the space charge forces. This figure shows that the calculated slice emittance from the quadrupole scan is in a good agreement with the simulated initial one.

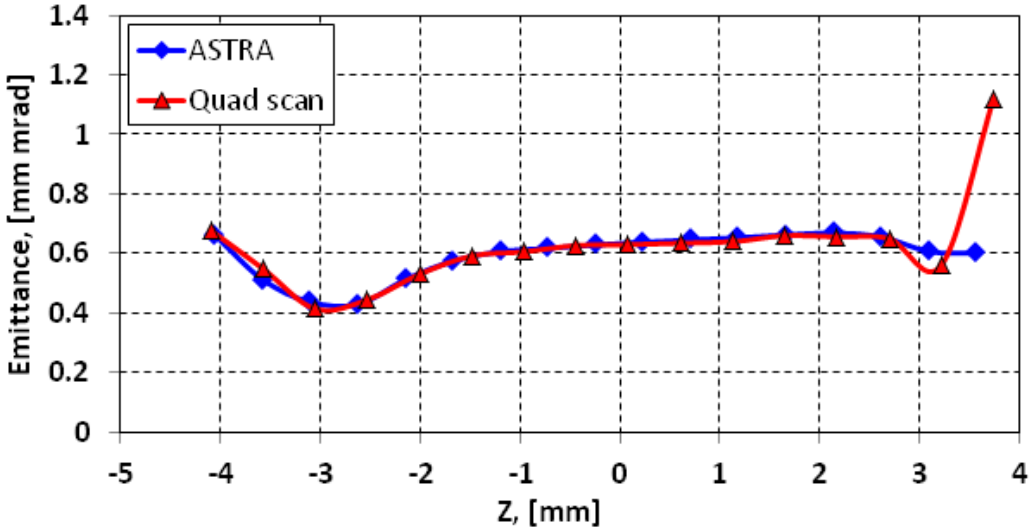

Fig. 5.9: Simulated measured slice emittance from the quadrupole scan (red triangles, Quad scan) and simulated initial slice emittance (blue diamonds, ASTRA) without space charge forces taken into account.

5.2.5 Longitudinal resolution of the slice emittance measurements or how to define slices

An estimation of the longitudinal resolution σ_z of the slice emittance measurements can be done in a way similar to Eq. (4.10):

$$\sigma_z = \sigma_y / S, \tag{5.1}$$

where S is the TDS shear parameter and σ_y is the vertical beam size on the observation screen with the TDS switched off. A measurement of this resolution can easily be done during the experiment together with the TDS calibration, as it was discussed in section 4.5.

A more precise way to estimate the longitudinal resolution in simulations is to restore the longitudinal coordinates of all the particles lying in one stripe on the screen when the whole bunch is at the position of the quadrupole entrance. Such a procedure is illustrated in Fig. 5.10.

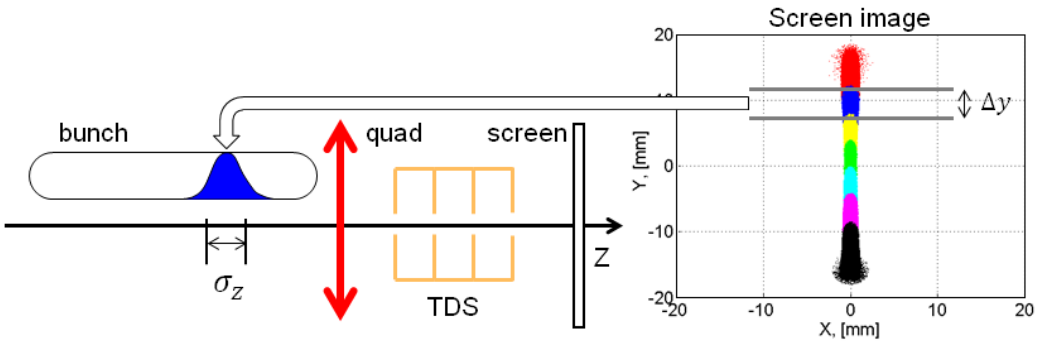

Fig. 5.10: An estimation of the bunch longitudinal slice length for slice emittance measurements. The distribution of particles, which vertical coordinates are within the stripe of width Δy on the observation screen, is shown upstream the quadrupole with the blue area within the bunch and it has RMS length of σ_z.

The longitudinal coordinates of the particles, whose vertical coordinates are within a stripe on the observation screen, see the right side of Fig. 5.10, are restored and shown as a blue histogram within the bunch on the left side. The calculated standard deviation σ_z of these longitudinal coordinates represents the RMS length of the slice which corresponds to the longitudinal resolution for the current stripe width of Δy.

When one will decrease the stripe width Δy to have higher resolution, at some point the resolution will not grow anymore. It will happen at the stripe width equal to the vertical beam size on the screen with the TDS switched off. The simulated histograms of the particles longitudinal distributions in one longitudinal slice are shown in Fig. 5.11 for the different stripe widths of Δy = 0.125, 0.25, 0.5, 1.0, 2.0 mm. As one can see from the stripe width of 2 mm and down to 0.25 mm the width of the histogram is decreasing. But for 0.25 and 0.125 mm it is not changing significantly. In other words, while the stripe width Δy remains bigger than the vertical beam size σ_y with the TDS switched off, the resolution length is close to the stripe width Δy divided by the TDS shear parameter. As the stripe width Δy becomes equal or smaller than the vertical beam size $\sigma_{y,0}$ with the TDS switched off, the longitudinal resolution is limited by the beam size $\sigma_{y,0}$ divided by the TDS shear parameter, according Eq. (4.10). The dependence of resolution length on the stipe width Δy is shown in Fig. 5.12.

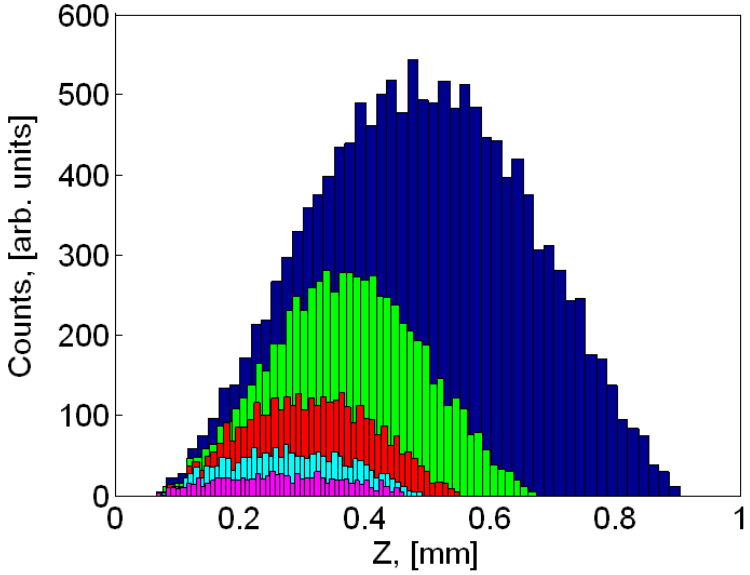

Fig. 5.11: Histograms of the particles longitudinal distribution in one slice which corresponds to one stripe with width Δy of 2 mm (blue), 1 mm (green), 0.5 mm (red), 0.25 mm (cyan) and 0.125 mm (magenta).

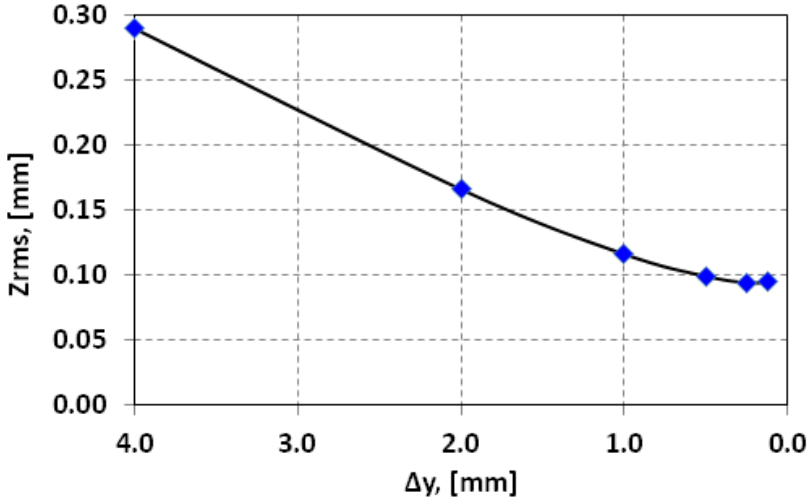

Fig. 5.12: Slice RMS length as a function of the horizontal stripe width Δy.

From this plot one can see, that for a stripe width Δy of 0.5 mm and less the obtained slice RMS length remains almost constant and does not decrease anymore with the decrease of the stripe width. Therefore, the maximal achievable resolution can be estimated as 0.1 mm or 0.3 ps RMS. The optimal stripe width for slice emittance calculation is 0.5 mm, which results in about 70 slices for an electron bunch with about 20 ps duration.

5.3 Longitudinal phase space measurements

Besides using the streak camera in the dispersive sections [7], [8], in future measurements of the longitudinal phase space at PITZ can be done with the TDS cavity and the dipole magnet downstream with high temporal resolution as well as with high momentum resolution. In order to allow for such measurements the beamline optics should provide the possibility for focusing on the observation screen in the plane of deflection when the TDS cavity is switched off. According to Eq. (4.10) this condition would assure high temporal resolution. The beamline optics also should be optimized in such a way that it provides the conditions for the highest momentum resolution. Additionally, the TDS shear parameter has to be measured.

5.3.1 Measurement setup

The TDS cavity together with the first dipole of the HEDA2 section will be used for longitudinal phase space measurements, see Fig. 3.1, and a more detailed diagram of the setup elements related to the longitudinal phase space measurement is shown in Fig. 5.13. The resulting longitudinal phase space of the bunch will be observed on the first screen downstream the dipole magnet – Disp3.Scr1. The TDS entrance is located 10.7 m downstream the gun, the cavity length is about 0.6 m, the distance between the cavity center and the dipole entrance is about 6 m. The dipole Disp3.D1 has a bending radius of $\rho = 0.6$ m and a bending angle of $\theta = 60°$. The distance between the dipole exit and the observation screen Disp3.Scr1 is $L_d = 0.7$ m.

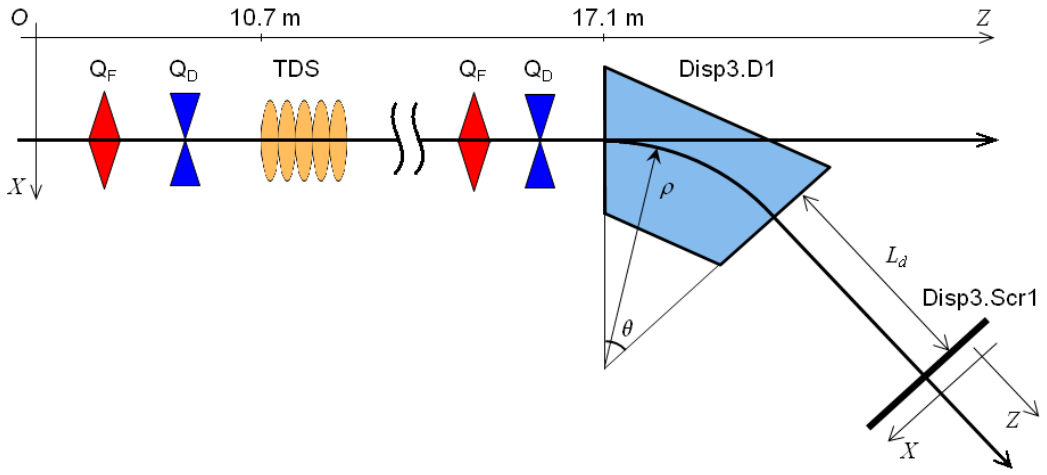

Fig. 5.13: Schematic setup for longitudinal phase space measurements with the TDS at PITZ. Disp3.D1 is a dipole magnet; Disp3.Scr1 is an observation screen. The beam propagates from left to right. The vertical axis Y points out from the drawing plane.

5.3.2 Measurement procedure

The following steps have to be done to perform longitudinal phase space measurements with the TDS cavity:

- beam transport to optimize the longitudinal and the momentum resolution;
- calibration of the TDS cavity for the beam transport found;
- measurements of the beam image on the observation screen.

First, to have the highest longitudinal resolution, the beam should have the smallest vertical size (the deflection plane of the TDS is vertical) on the observation screen Disp3.Scr1 downstream the dipole magnet. Also the beam should have a small transverse size in the TDS cavity in order to be less affected by the induced energy spread, see section 4.3. At the same time, the beam should be optimized in such a way that the momentum resolution is the highest.

Fig. 5.14 shows the transverse RMS sizes of the bunch along the beamline for the case of 1 nC bunch charge. The location of the TDS cavity is shown as a yellow color stripe between 10 and 12 m and the location of the dipole is shown as a light blue stripe between 17 and 18 m. For this plot the beam sizes were simulated without taken into account the dipole field.

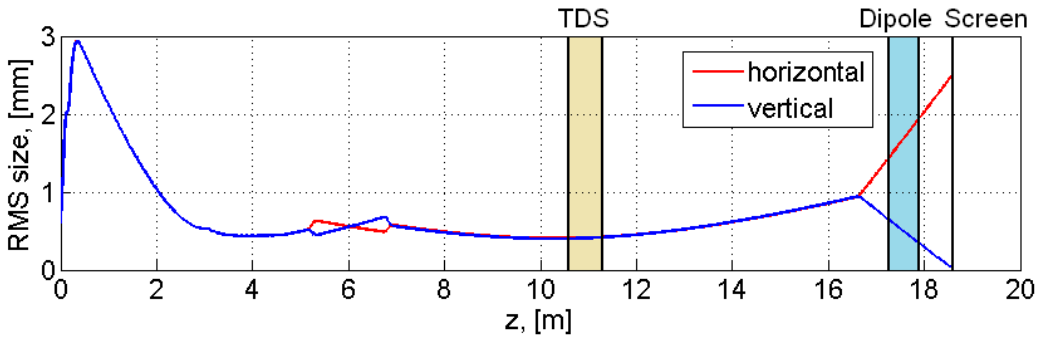

Fig. 5.14: Transverse RMS bunch sizes along the beamline for longitudinal phase space measurements. The red curve is the horizontal and the blue curve is the vertical bunch size. The yellow stripe shows the TDS, the light blue stripe shows the dipole and the black vertical line shows the observation screen at about 18.6 m.

For the beam transport four quadrupoles upstream the TDS (around 6 m) and one quadrupole downstream (around 17 m) are used to realize the small and round beam size in the center of the TDS and to reach a high longitudinal and momentum resolution on the observation screen correspondingly. The beam is focused vertically on the observation screen and the divergence of the beam in front of the dipole corresponds to the optimal one, see section 3.6. After the dipole the horizontal beam size on the observation screen will correspond to the RMS momentum spread in the bunch multiplied by the dispersion, Eq. (3.4).

As a next step before the measurements one needs to obtain the TDS shear parameter, i.e. to calibrate the longitudinal axis of the restored longitudinal phase space, see section 4.5. Using Eq. (4.20), one calculates the TDS shear parameter $S = 0.8$ for 0.6 MV deflecting voltage of the TDS. This parameter differs from the other type of measurements, sections 5.1 and 5.2, because of different beam transport.

After the calibration is done, the RF phase of the TDS should be set to the "zero" phase in order to have the beam vertical position at the screen center. An image on the screen downstream the Disp3.D1 dipole magnet will represent the longitudinal phase space. The vertical axis of the image corresponds to the longitudinal coordinate within the bunch, scaled with the TDS shear parameter, and the horizontal axis corresponds to the momentum.

5.3.3 Simulation results

Simulation results for a longitudinal phase space measurement are shown in Fig. 5.15 for 1 nC bunch charge. The left plot (a) shows the electron bunch longitudinal phase space upstream the TDS cavity. The middle plot (b) shows the bunch longitudinal phase space downstream the TDS in front of the dipole magnet. The right plot (c) shows the reconstructed longitudinal phase space from the beam image on the observation screen Disp3.Scr1 downstream the dipole magnet.

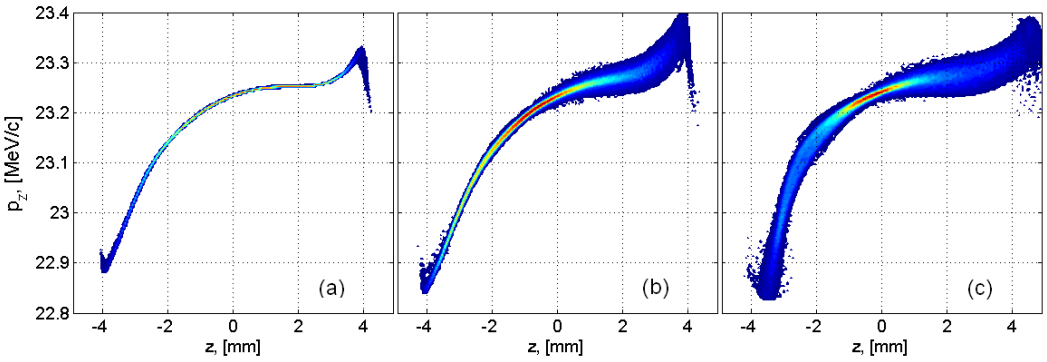

Fig. 5.15: Simulated longitudinal phase spaces for 1 nC bunch charge: in the front of the TDS (a), in front of the dipole magnet (b) and the reconstructed phase space at the position of the observation screen Disp3.Scr1 downstream the dipole (c).

The axis of the longitudinal coordinate within the bunch shown in Fig. 5.15 (c) was restored using Eq. (4.4) and the momentum axis was restored using Eq. (3.4).

The reconstructed longitudinal phase space shown in Fig. 5.15 (c) is wider and has slightly different shape from the original one, see Fig. 5.15 (a). This effect comes from the TDS induced energy spread, described in section 4.3, and from the limited resolution of the momentum measurement (see section 3.6).

In Fig. 5.16 the evolution of the slice momentum spread induced by the TDS cavity is shown. The blue curve shows the slice momentum spread at 10.0 m downstream the gun in front of the TDS cavity, corresponding to the longitudinal phase space from Fig. 5.15 (a), and the red curve is the slice momentum spread at 17.0 m downstream the gun in front of the dipole magnet, corresponding to the longitudinal phase space on Fig. 5.15 (b).

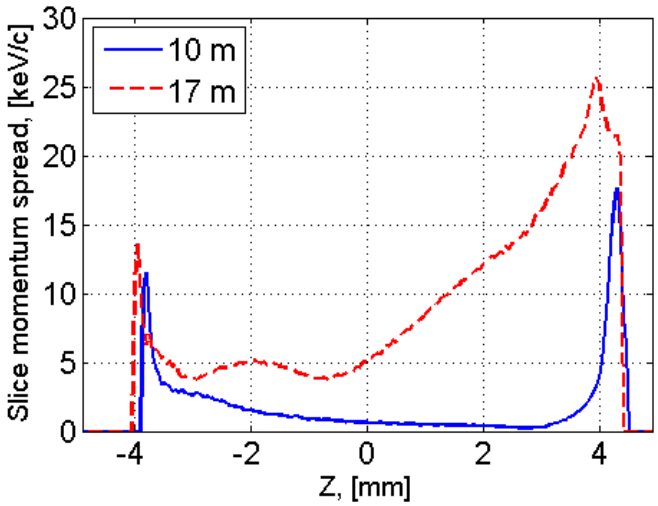

Fig. 5.16: Simulated slice momentum spread within the bunch: in front of the TDS at z = 10.0 m is shown with the blue curve and downstream the TDS in front of the dipole magnet at z = 17.0 m is shown with the red dashed curve.

The effect of the TDS induced momentum spread can be estimated from the beam parameters and the field amplitude in the TDS as it was described in section 4.3. The RMS beam size in the TDS cavity is about 0.4 mm, see Fig. 5.14. Using Eq. (4.16) for a TDS deflecting voltage of 0.6 MV, one can calculate an RMS induced momentum spread of 15 keV/c for 23 MeV/c beam momentum.

5.4 Summary

The simulations of longitudinal profile measurements using TDS cavity show consistent results. The achieved longitudinal resolution is about 17 μm and limited by the beam size on the observation screen and this screen resolution (12 μm from the transverse beam size plus 5 μm, came from the screen resolution of 20 μm dived by the TDS shear parameter).

Presence of the time jitter between the RF phase of the TDS cavity and the bunch can significantly reduce time resolution of the measurements. From the calibration shown in Fig. 4.8 one can see that RF phase jitter of 0.1 degree will cause the beam position jitter on the observation screen up to about 0.1 mm for

1.2 MV deflecting voltage. For single shot measurements it will not play a role because of the bunch will jitter entirely. But for multi shot measurements, which are required for the small bunch charges to have reasonable intensity from the observation screen, it will reduce temporal resolution. For the case shown in section 5.1.3 multi shot measurements with the RF phase jitter of 0.1 degree will make worse the temporal resolution from 40 fs to 120 fs.

For the simulations of the slice emittance measurements the reconstructed slice emittance using quadrupole scan is in good agreement with the original calculated one from the simulated particles distribution. They perfectly coincide if not taking into account the space charge forces in simulations, and with the space charge forces there are small discrepancies between them.

The achieved longitudinal resolution for the simulation of the longitudinal phase space measurements at PITZ for 1 nC bunch charge and about 8 mm bunch length is 0.1 mm (0.3 ps duration) with an TDS induced momentum spread of 15 keV/c over about 1 keV/c original spread. For such type of measurements one needs to take care of the quite strong influence of the longitudinal fields of the TDS cavity on the electron beam.

For example, at FLASH for a normalized transverse emittance of 2 mm mrad, transverse beam size in the TDS of 0.1 mm and 20 MV TDS deflecting voltage the longitudinal resolution will be 8 μm (27 fs) [39], [40]. With the same transverse emittance and increased transverse beam size up to 1 mm in the TDS at PITZ, for 1.8 MV TDS deflecting voltage the longitudinal resolution will be close to the FLASH case – 8.8 μm (30 fs). But, at FLASH, such a transverse beam size will result in 120 keV/c induced momentum spread for a 1.2 GeV/c beam, whereas at PITZ this will result in 115 keV/c for a 23 MeV/c beam. In relative terms, for PITZ this is 50 times worse: $5 \cdot 10^{-3}$ versus 10^{-4}, and will completely smear out the inner structure of the longitudinal phase space.

Chapter 6

Longitudinal phase space tomography

Tomography is an object reconstruction technique which uses any kind of penetrating wave or other ways to get projections of the object under different perspectives. The method is used in radiology, archaeology, biology, geophysics, oceanography, materials science, astrophysics, quantum information, and other sciences. In most cases it is based on a mathematical procedure called tomographic reconstruction. From its mathematical background tomography deals with a reconstruction of an N-dimensional function from a number of (N-1)-dimensional projections of this function [41]. For example, it can be represented as the mathematical reconstruction of an unknown two-dimensional object using its one-dimensional projections under different angles of observation or after applying different transformations to the object. From here on if not mentioned otherwise only two-dimensional functions will be used. In Fig. 6.1 a schematic example of taking a one-dimensional projection from a two-dimensional unknown object is shown.

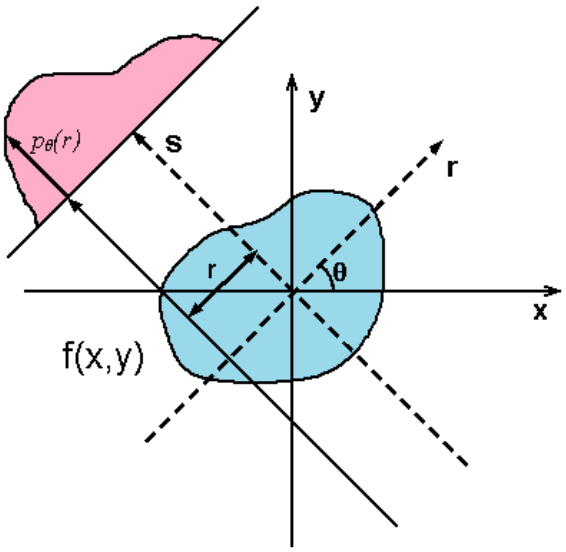

Fig. 6.1: Tomographic transformation illustration. $f(x,y)$ is an unknown 2D object shown with the blue area, $p_\theta(r)$ is one of the measured one-dimensional projections of the object taken at an observation angle θ. The θ angle varies in the range from 0 to π to obtain all possible projections.

In this figure, θ is the angle at which the projection $p_\theta(r)$ is taken, (r, s) is a rotated coordinate system and $p_\theta(r)$ is the projection of $f(x, y)$ on the r axis. Taking many projections $p_\theta(r)$ of the unknown object for $\theta \in [0, \pi]$, the unknown function $f(x, y)$ can be restored using tomographic reconstruction techniques, for example by algebraic reconstruction technique (ART) [42] or maximum entropy technique (MENT) [43].

Tomographic techniques can be deployed for measurements of the longitudinal phase space as the input projections correspond to the momentum spectra where the bunch energy chirp has been varied [9]. From the reconstructed longitudinal phase space, the electron bunch longitudinal profile and slice energy spread can be extracted and the longitudinal emittance can be calculated. The electron bunch longitudinal phase space at PITZ can be measured by varying the RF phase of the accelerating structure – the CDS booster. The momentum spectra measured downstream the booster at the HEDA1 or the HEDA2 dispersive sections (see sections 3.5 and 3.6) can be used to feed the tomographic reconstruction algorithm.

6.1 Algebraic Reconstruction Technique

One of the algorithms for tomographic reconstruction is the algebraic reconstruction technique (ART) [42]. In ART the two-dimensional object of reconstruction is defined as a two-dimensional matrix and is represented as one-dimensional array with density value g_l for each pixel l, see Fig. 6.2.

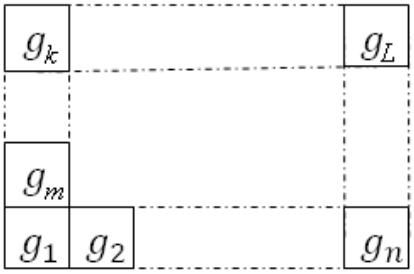

Fig. 6.2: Two-dimensional matrix representation of the object of reconstruction. The pixel numeration is done from left to right and from bottom to top. Here L is the total number of elements in the matrix and n is the number of elements in the horizontal line, i.e. number of columns, $m = n + 1$, $k = L - n + 1$ and L is multiple of n.

For all the projections p_{ij}, where i represents the projection number, e.g. viewing angle, and j represents the bin number of this projection, there is such a matrix a_{ijl} which relates the image pixel g_l, $l \in [1, L]$, to the projections by the following sum of all matrix elements:

$$p_{ij} = \sum_{l=1}^{L} a_{ijl} \cdot g_l. \tag{6.1}$$

In other words this matrix a_{ijl} represents the contribution of each g_l to p_{ij}. In the case of longitudinal phase space tomography the matrix a_{ijl} is built from the beam transport function of the accelerating structure.

Knowing all the projections p_{ij}, the object of reconstruction g_l can be obtained from an iterative procedure over the projections, starting from an initial guess $g^{(0)}$ [42]:

$$g_q^{(k+1)} = g_q^{(k)} + \sum_{ij} \frac{a_{ijq}(p_{ij} - \sum_l a_{ijl} \cdot g_l^{(k)})}{\sum_{nm} a^2{}_{inm}} \tag{6.2}$$

until some required convergence is achieved. The initial guess can be, for example, a matrix with all zero elements. During the iterations the non-negativeness of each solution $g_q^{(k+1)}$ can be forced by setting all negative values to zero and then reusing them in the next cycle of iterations, since a negative phase space distribution is not physical. However, noise and inconsistencies in the measured projections can lead to stripe artifacts in the solution due to the additive nature of the algorithm [44].

The convergence of the reconstruction algorithm can be verified as the relative root mean square between all the elements from two consequent iteration steps:

$$C(k) = \sqrt{\frac{\sum_q \left(g_q^{(k)} - g_q^{(k-1)}\right)^2}{q_{max}}} \Big/ max(g^{(k)}), \tag{6.3}$$

where q_{max} and $max(g^{(k)})$ are the number of elements and the maximal element in the reconstructed image $g^{(k)}$, respectively, and k is the number of the current iteration. A criterion for the convergence of the algorithm can be defined as $C(k)$ is less than some number, sufficient that the following iterations will not visibly improve the reconstruction results.

An example of the ART algorithm convergence as a function of the number of iteration steps for the measured data (see section 8.3.1) is shown in Fig. 6.3. For the initial guess $g^{(0)}$ an array with zero elements was used. As it can be seen from Fig. 6.3, for this example, already after 60 iterations the convergence $C(k)$ is less than 10^{-3}.

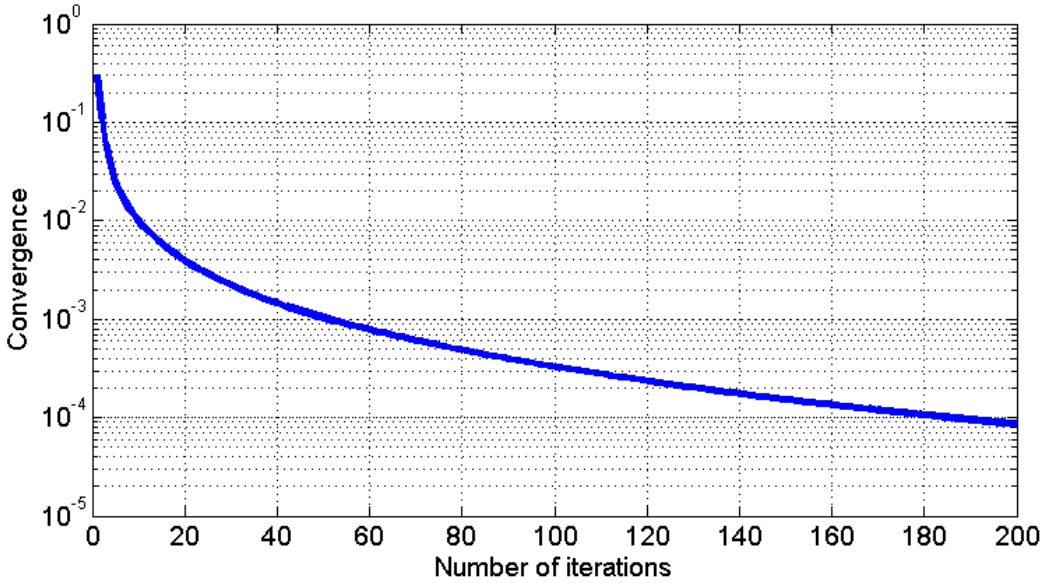

Fig. 6.3: Convergence of the ART algorithm as a function of the number of iteration steps. The vertical axis shows the convergence $C(k)$ according to Eq. (6.3) and the horizontal axis shows the number of iterations.

The corresponding reconstruction results of the measured data are shown in Fig. 6.4 for different numbers of iteration steps. It can be seen that after 10 iteration steps the core part of the object of reconstruction lie on some wide hill with long slopes, Fig. 6.4 (a). 50 iteration steps lead to significant improvement of the reconstruction result as can be seen in Fig. 6.4 (b). After 100 iteration steps the result is slightly improved in terms of reconstruction artifacts compared to the case with 50 iteration steps, Fig. 6.4 (c). Finally, the reconstruction result after 200 iteration steps has almost no difference with the result after 100 iteration steps, Fig. 6.4 (d). Nevertheless, one can clearly see that with increase in the number of iterations also the width of the core distribution gets smaller. Calculated longitudinal RMS emittances for these four reconstructed phase spaces are 157, 67, 56 and 53 mm keV/c, respectively.

To summarize, 100 iteration steps are sufficient as further iterations do not significantly improve the reconstruction. In terms of convergence from Eq. (6.3), $C(k)$ should be less or equal to $3 \cdot 10^{-4}$. However, one needs to keep in mind that the reconstruction still tends to overestimate the longitudinal emittance.

For simplicity in the simulation of measurements and reconstructions of the measured data for longitudinal phase space tomography, shown in this thesis in Chapter 7 and Chapter 8, always 100 iterations are used.

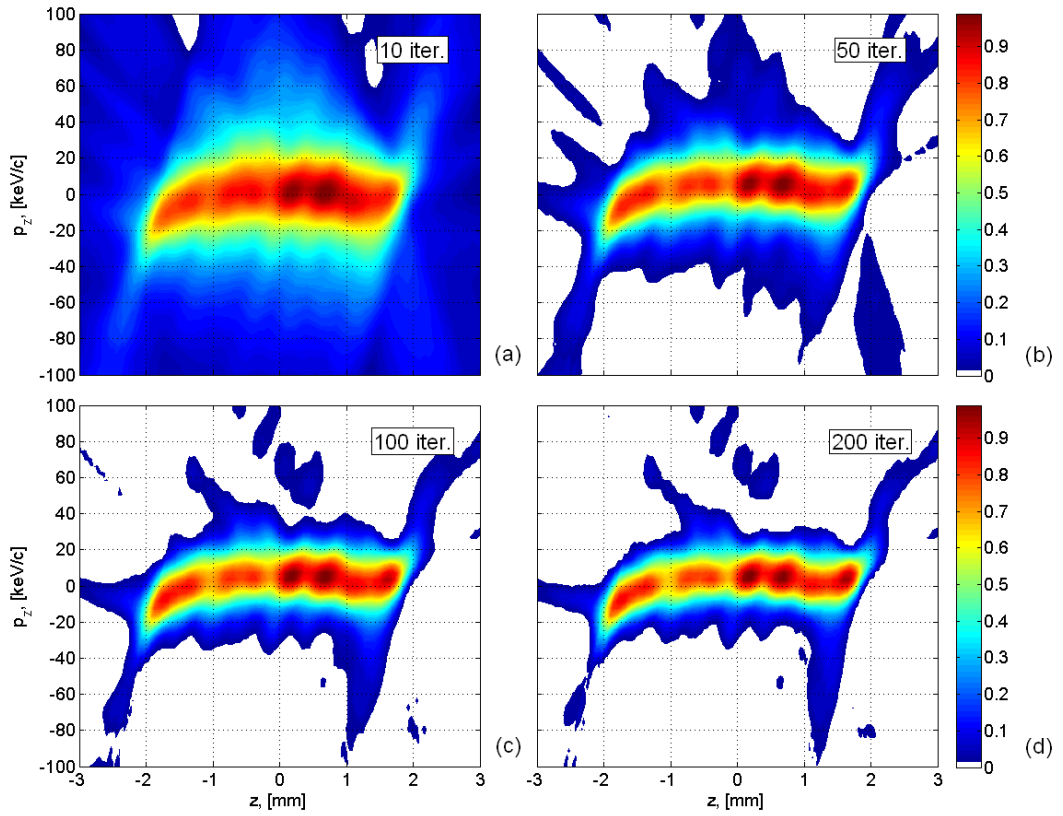

Fig. 6.4: An example of ART reconstruction of the experimental tomography data after 10 (a), 50 (b), 100 (c) and 200 (d) iteration steps.

6.2 Application of ART for longitudinal phase space measurements

To perform a tomographic reconstruction using the ART algorithm defined by Eq. (6.2) one needs to prepare the a_{ijl} matrix which describes the transformation of the bunch longitudinal phase space by the accelerating structure. In other words, one needs to show how the longitudinal coordinates and the longitudinal momenta of the electrons in the bunch are being transformed during the acceleration for different RF phases of the accelerating structure.

For the longitudinal coordinates it is assumed that these coordinates of the particles within the bunch stay constant relative to the center of mass during acceleration:

$$z_1 = z_0, \tag{6.4}$$

where z_0 is the particle longitudinal coordinate within the bunch relative to the center of mass upstream the accelerating structure and z_1 is the corresponding

coordinate downstream the structure. This will be true for ultra-relativistic particles. For example, for the PITZ case, beam momentum upstream the booster cavity is about 6.5 MeV/c. The distance between two particles in the bunch whose longitudinal momentum differs by 20 keV/c becomes bigger only by about 30 μm during propagation through the booster cavity with the length of about 1.6 m (without taking into account acceleration). As a result, for the bunch with 20 keV/c momentum spread and with the length of about 6 mm it will cause the elongation of the bunch up to about 0.5%.

Using particle acceleration model described in section 2.3 the longitudinal momentum of a single particle p_{z_1} after acceleration can be calculated from Eq. (2.42):

$$p_{z_1} = p_{z_0} + V \cdot cos\left(\omega(t - \frac{z_0}{c}) - \varphi_0\right), \tag{6.5}$$

where p_{z_0} is the longitudinal component of momentum at the entrance of the accelerating structure, p_{z_1} at the exit of the accelerating structure, c is the speed of light, V is the momentum gain of the accelerating structure, φ_0 is the RF phase for which the single particle, entering the cavity will obtain the highest possible momentum gain and $t = \varphi/\omega$ is the time when the particle enters the structure (φ is the phase at which particle enters the cavity; if $\varphi = \varphi_0$ a particle in the center of mass will obtain momentum gain V). As a result, the momentum of the particle relative to the mean momentum of the bunch after acceleration is a function of two parameters: RF relative phase $\varphi - \varphi_0$ and particle coordinate z_0 relative to the center of mass:

$$\Delta p_{z_1} = g(\varphi - \varphi_0, z_0) = V \cdot \left[cos\left(\omega\left(t - \frac{z_0}{c}\right) - \varphi_0\right) - cos(\omega t - \varphi_0)\right]. \tag{6.6}$$

Eq. (6.6) describes a transformation of the longitudinal phase space caused by the accelerating structure including changing of the acceleration field along the bunch, therefore the back transformation will give as a result the longitudinal phase space upstream the accelerating structure. Using the approximations from equations (6.4) and (6.6), the matrix a_{ijl} can be obtained and the tomographic reconstruction can be performed according to Eq. (6.2). The longitudinal phase space downstream the accelerating structure can be obtained by applying the acceleration model to the reconstructed phase space upstream.

For the bunch length much shorter than the RF wavelength:

$$z_{0_i} \ll \lambda = 2\pi c/\omega, \tag{6.7}$$

Eq. (6.6) can be simplified ($\omega \frac{z_0}{2c} \ll \pi$):

$$\Delta p_{z_1} = V \cdot 2\, sin\left(\varphi - \varphi_0 - \omega \frac{z_0}{2c}\right)\, sin(\omega \frac{z_0}{2c}) \approx V \cdot \omega \cdot sin(\varphi - \varphi_0) \cdot \frac{z_0}{c}, \tag{6.8}$$

where $\varphi = \omega t$. The momentum chirp k_m in the longitudinal phase space can be calculated from Eq. (6.8) by dividing the right part by z_0:

$$k_m = V \cdot \omega \cdot sin(\varphi - \varphi_0) \cdot \frac{1}{c}. \tag{6.9}$$

6.3 Data taking for tomographic reconstruction

The momentum distributions measured for different booster RF phases which are needed as an input for the tomographic reconstruction are saved for each electron bunch charge and temporal laser profile. According to the previous sections, the experimental data has to be prepared before applying the reconstruction algorithm.

In order to perform the tomographic reconstruction the matrix a_{ijl} has to be created using Eq. (6.4) and Eq. (6.6). First, the size of the reconstructed area in the longitudinal phase space plane has to be defined as follows. The range of the momentum axis is chosen as the maximum span between minimum and maximum momentum for all booster RF phases. The range of the longitudinal coordinate axis can be estimated from the maximal momentum chirp applied to the bunch during measurements and the momentum spread of the bunch when this chirp is applied. This range can be fine adjusted later after the first reconstruction is performed.

An example of a measured momentum distribution for 20 pC bunch charge, generated with a flat-top laser pulse, at HEDA1 section is shown in Fig. 6.5. It consists of the beam signal starting from ~21.0 MeV/c up to ~21.6 MeV/c on top of some background noise.

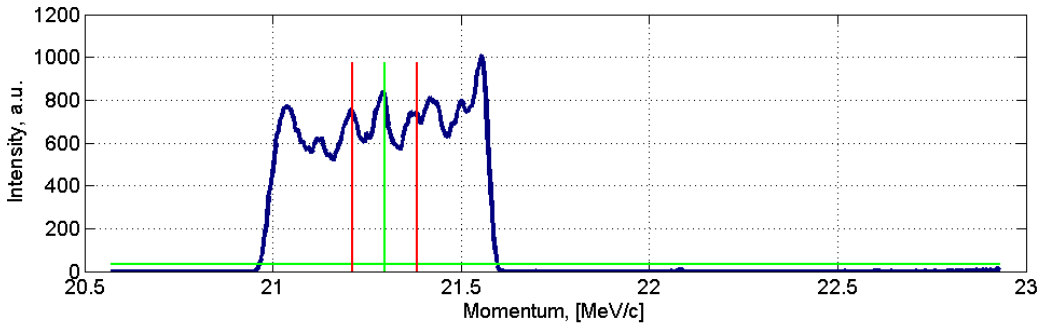

Fig. 6.5: An example of measured electron bunch momentum distribution for 20 pC bunch charge at the HEDA1 section, the blue curve. The vertical green line shows the mean momentum value, the distance between two vertical red lines shows the RMS momentum spread. The horizontal green line shows the level of intensity at which the background noise will be subtracted.

Filtering of the background noise is realized by subtracting a fraction of the mean intensity from the distribution, Fig. 6.5 the horizontal green line. Afterwards all negative values of the distribution are set to zero:

$$p_{ij}^{(1)} = p_{ij}^{(0)} - \frac{v}{k_{max}} \cdot \sum_k p_{ik}^{(0)}, \text{ if } p_{ij}^{(1)} < 0, p_{ij}^{(1)} = 0, \tag{6.10}$$

where v is the defined subtraction coefficient, $p_{ij}^{(0)}$ is an initial momentum distributions, $p_{ij}^{(1)}$ is the resulting filtered momentum distribution, the indexes j and k correspond to the momentum bins in the momentum distributions, k_{max} is the number of momentum bins in the momentum distribution and the index i corresponds to the number of the projection, i.e. the corresponding booster RF phase. After that, all the measured momentum distributions have to be shifted to the mean value so that the mean momenta of the resulting momentum distributions are zero for each projection i (in the reconstruction algorithm matrix a_{ijl} describes transformation of the longitudinal phase space relative to the bunch mean momentum and the bunch center of mass, see section 6.2):

$$\sum_j p_{ij} \cdot m_j = 0. \tag{6.11}$$

where p_{ij} is the weight in the momentum distribution for booster phase i and momentum bin j, m_j is the value of momentum for the momentum bin j. The resulted filtered and centered momentum distribution is shown in Fig. 6.6 with the blue curve.

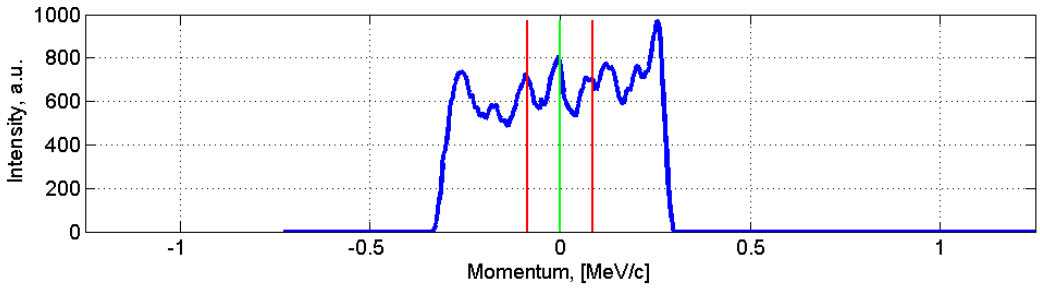

Fig. 6.6: Filtered and centered measured momentum distribution, the blue curve. The vertical green line shows the mean momentum value, the distance between two vertical red lines shows the RMS momentum spread.

Then the measured momentum distributions p_{ij} are scaled so that the sum of all bins in the momentum distribution is the same constant for each booster phase i:

$$\sum_j p_{ij} = Const. \tag{6.12}$$

This results from the fact, that during acceleration with different RF phases of the booster cavity no particles are lost and the integral of the beam image on the screen should be constant. After that, the resulting matrix p_{ij} is ready to be used in the reconstruction algorithm described in section 6.1.

Further analysis can be performed after the longitudinal phase space is reconstructed. The bunch current distribution can be extracted as a horizontal projection from the longitudinal phase space as well as the slice momentum spread and the bunch longitudinal RMS emittance can be obtained.

6.4 Estimation of the temporal resolution

The temporal resolution τ of the reconstructed longitudinal phase space depends on the momentum resolution of the measured momentum spectra σ_0, the maximum momentum chirp k_{max} applied to the electron bunch by the accelerating structure and the slice momentum spread σ_δ of the bunch. It can be estimated at [9]:

$$\tau = \frac{1}{c}\frac{\sigma_\delta + \sigma_0}{k_{max}}. \tag{6.13}$$

In a simple model, when one needs to roughly get the longitudinal profile of the electron bunch, it can be measured by applying the maximal momentum chirp k_{max} by the accelerating structure and measuring the momentum distribution for it. This measured momentum distribution will represent the longitudinal profile of the electron bunch with the scale parameter of k_{max}.

An example of a simulated longitudinal phase space for 1 nC bunch charge, generated with a flat-top laser pulse with 17.5 ps FWHM duration and 2 ps rise and fall times, for RF phase of the accelerating structure of 22 degrees offset with respect to the MMMG phase is shown in Fig. 6.7. The momentum chirp calculated from Eq. (6.9) with $V = 15.7\,\mathrm{MeV/c}$ and $\omega = 8.2 \cdot 10^9 s^{-1}$ is 160 keV/c/mm. Assuming that the momentum distribution is measured with resolution of 4 keV/c and the RMS slice momentum spread for the bunch, presented in Fig. 6.7, is 4 keV/c, the temporal resolution of the reconstructed longitudinal phase space according Eq. (6.13) will be 50 μm or about 0.2 ps. This is comparable with the temporal resolution estimated for the longitudinal phase space measurements using TDS cavity, see sections 4.2 and 5.3.

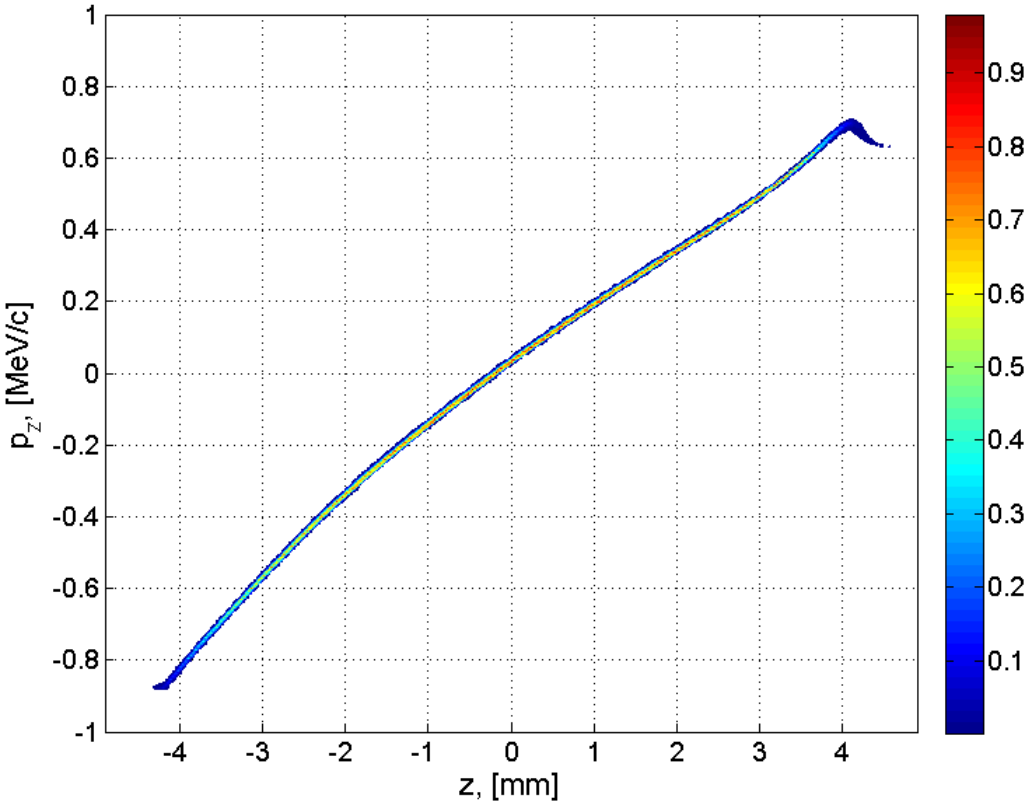

Fig. 6.7: Simulated longitudinal phase space of the bunch downstream the accelerating cavity, 1 nC bunch charge generated with a flat-top laser pulse with 17.5 ps FWHM duration and 2 ps rise and fall times, for an offset of 22 degrees of the RF phase of the accelerating structure with respect to the MMMG phase. The vertical axis is shown relative to the bunch mean momentum of 22.4 MeV/c.

Chapter 7

Simulations of measurements with tomographic technique

The tomographic technique for longitudinal phase space measurements can be verified with numerical simulations. Simulations presented in this chapter were performed for Gaussian and flat-top temporal laser profiles, Fig. 7.1, and for several electron bunch charges using the ASTRA particle tracking code [38].

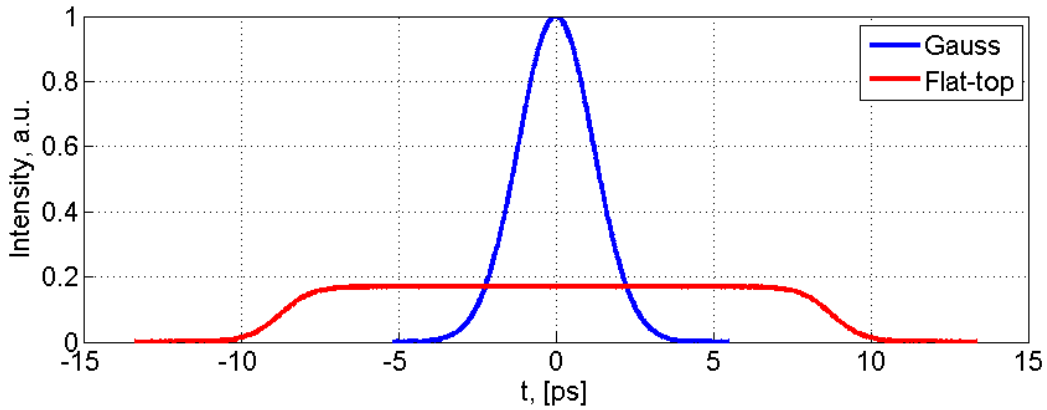

Fig. 7.1: Temporal laser profiles used for simulations: a Gaussian profile with duration of 2.8 ps FWHM – the blue curve and a flat-top profile with duration of 17.5 ps – the red curve. The flat-top profile in this plot was normalized to have the same integral laser pulse energy as the Gaussian profile.

A Gaussian temporal profile with duration of 2.8 ps FWHM was used for simulations as the shortest available temporal laser profile at PITZ. A flat-top temporal profile with duration of 17.5 ps FWHM and 2 ps rise and fall times was used as the longest available flat-top laser profile at PITZ in the beginning of 2013. The transverse laser distribution had a uniform round profile with a diameter of 1.6 mm, which corresponds to an RMS transverse size of 0.4 mm.

The common machine parameters used for the simulations presented in this chapter are shown in Table 7.1. Transverse laser size was chosen as one used in an experiment. The main solenoid current was chosen as the current which delivers a good beam transport in the experiment, see section 8.1.

Table 7.1: Machine parameters used for the ASTRA simulations.

Transverse laser size, RMS	0.4 mm
Main solenoid current	377 A
Maximum mean beam momentum after the gun	6.68 MeV/c
Maximum mean beam momentum after the booster	22.4 MeV/c

The simulations for the Gaussian temporal laser profile were done for electron bunch charges of 700 pC and 20 pC. The simulations for the case of the flat-top temporal laser profile were done for 1 nC and 20 pC bunch charges.

The charge of 1 nC was chosen as a bunch charge mostly studied at PITZ and will be used as a nominal charge for European XFEL operation [5]. The charge of 20 pC was chosen as charge mostly used for short bunches generation and single spike lasing [45], [46]. And the charge of 700 pC for the Gaussian temporal laser profile was chosen as the maximum extractable one in a real experiment at PITZ for such temporal and transverse laser profiles at that moment.

7.1 Gaussian temporal laser profile and 20 pC bunch charge

The simulations for 20 pC bunch charge presented in this section were done for a Gaussian temporal laser profile with a duration of 2.8 ps FWHM, Fig. 7.1 the blue curve.

The electron bunch mean momentum was simulated downstream the CDS booster at the position of the HEDA1 reference screen High1.Scr5, Fig. 3.5. The simulations were done for the booster RF phases in the range from -20 degrees to +20 degrees with respect to the MMMG phase with a step width of 1 degree, 41 momentum projections in total. A maximum mean momentum of 22.4 MeV/c was achieved. The result of the phase scan of the electron bunch mean momentum is shown in Fig. 7.2 with the blue curve (a) and the beam RMS momentum spread is shown with the red curve (b). The green curve in the Fig. 7.2 (a) is mostly covering the blue one and shows the beam momentum as a function of the booster RF phase according to the acceleration model described by Eq. (2.42):

$$p = p_g + \left(p_b - p_g\right) \cdot cos(\varphi - \varphi_0), \tag{7.1}$$

where p is the electron bunch mean momentum downstream the booster cavity, $p_g = 6.68$ MeV/c is the electron bunch mean momentum downstream the gun, $p_b = 22.4$ MeV/c is the maximum mean momentum downstream the booster and $\varphi_0 = 0$ corresponds to the MMMG phase. The model gives a result consistent with the numerical simulation, the green and blue curves mostly coincide, Fig. 7.2 (a).

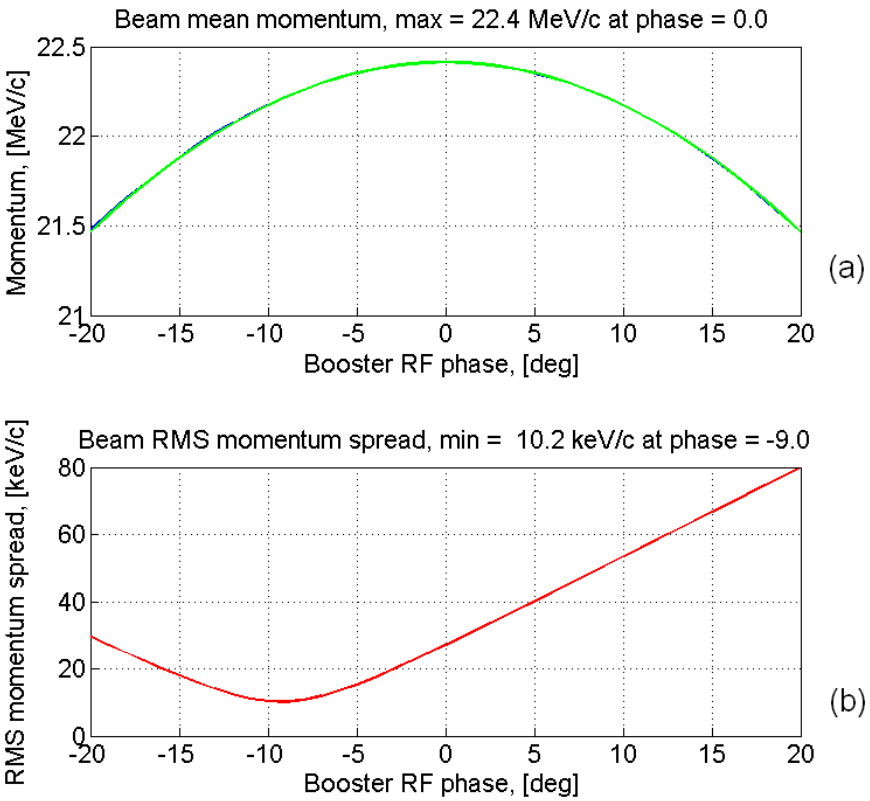

Fig. 7.2: Simulated mean beam momentum (a), blue curve, and RMS momentum spread (b), red curve, as a function of the booster RF phase for 20 pC bunch charge generated with the Gaussian temporal laser profile. The green curve in (a) is the beam momentum according to the acceleration model described by Eq. (2.42).

From the simulated momenta of the particles for each booster RF phase the momentum distributions were calculated with a bin size of 1 keV/c, close to the minimum momentum bin size available in the measurements, see Chapter 8. The resulting momentum distributions are scaled and normalized according to the procedure introduced in section 6.3. Final data, ready for tomographic reconstruction, are shown in Fig. 7.3 as momentum distributions for different booster RF phases. It is shown with 2 degree step of the booster RF phase to do not overload this plot.

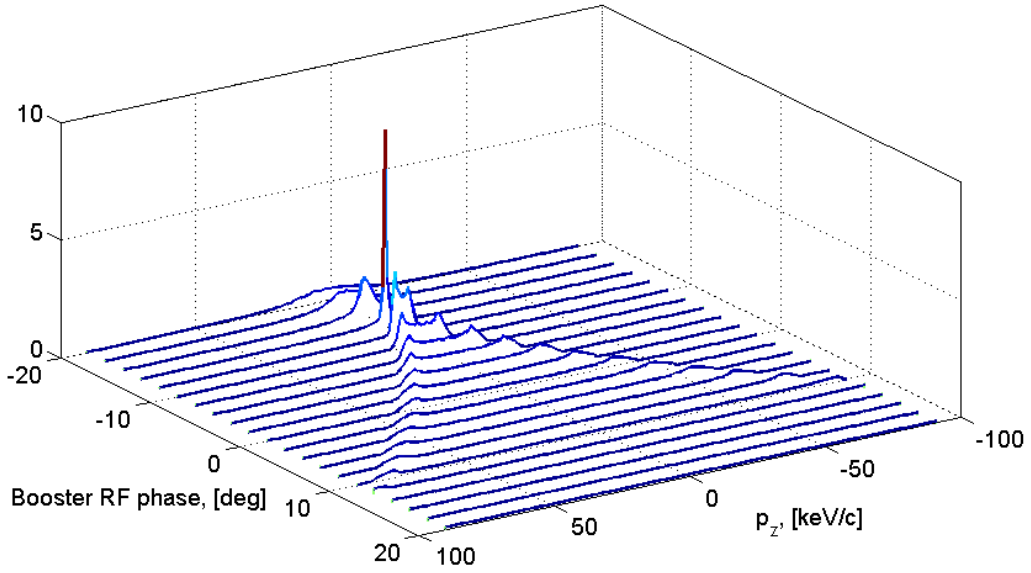

Fig. 7.3: Simulated momentum distribution for different booster RF phases, for 20 pC bunch.

Then the data are treated by the iterative reconstructed algorithm ART, as described in section 6.1 using all 41 momentum projections. The result of the reconstruction after 100 iterations starting from a zero initial guess is shown in Fig. 7.4 upper plot (a) and the original longitudinal phase space (calculated from the simulated particles distribution) upstream the booster cavity is shown on the bottom plot (b). For this reconstruction, the electron bunch momentum distributions had 194 bins with a bin size of 1 keV/c and 201 bins were used for the longitudinal coordinate (bin size of 0.01 mm). The corresponding convergence is shown in Fig. 7.5 as a function of the iteration number. The method converges quite fast and reached convergence criteria of $C(k) \leq 3 \cdot 10^{-4}$ after 100 iterations.

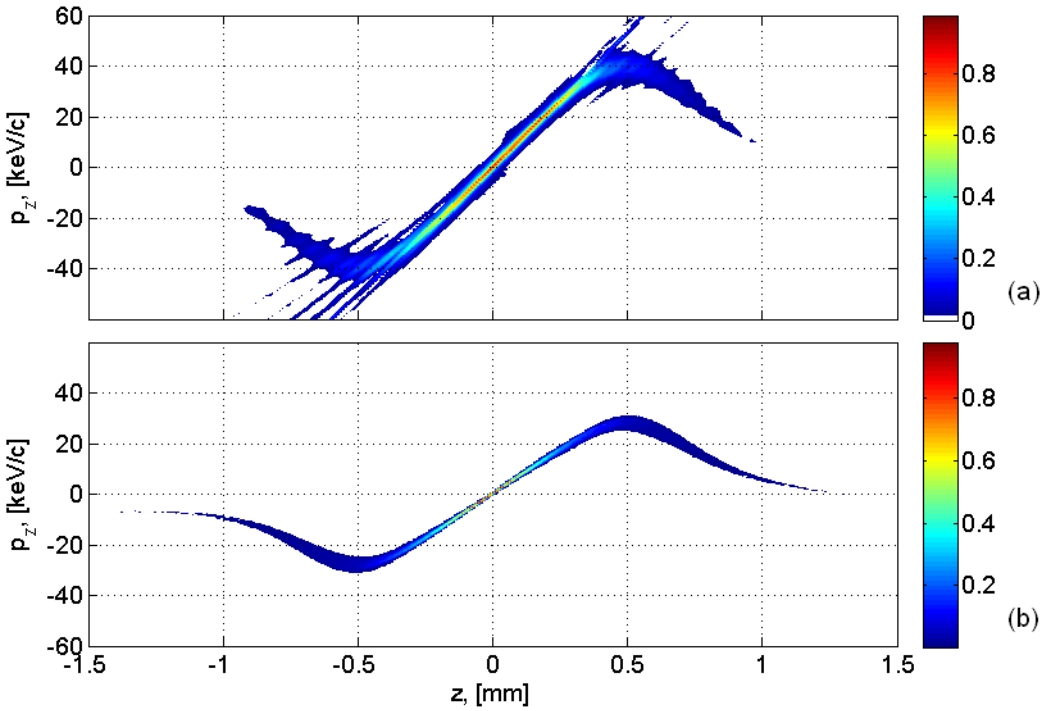

Fig. 7.4: Reconstructed longitudinal phase space upstream the booster cavity (a) from a simulated momentum distributions at 8.92 m and original longitudinal phase space from ASTRA at 2.5 m (b), for the 20 pC bunch charge generated with the Gaussian temporal laser profile.

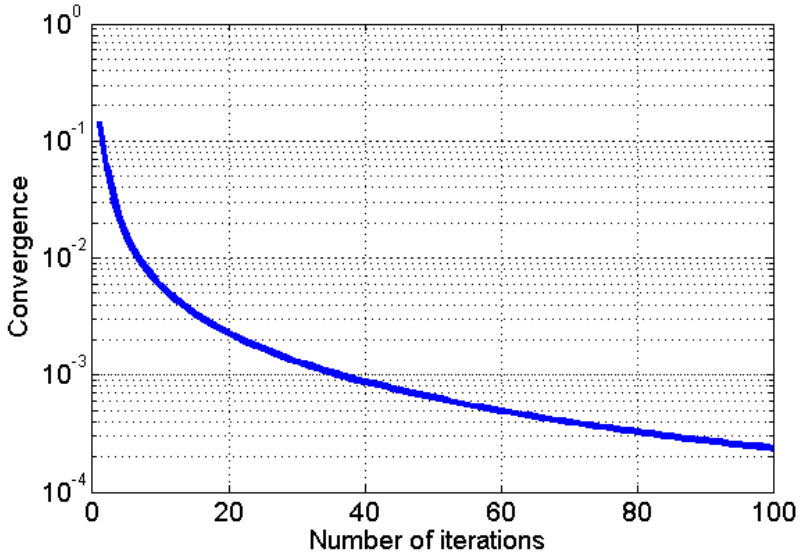

Fig. 7.5: Convergence of the ART algorithm for 100 iterations for the reconstructed phase space shown in Fig. 7.4 (a).

The reconstructed longitudinal phase space looks close to the original simulated one, see Fig. 7.4 (a) and (b), but the slope of the reconstructed one is higher and as a result the reconstructed one has a bigger momentum spread. Also the reconstructed phase space has some reconstruction artifacts which arise from the additive nature of the ART algorithm.

The higher slope in the reconstructed longitudinal phase space can be explained by significant space charge forces for such short bunch which are sufficient to additionally accelerate and decelerate the head and tail of the bunch, respectively, by about of 10 keV/c. This effect can be seen in the numerical simulation. In Fig. 7.6 the simulated longitudinal phase space at 8.92 m is shown.

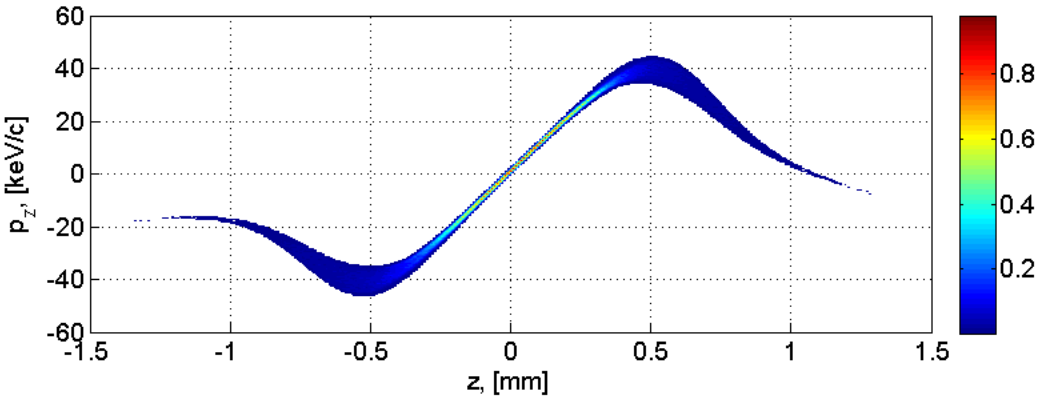

Fig. 7.6: Longitudinal phase space simulated at 8.92 m for the 20 pC bunch charge generated with the Gaussian temporal laser profile.

This phase space looks much closer to the reconstructed one, compared Fig. 7.4 (a) and Fig. 7.6, because the momentum distributions used for the tomographic reconstruction were taken at 8.92 m and already contain the transformation of the longitudinal phase space induced by the space charge forces. The space charge forces are not taken into account in the model used for the tomographic reconstruction, see section 6.2, and this is why the slope in the result of the reconstruction shown in Fig. 7.4 (a) differs from the slope in the original phase space (b).

The resolution of the momentum distribution measurements at the HEDA1 section is limited by the optical system and is about 4 keV/c. For this case a numerical simulation of such measurements can be done using 4 keV/c binning of the momentum distributions. The resulting reconstructed longitudinal phase space is shown in Fig. 7.7. For this reconstruction, the electron bunch momentum distributions had only 66 bins with a bin size of 4 keV/c and 201 bins were used for the longitudinal coordinate (bin size of 0.01 mm), the same as for the previous case.

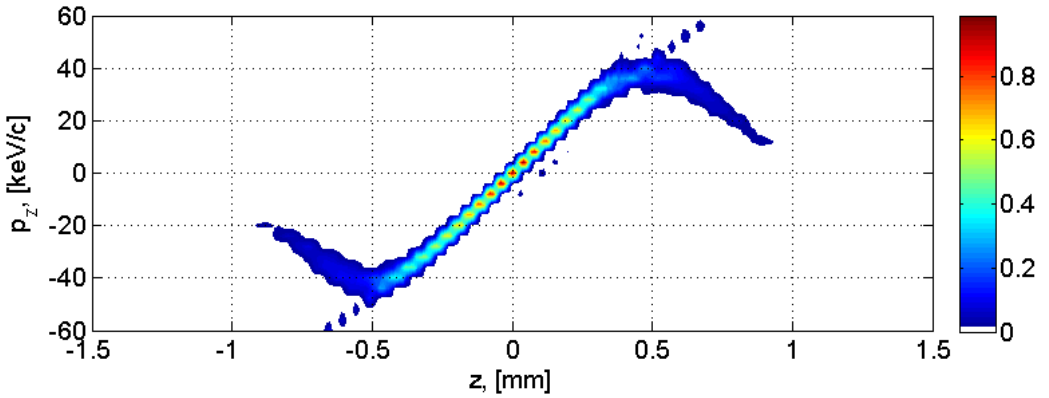

Fig. 7.7: Reconstructed longitudinal phase space upstream the booster cavity using 4 keV/c momentum binning of the used momentum distributions for the tomographic reconstruction.

The reconstructed longitudinal phase space using bigger bin size of 4 keV/c looks close to the one using small bin size of 1 keV/c, compared Fig. 7.4 (a) and Fig. 7.7. Only one major difference is that Fig. 7.7 presents density modulations which are not real and come from the way of plotting the two-dimensional distribution, the period of the modulation is exactly 4 keV/c.

To more completely reproduce the real measurements the procedure of the momentum distribution measurements in the HEDA1 (see section 3.5) can be added to this simulation. This can be realized in the following way. The ASTRA simulations are performed up to reference screen High1.Scr5 located 8.92 m downstream the gun, Fig. 3.5. The last quadrupole upstream the dipole has to be optimized to have the beam focused vertically at this screen. Then the particles distributions at the position of the dipole entrance are taken and using the dipole transport matrix according to Eq. (2.34) can be tracked up to the observation screen Disp2.Scr1. The resulting beam momentum distribution can be obtained as the vertical beam profile at the screen divided by the dispersion.

The resulting reconstructed longitudinal phase space including dipole effect in the simulations of measurements is shown in Fig. 7.8. The same as for the previous case the electron bunch momentum distributions had 66 bins with a bin size of 4 keV/c and 201 bins were used for the longitudinal coordinate. The phase space looks a bit worse than the one reconstructed without taken into account procedure of the momentum measurements, Fig. 7.7, but still the shape and structure are close to the original one, Fig. 7.4 (b).

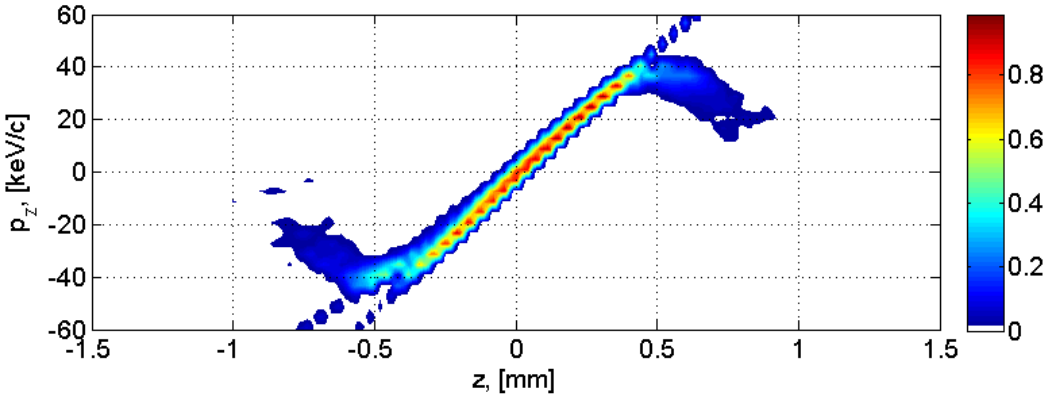

Fig. 7.8: Reconstructed longitudinal phase space upstream the booster cavity using 4 keV/c momentum binning of the simulated measured momentum distributions.

For quantitative comparison of the phase spaces one can compare the calculated longitudinal RMS emittance from each phase space. Difficulties will arise from the reconstruction artifacts which will spoil the calculated longitudinal emittance. To solve this problem, the charge cut can be applied to each phase space to remove reconstruction artifacts and comparison of the resulted purified phase spaces can be performed.

Result of the longitudinal emittance calculation for different level of the charge cut applied is shown in Fig. 7.9 for all four cases. The black curve shows the emittance calculated from the simulated longitudinal phase space shown in Fig. 7.6, the goal emittance. The green curve shows the emittance calculated from the reconstructed phase space shown in Fig. 7.4 (a). The blue and the red curves show the calculated emittances from the reconstructed phase spaces shown in Fig. 7.7 and Fig. 7.8 respectively.

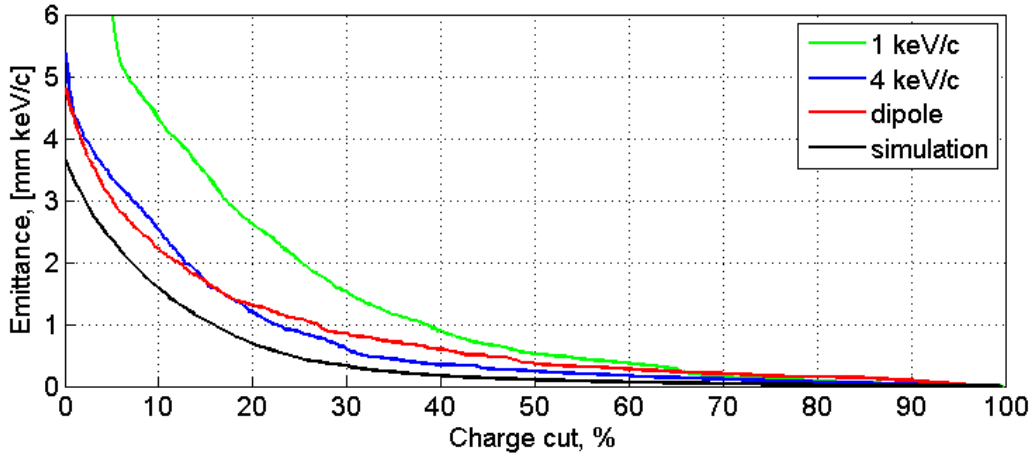

Fig. 7.9: Longitudinal emittance calculation with different charge cut applied.

Strong reconstruction artifacts which are presented in the phase space shown in Fig. 7.4 (a) result in about three times higher calculated emittance from the reconstruction with comparison to the calculated one from the simulated phase space. Charge cut applied does not help to remove reconstruction artifacts in this case. Longitudinal emittances calculated from the phase spaces shown in Fig. 7.7 and Fig. 7.8, which have significantly less artifacts, are much closer to the expected value from simulation: they are about 50% higher.

7.2 Gaussian temporal laser profile and 700 pC bunch charge

The simulations for 700 pC bunch charge presented here were done for a Gaussian temporal laser profile, the same as for the previous case, Fig. 7.1 the blue curve.

Simulations were performed for booster RF phases in range from -18 degrees up to +22 degrees with respect to the MMMG phase with a step of 1 degree, 41 momentum projections in total. The maximum beam momentum is 22.4 MeV/c. The bunch mean momentum downstream the booster cavity as a function of the booster RF phase at the HEDA1 section is shown in Fig. 7.10 (a) with the blue curve and the beam RMS momentum spread is shown with the red curve in Fig. 7.10 (b). The green curve in Fig. 7.10 (a) is mostly covering the blue one and shows the beam momentum as a function of the booster RF phase according to Eq. (7.1) where $p_g = 6.68$ MeV/c is the electron bunch mean momentum downstream the gun, $p_b = 22.4$ MeV/c is the maximum mean momentum downstream the booster and $\varphi_0 = 0$ corresponds to the MMMG phase. The acceleration model gives result very close to the numerical simulation, the green and blue curves are almost identical, Fig. 7.10 (a).

The resulting simulated bunch momentum distributions are scaled and normalized according the procedure introduced in section 6.3. Final data, ready for tomographic reconstruction, are shown in Fig. 7.11 as momentum distributions for different booster RF phases. It is shown with 2 degree step of the booster RF phase to do not overload this plot.

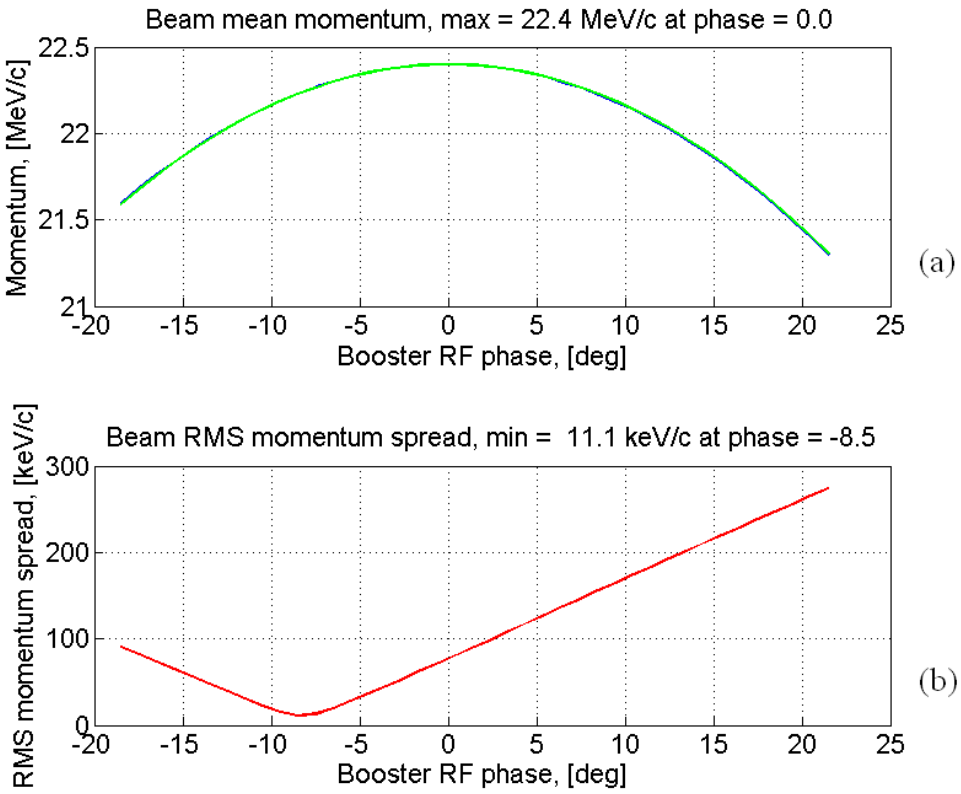

Fig. 7.10: Simulated mean beam momentum (a), blue curve, and beam RMS momentum spread (b), red curve, as a function of the booster RF phase for the 700 pC bunch charge. The green curve in (a) is the beam momentum according to the acceleration model described by Eq. (2.42).

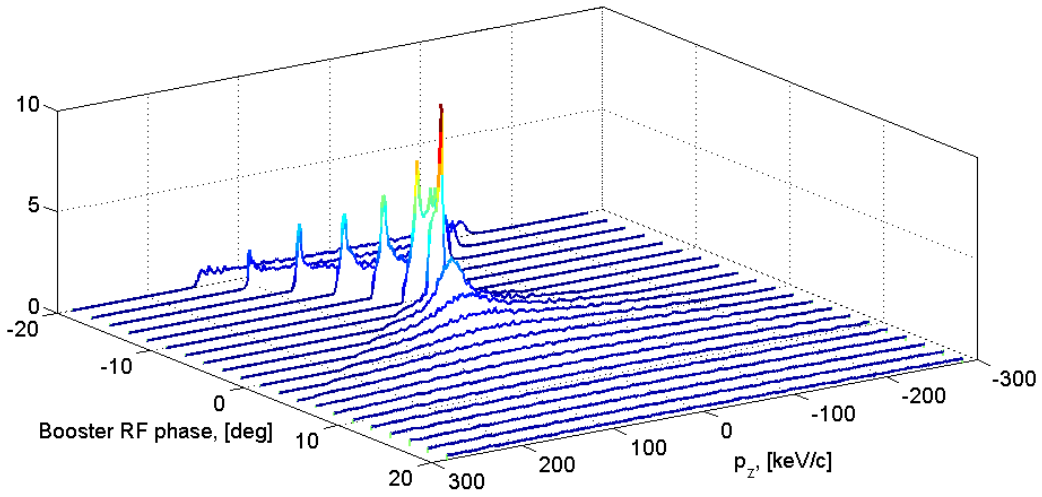

Fig. 7.11: Simulated momentum distribution for different booster RF phases, for 700 pC bunch.

Then the data are treated by the iterative reconstruction algorithm ART using all 41 momentum projections. The result of the reconstruction after 100 iterations starting from a zero initial guess is shown in Fig. 7.12 (a) and the original longitudinal phase space from ASTRA simulation at 2.5 m is shown in Fig. 7.12 (b).

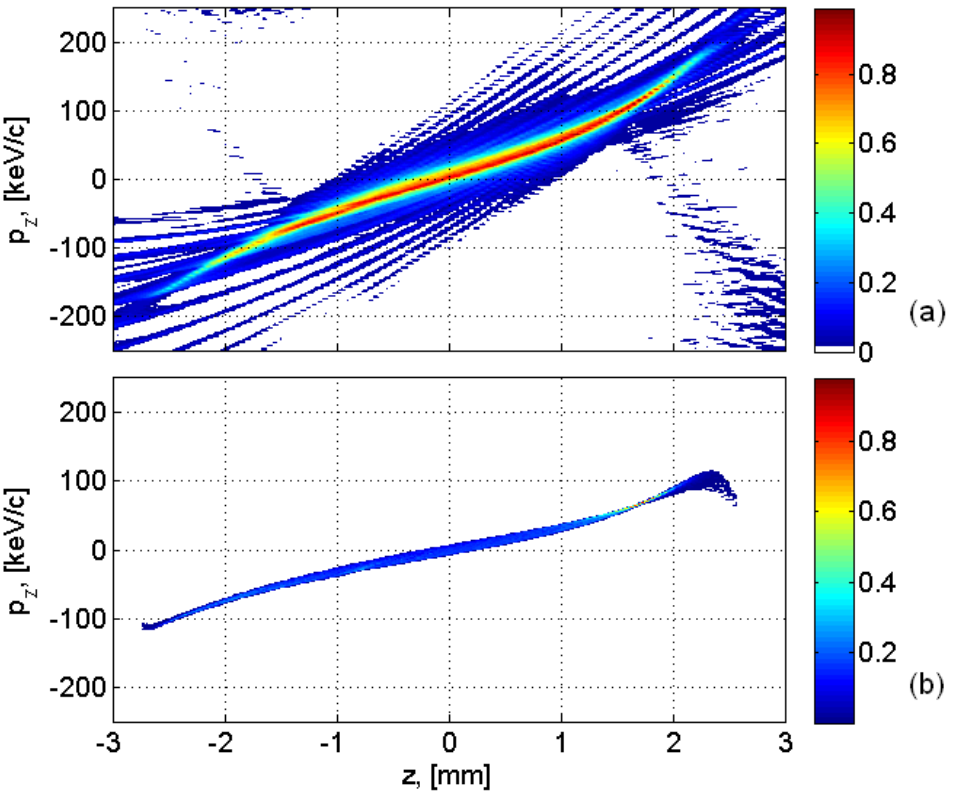

Fig. 7.12: Reconstructed longitudinal phase space upstream the booster cavity from the simulated momentum distributions at 8.92 m downstream the gun by the ART algorithm (a) and the original longitudinal phase space from ASTRA at 2.5 m (b), for 700 pC bunch charge generated with the Gaussian temporal laser profile.

For this reconstruction, the electron bunch momentum distributions had 568 bins with bin size of 1 keV/c and 121 bins were used for the longitudinal coordinate (bin size of 0.05 mm). The iteration method converges quite fast and reached convergence criteria of $C(k) \leq 3 \cdot 10^{-4}$ after 100 iterations. The reconstructed longitudinal phase space looks similar to the original one, see Fig. 7.12 (a) and (b), except the low intensity artifacts arising from the additive nature of the ART algorithm and insufficient number of projections, i.e. too rough step for the booster RF phase. Using more momentum projections the quality of the reconstruction can be improved. The head and the tail of the reconstructed phase

space are higher and lower than it is for the simulated one, respectively. This effect can be explained by the space charge forces which accelerate a bit the head of the bunch and decelerate the tail.

7.3 Flat-top temporal laser profile and 20 pC bunch charge

The simulations for 20 pC bunch charge presented in this section were done for a flat-top temporal laser profile with duration of 17.5 ps FWHM and 2 ps rise and fall times, Fig. 7.1 the red curve.

The simulated electron bunch mean momentum as a function of the booster RF phase at the HEDA1 section is shown in Fig. 7.13 (a) with the blue curve and beam RMS momentum spread is shown in Fig. 7.13 (b) with the red curve. The simulations were done for the booster RF phases in the range from -20 degrees to +20 degrees with respect to the MMMG phase with a step width of 1 degree, 41 momentum projections in total. The green curve in Fig. 7.13 (a) shows the beam momentum as a function of the booster RF phase according Eq. (7.1) where $p_g = 6.68$ MeV/c is the electron bunch mean momentum downstream the gun, $p_b = 22.4$ MeV/c is the maximum mean momentum downstream the booster and $\varphi_0 = 0$ corresponds to the MMMG phase. The acceleration model coincides with the numerical simulation very well.

The resulting simulated bunch momentum distributions for each booster RF phases are scaled and normalized according the procedure introduced in section 6.3. Final data, ready for tomographic reconstruction, are shown in Fig. 7.14 as momentum distributions for different booster RF phases. It is shown with 2 degree step of the booster RF phase to do not overload this plot.

To get the longitudinal phase space upstream the booster cavity all 41 momentum projections are treated by the iterative reconstruction algorithm ART. Result of the reconstruction after 100 iterations starting from a zero initial is shown in Fig. 7.15 upper plot (a) and original longitudinal phase space from ASTRA simulation at 2.5 m is shown on bottom plot (b). For this reconstruction, each electron bunch momentum distribution had 414 bins with a bin size of 1 keV/c, and 121 bins were used for the longitudinal coordinate with a bin size of 0.05 mm. The core part of the reconstructed longitudinal phase space looks similar to the original simulated one, except significant amount of the additional artifacts. Vertical wider reconstructed longitudinal phase space, Fig. 7.15 (a), come from insufficient binning of the momentum axis with the bin size of 1 keV/c.

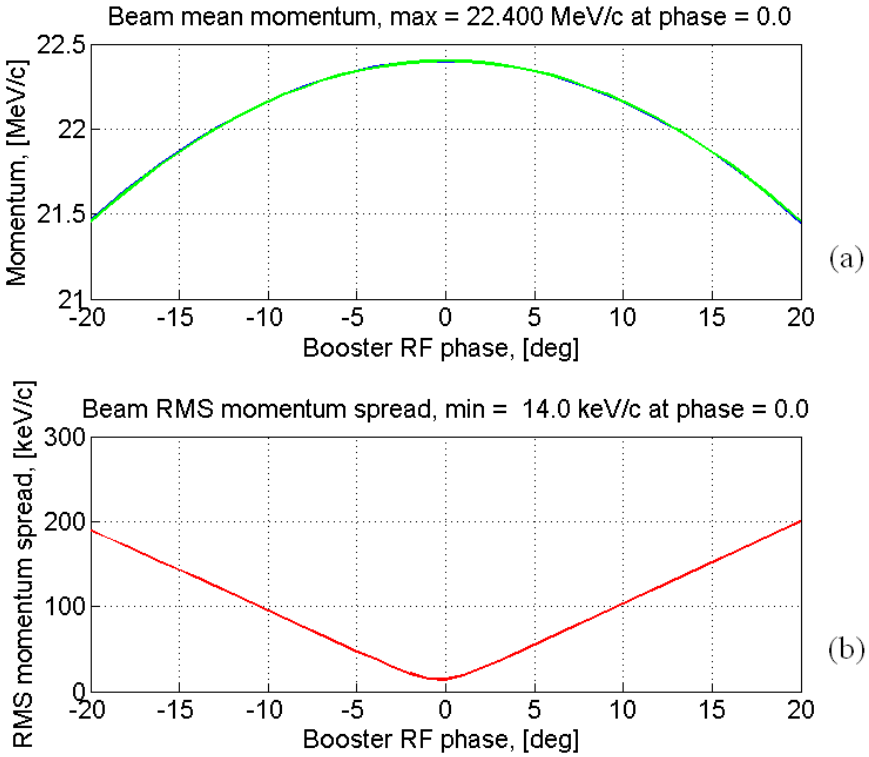

Fig. 7.13: Simulated mean beam momentum (a), blue curve, and beam RMS momentum spread (b), red curve, as a function of the booster RF phase for the flat-top temporal laser profile and 20 pC bunch charge. The green curve (a) is the beam momentum according to the acceleration model described by Eq. (2.42).

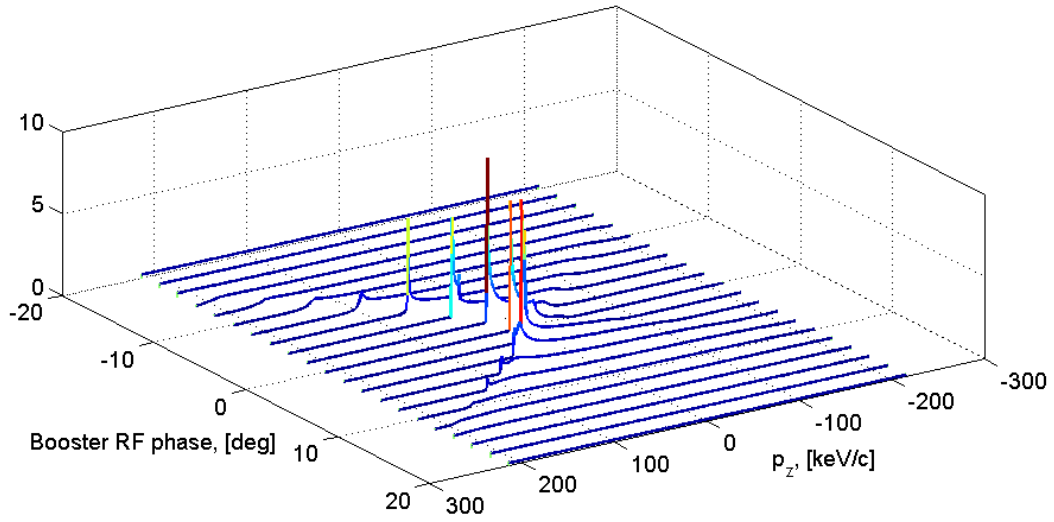

Fig. 7.14: Simulated momentum distribution for different booster RF phases, for 20 pC bunch.

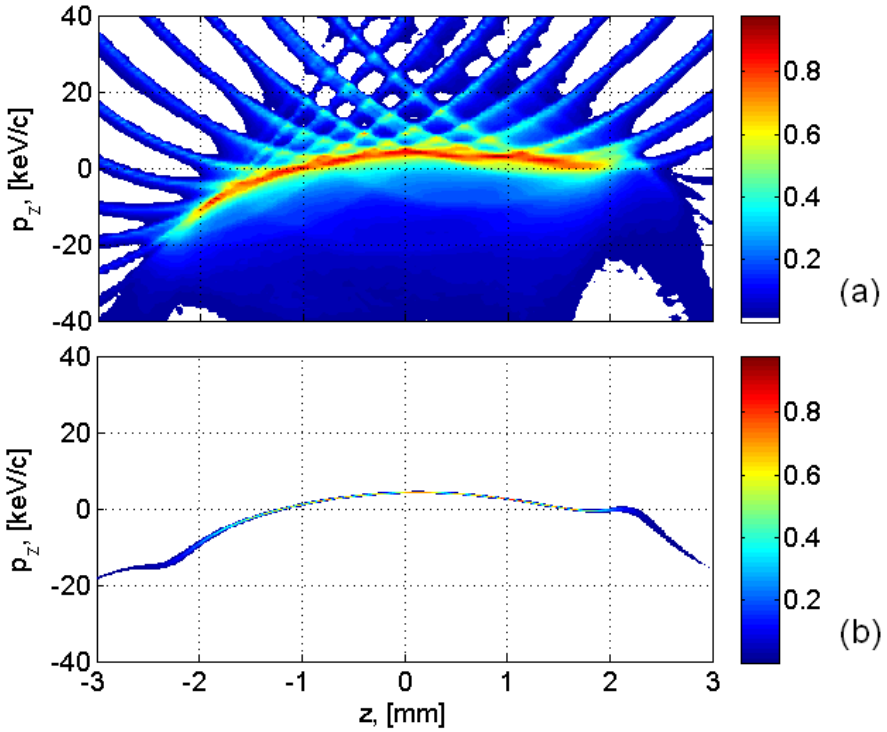

Fig. 7.15: Reconstructed longitudinal phase space upstream the booster cavity (a) from a simulated momentum distributions at 8.9 m and original longitudinal phase space from ASTRA at 2.5 m (b), for 20 pC bunch charge generated with the flat-top temporal laser profile. The electron bunch momentum distributions have a bin size of 1 keV/c and booster phase step was 1 degree in the range from -20 to +20 degrees.

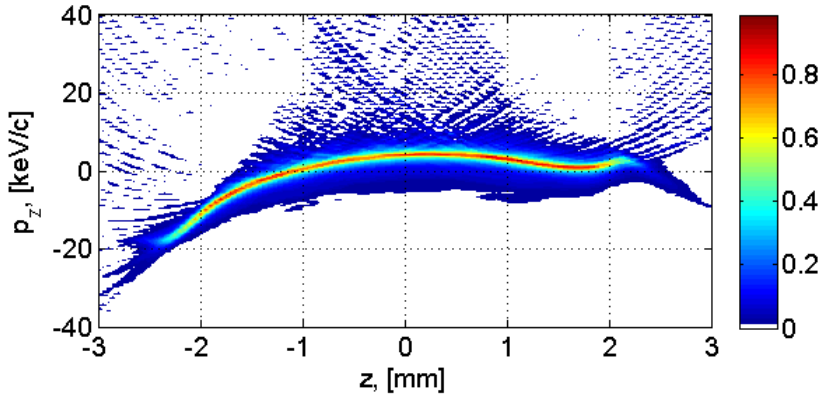

Fig. 7.16: Reconstructed longitudinal phase space upstream the booster cavity (a) from a simulated momentum distributions at 8.9 m. The electron bunch momentum distributions have a bin size of 0.5 keV/c and booster phase step was 0.2 degree in the range from -10 to +10 degrees.

Also, the strong stripe artifacts arise from insufficient number of projections, used booster RF phases, i.e. too rough step in the booster phase. The result of the reconstruction using 0.5 keV/c momentum binning and 0.2 degree RF phase step is shown in Fig. 7.16. The used booster RF phase range was decreased to from -10 to +10 degrees to have reasonable computation time for this simulation, giving in total 101 momentum projections. The reconstructed longitudinal phase space, shown in Fig. 7.16, looks very close to the original one, Fig. 7.15 (b). The reconstructed one is slightly wider vertically and has some small amount of artifacts. Smaller size of momentum binning and finer step in the booster RF phase will further improve the reconstruction.

Applying the acceleration model to the reconstructed longitudinal phase space shown in Fig. 7.16, the bunch longitudinal phase space downstream the CDS booster cavity can be reconstructed. A result is shown in Fig. 7.17 (a) and original longitudinal phase space from the ASTRA simulation at 8.92 m is shown in Fig. 7.17 (b).

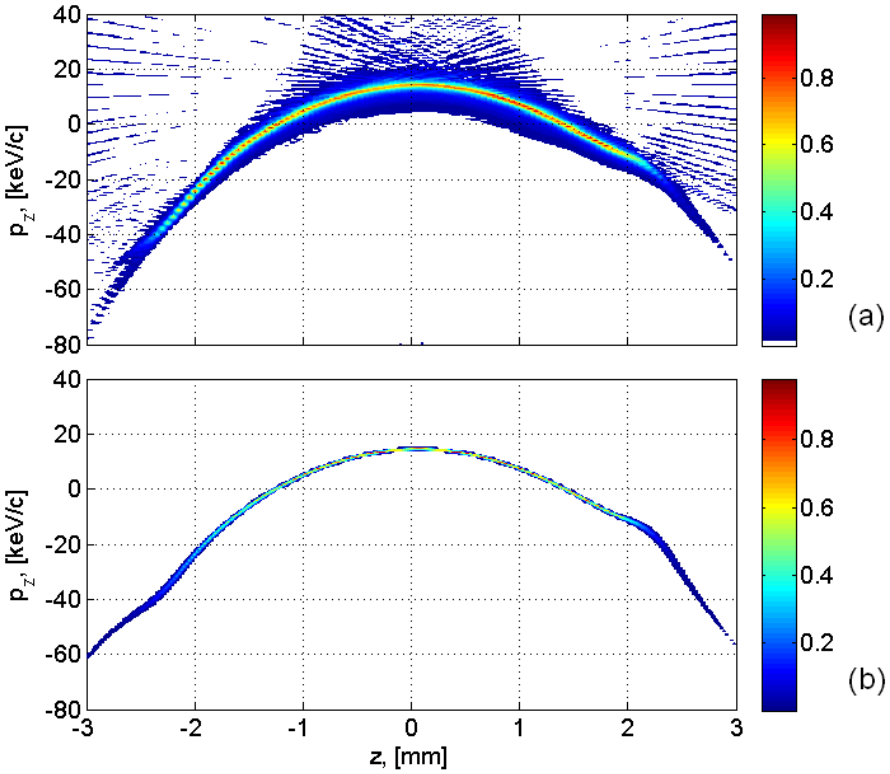

Fig. 7.17: Reconstructed longitudinal phase space downstream the booster cavity (a) from the simulated momentum distributions at 8.92 m and original longitudinal phase space from ASTRA at 8.92 m (b). The electron bunch momentum distributions had a bin size of 0.5 keV/c and booster RF phase step was 0.2 degree in the range from -10 to +10 degrees, i.e. 101 projections.

The reconstructed longitudinal phase space, shown in Fig. 7.17 (a), looks very close to the original simulated one, Fig. 7.17 (b). The reconstructed one is slightly wider vertically and has some small amount of artifacts. Smaller size of momentum binning and finer step in the booster RF phase will further improve the reconstruction. The intensity modulation in the head and the tail of the reconstructed bunch is coming from the plotting for such binning of the longitudinal axis, which was done with a bin size of 0.05 mm. The period of modulations is exactly 0.05 mm.

7.4 Flat-top temporal laser profile and 1 nC bunch charge

The simulations for 1 nC electron bunch charge presented in this section were also done for the same flat-top temporal laser profile, see Fig. 7.1. An evaluation of the simulated longitudinal phase space for the booster MMMG phase at three different locations along the beamline is shown in Fig. 7.18. The first one, Fig. 7.18 (a), is the longitudinal phase space upstream the booster at 2.5 m downstream the gun. The second one, Fig. 7.18 (b), is the longitudinal phase space downstream the booster at the position of the HEDA1 reference screen High1.Scr5 located at 8.92 m downstream the gun. The last one, Fig. 7.18 (c), is the longitudinal phase space downstream the booster at the position of the HEDA2 observation screen Disp3.Scr1 located at about 18.6 m downstream the gun.

The electron bunch mean momentum as a function of the booster RF phase at the HEDA1 section is shown in Fig. 7.19 (a) with the blue curve and the beam RMS momentum spread is shown in Fig. 7.19 (b) with the red curve. The green curve in Fig. 7.19 (a) shows the beam momentum as a function of the booster RF phase according to the acceleration model described by Eq. (7.1) where $p_g = 6.68$ MeV/c is the electron bunch mean momentum downstream the gun, $p_b = 22.379$ MeV/c is the maximum mean momentum downstream the booster and $\varphi_0 = 0$ corresponds to the MMMG phase. The acceleration model coincides with the numerical simulation very well.

The resulting simulated momentum distributions for each booster RF phase are scaled and normalized according to the procedure introduced in section 6.3. Final data, ready for tomographic reconstruction, are shown in Fig. 7.20 as momentum distributions for different booster RF phases. It is shown with 2 degree step of the booster RF phase to do not overload this plot.

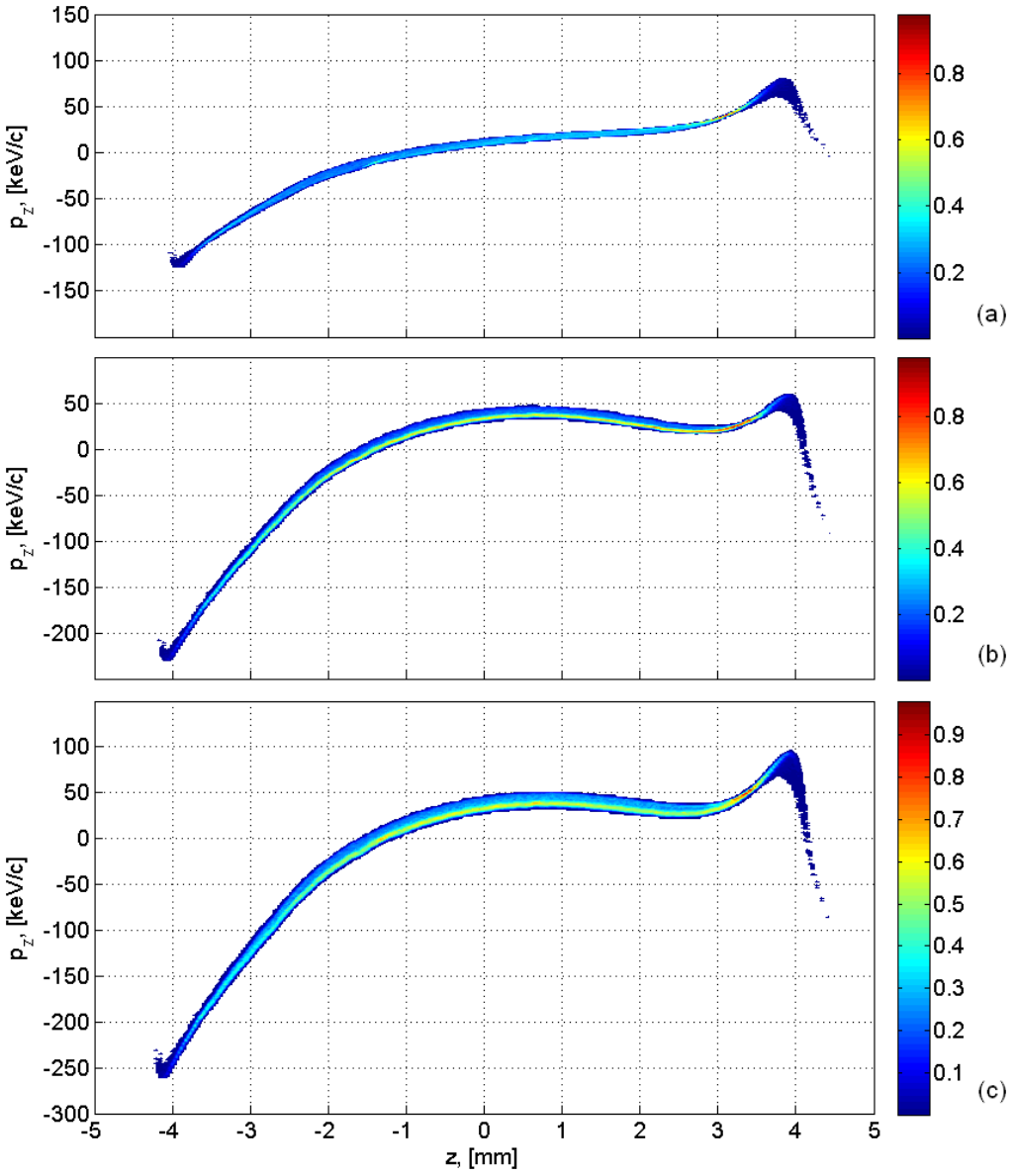

Fig. 7.18: Simulated electron bunch longitudinal phase spaces at 2.5 m (a), at 8.9 m (b) and at 18.6 m (c) downstream the gun for a flat-top temporal laser profile and 1 nC electron bunch charge. The gun and the booster RF phases correspond to MMMG phase.

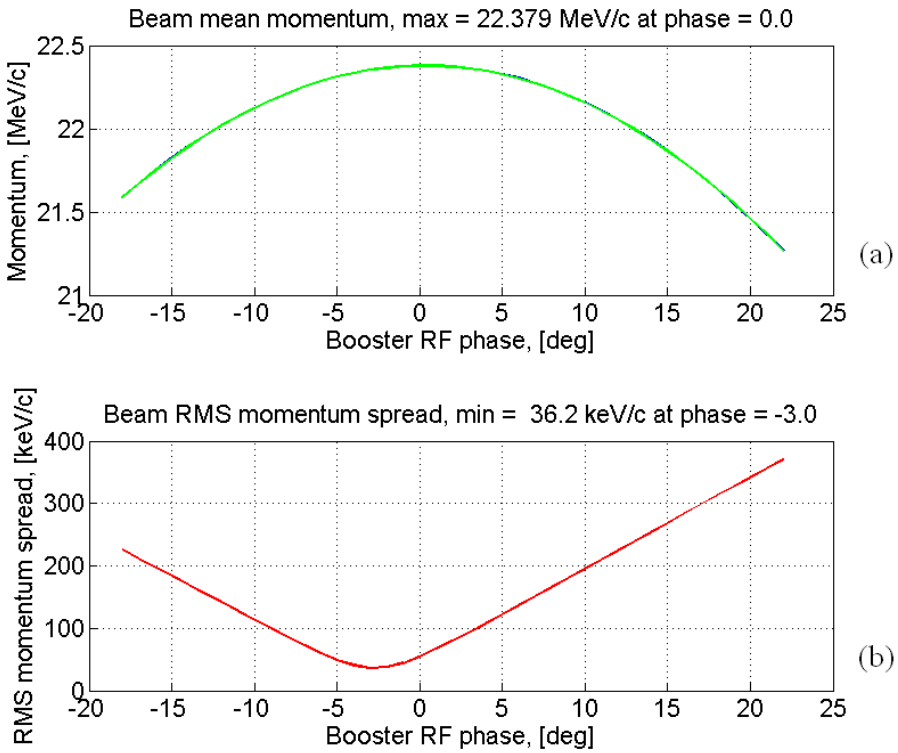

Fig. 7.19: Simulated mean beam momentum (a), blue curve, and beam RMS momentum spread (b), red curve, as a function of the booster RF phase for the flat-top temporal laser profile and 1 nC bunch charge. The green curve (a) is the beam momentum according to the acceleration model described by Eq. (2.42).

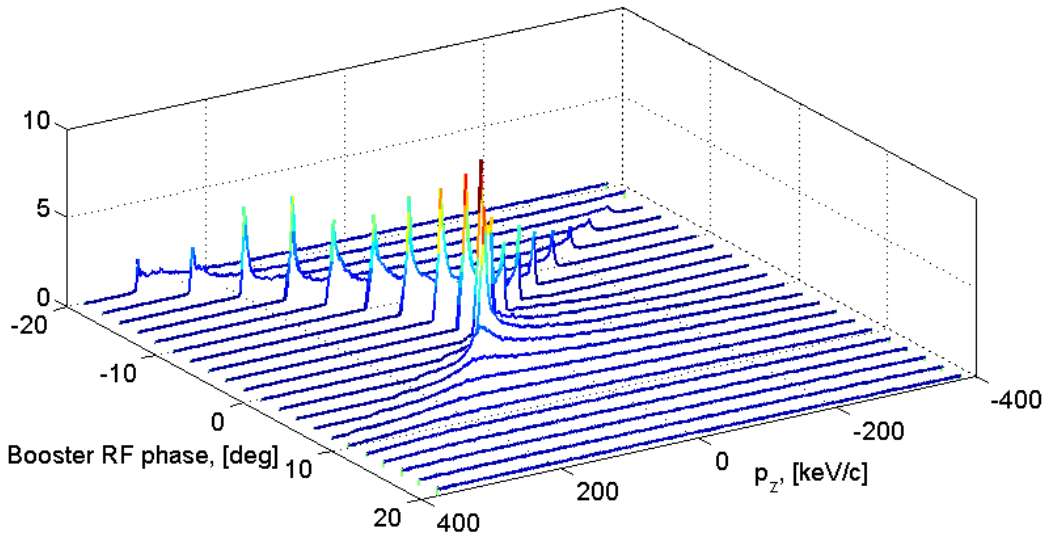

Fig. 7.20: Simulated momentum distribution for different booster RF phases.

Then the data are treated by the iterative reconstructed algorithm ART using all 41 momentum projections. The result of the reconstruction is shown in Fig. 7.21 (a) and the original longitudinal phase space from the ASTRA simulation at 2.5 m, upstream the booster, is shown in Fig. 7.18 (a). For this reconstruction, the electron bunch momentum distribution had 432 bins with a bin size of 2 keV/c, and 201 bins were used for the longitudinal coordinate with a bin size of 0.05 mm. The resulting shape of the reconstructed longitudinal phase space is similar to the original simulated one except for additional reconstruction artifacts.

Applying the acceleration model to the reconstructed longitudinal phase space upstream the booster cavity shown in Fig. 7.21 (a), the phase space downstream the booster cavity can be reconstructed. The result is shown in Fig. 7.21 (b) and the original longitudinal phase space from ASTRA simulation at 8.92 m is shown in Fig. 7.18 (b). The core part of the reconstructed longitudinal phase space looks similar to the original one, Fig. 7.21 (b) and Fig. 7.18 (b), except a lot of additional low intensity artifacts.

Using more projections, i.e. more booster RF phases, with finer booster RF phase step, amount and strength of the artifacts can be significantly decreased, Fig. 7.22.

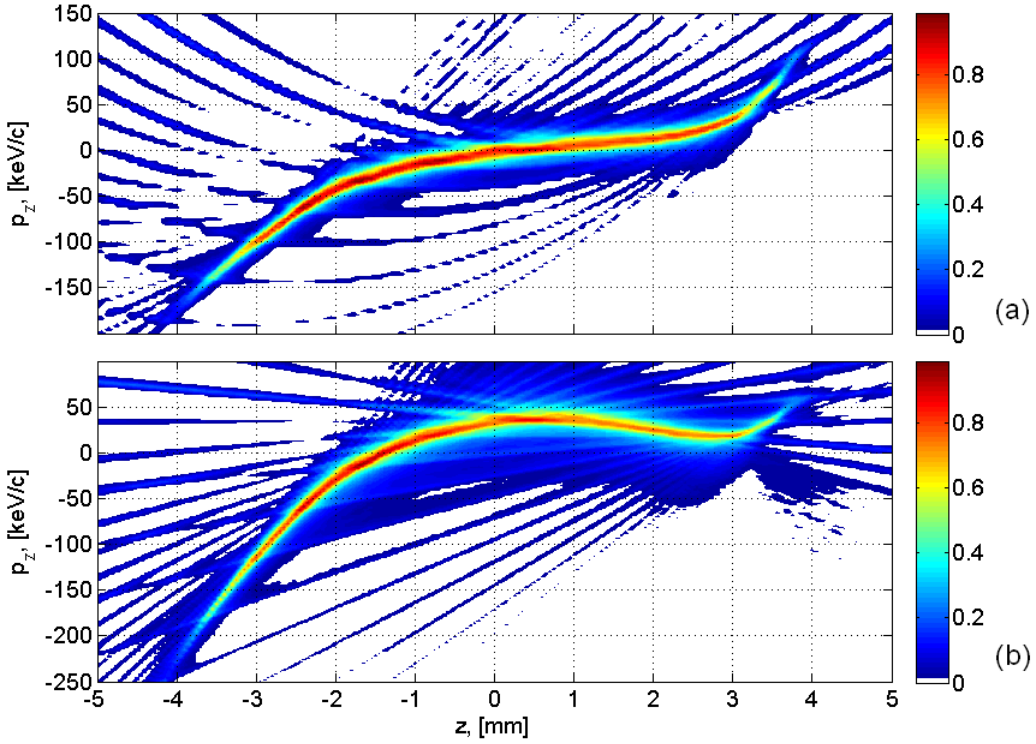

Fig. 7.21: Reconstructed longitudinal phase space upstream (a) and downstream (b) the booster cavity using 41 momentum projections with 1 degree booster RF phase step and 2 keV/c momentum binning.

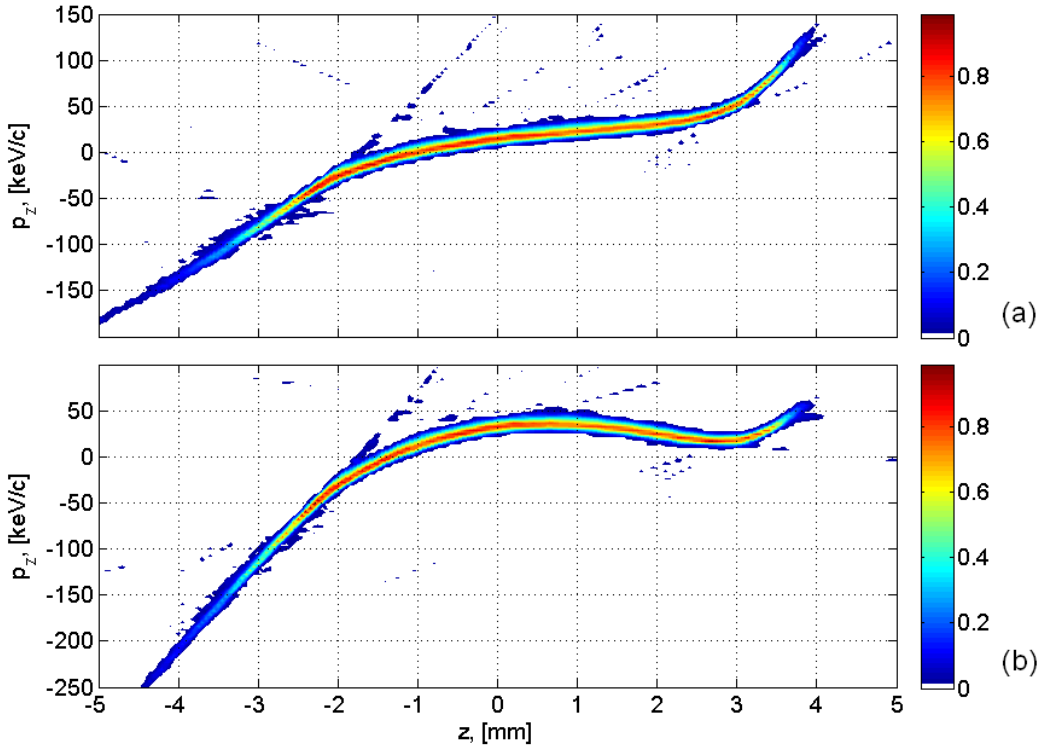

Fig. 7.22: Reconstructed longitudinal phase spaces upstream (a) and downstream (b) the booster cavity using 151 momentum projections with 0.2 degrees booster RF phase step and 4 keV/c momentum binning.

For this reconstruction 151 momentum projections were used for the booster RF phases in the range from -15 to +15 degrees with step of 0.2 degrees. The binning of momentum distribution was decreased to 4 keV/c to have reasonable computation time. The core part of the reconstructed phase spaces is the same but amount of the artifacts around is significantly reduced.

7.4.1 MENT reconstruction algorithm

The algebraic reconstruction technique can be used to perform the tomographic reconstruction, but in some cases it produces a lot of additional artifacts in the reconstructed images as shown, for example, in Fig. 7.21. One of the possible ways to eliminate these artifacts would be using another algorithm, for example, the maximum entropy method (MENT) [43]. An example of such a reconstruction from simulated data is shown in Fig. 7.23 using the MENT algorithm with 2 iterations. The initial data of the electron bunch momentum distributions used for this reconstruction were the same as they were used for the ART reconstruction algorithm, Fig. 7.21, 41 momentum projections.

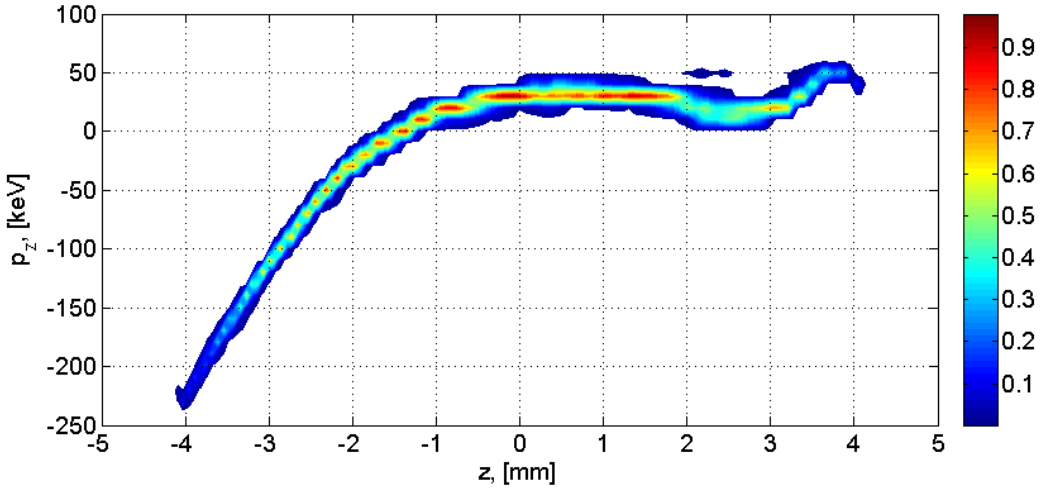

Fig. 7.23: Reconstructed longitudinal phase space using the MENT algorithm from simulated momentum distributions at 8.92 m downstream the gun. For 1 nC bunch charge generated with a flat-top temporal laser profile.

A bin size of the momentum distributions was 2 keV/c and the reconstructed longitudinal axis has a bin size of 0.07 mm. The resulting shape of the reconstructed longitudinal phase space looks similar to the original one from ASTRA simulation, Fig. 7.23 and Fig. 7.18 (b), and has much less additional artifacts as compared with the ART algorithm, Fig. 7.21.

Further iterations of the MENT algorithm start to cause density oscillation in the reconstructed phase space. And also reconstruction from the experimental data does not show convergence with the iteration number when using MENT algorithm. To understand the nature of the oscillations in the reconstruction result and divergence of the algorithm further studies of the application of the MENT algorithm to the longitudinal phase space reconstruction are needed.

7.5 Summary

Simulations of tomographic measurements with the Gaussian temporal laser profile show consistent results, except some insignificant amount of reconstruction artifacts. Less artifacts can be seen for the small charge of 20 pC, and more artifacts for the 700 pC case. Reconstruction artifacts in this case arise from the additive nature of the ART algorithm [44] and insufficient number of the used projections, i.e. too rough booster RF phase steps.

The reconstructed phase space does not significantly degrade when the procedure of momentum distribution measurements is included in the simulations, and still close to the original one. Momentum resolution in this case is limited by the transverse beam size at the reference screen divided by the dispersion. For the

case of 20 pC generated with a Gaussian temporal laser profile it is about 2 keV/c. It is two times less than the limitation from the optical read out system for the HEDA1, which is about 4 keV/c, see section 3.4.

For the case of a flat-top temporal laser profile, the ART reconstruction produces significant amount of artifacts but the shape and the core part of the reconstructed phase spaces are still similar to the original one, calculated from the simulated particles distributions. Using more detailed momentum distributions and finer booster RF phase steps the quality of the reconstruction can be significantly improved.

The MENT algorithm does not have such problems with reconstruction artifacts like ART has and for the same initial data gives consistent result after a small number of iteration steps. But a high number of iterations cause divergence of the algorithm. Further studies are needed to eliminate problems with convergence and density oscillations in the reconstruction results when using the MENT algorithm.

Chapter 8

Longitudinal phase space measurements with tomographic technique

This chapter presents results of longitudinal phase space measurements using the tomographic technique for three different temporal laser profiles and several electron bunch charges. Tomographic reconstructions are done with the ART algorithm that will give in result the longitudinal phase space upstream the booster cavity. Applying the acceleration model to the reconstructed phase space the longitudinal phase space downstream the booster cavity can be reconstructed as well.

8.1 Strategy and varied machine parameters

The measurements of the longitudinal phase space at PITZ were done using the tomographic technique as described in Chapters 6 and 7. The CDS booster RF phase was varied and the corresponding momentum distributions were measured at two dispersive sections: HEDA1 and HEDA2.

All the measurements were done for three photocathode temporal laser profiles and several electron bunch charges. The laser intensity was adjusted to have the defined bunch charge at the High1.ICT1 according to Table 8.1.

Table 8.1: Laser parameters used for measurements.

Bunch charge / Temporal laser profile	20 pC	100 pC	400 pC	700 pC	1 nC
Gauss, 2.7 ps	✓	✓	✓	✓	
Flat-top, 17.4 ps	✓	✓			✓
Modulated, 21.5 ps	✓				✓

The charges were chosen to be the same as the ones used for the numerical simulations of the measurements shown in Chapter 7. Additionally, 100 pC for flat-top and Gaussian temporal laser profiles and 400 pC for Gaussian were measured.

To have the highest momentum resolution at the HEDA1 section the beam was focused vertically on the reference screen High1.Scr5 (see section 3.5). The resulted momentum resolutions were calculated from the vertical beam sizes at this screen according to Eq. (3.3) and summarized in Table 8.2 for the all measurements.

Table 8.2: Momentum resolution at HEDA1.

Temporal laser profile	Bunch charge	Beam size at High1.Scr5, [mm]	Momentum resolution, relative	Momentum resolution, [keV/c]
Gauss, 2.7 ps	20 pC	0.07	$1.2 \cdot 10^{-4}$	2.6
Gauss, 2.7 ps	100 pC	0.32	$5.3 \cdot 10^{-4}$	12.0
Gauss, 2.7 ps	400 pC	0.64	$1.1 \cdot 10^{-3}$	23.9
Gauss, 2.7 ps	700 pC	0.97	$1.6 \cdot 10^{-3}$	36.2
Flat-top, 17.4	20 pC	0.14	$2.3 \cdot 10^{-4}$	5.2
Flat-top, 17.4	100 pC	0.08	$1.3 \cdot 10^{-4}$	3.0
Flat-top, 17.4	1 nC	0.59	$1.0 \cdot 10^{-3}$	22.0
Modulated, 21.5 ps	20 pC	0.32	$5.3 \cdot 10^{-4}$	11.9
Modulated, 21.5 ps	1 nC	0.55	$9.2 \cdot 10^{-4}$	20.5

For the momentum distribution measurements in the HEDA1 section a bin size was 4 keV/c, which corresponds to one pixel of the CCD camera looking at the observation screen, see section 3.4.

For all measurements in the HEDA2 section the beam optics was optimized to have a divergent beam in the horizontal direction upstream the dipole magnet Disp3.D1 by applying a defocusing quadrupole (see section 3.6). For the momentum distribution measurements in the HEDA2 section the bin size was 1.5 keV/c except for one case when, by mistake, it was 3 keV/c for the measurements for 20 pC bunch charge generated with a flat-top temporal laser profile.

8.1.1 Photocathode laser parameters

The following temporal profiles of the photocathode laser were used for the measurements: a Gaussian with a duration of 2.7 ps FWHM, a flat-top with duration of 17.4 ps FWHM and a modulated flat-top with a duration of 21.5 ps FWHM, both with 2 ps rise and fall times. Examples of the corresponding measured temporal laser profiles are shown in Fig. 8.1. Intensities of the flat-top and the modulated flat-top laser pulses for this plot were scaled to have the same integral as for the Gaussian pulse. For all these measurements the head of the laser pulse is on the left side.

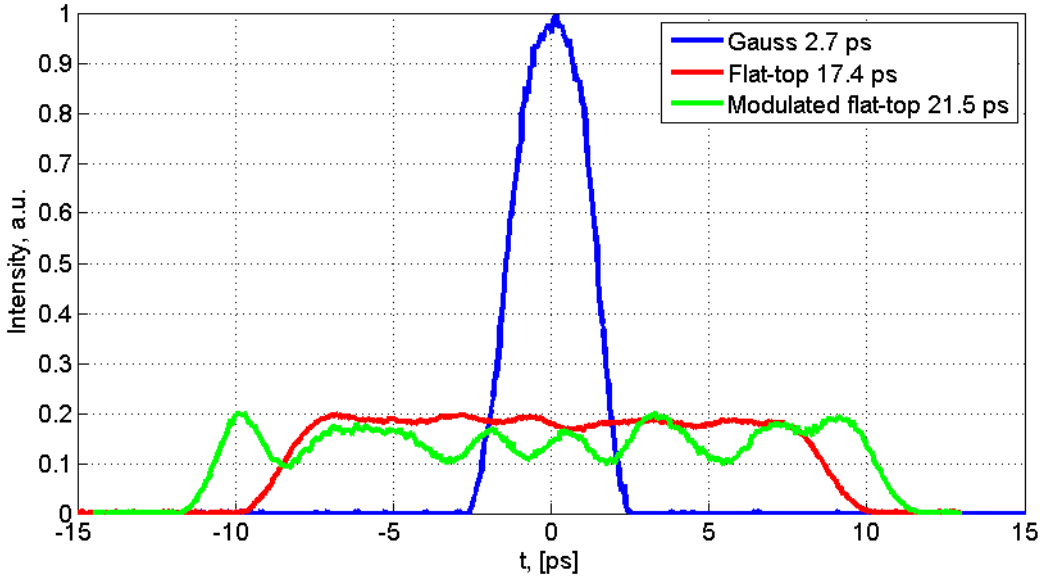

Fig. 8.1: Measured temporal laser profiles: Gaussian with 2.7 ps FWHM duration, the blue curve, flat-top with 17.4 ps FWHM duration and about 2 ps rise and fall times, the red curve, and modulated flat-top with 21.5 ps FWHM duration with about 1 ps rise and fall times, the green curve.

An example of the transverse distribution of the laser beam used for the measurements is shown Fig. 8.2. This distribution was measured at the position of the virtual cathode located at the same distance from the BSA and had the same imaging of the laser beam as the real photocathode [17].

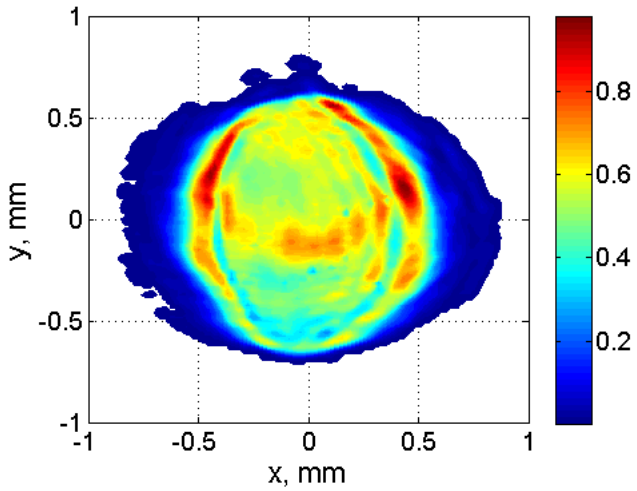

Fig. 8.2: An example of the measured transverse distribution of the photocathode laser at the position of the virtual cathode [17]. The horizontal RMS size is 0.36 mm and the vertical one is 0.37 mm.

The electron bunch charge for the measurements was varied by adjusting the photocathode laser intensity and the charge was measured by the integrating current transformer (ICT) downstream the booster cavity, Fig. 3.1. For the Gaussian temporal laser profile the bunch charge of 700 pC was the maximum extractable for such a laser transverse distribution.

8.1.2 RF gun and booster parameters

The RF power fed to the gun cavity was chosen in a way that 6.7 MeV/c maximum mean momentum at the gun exit was obtained. That corresponds to about 6.8 MW measured peak RF power in the gun and 60.5 MV/m simulated maximum electric field on the cathode surface (gun nominal operation at PITZ). The RF phase of the gun was always adjusted to have maximum mean momentum of the beam downstream the gun.

The main solenoid current was chosen empirically at 377 A for all the measurements as this current delivers a good beam transport up to the HEDA2 section and keeps the beam size relatively small along the whole beamline. The bucking solenoid was always adjusted in such way that it compensates the longitudinal magnetic field created by the main solenoid on the cathode surface.

The RF power fed to the CDS booster cavity was chosen to have the electron bunch maximum mean momentum at the booster exit around 22 MeV/c. That corresponds to about 3.2 MW peak RF power in the booster and 18 MV/m maximum electric field (maximum allowed during measurements).

8.2 Results for Gaussian temporal laser profile

8.2.1 Measurements with 20 pC bunch charge

The result of the mean momentum phase scan in the HEDA1 section is shown in Fig. 8.3 (a) as the blue dots with the statistical error bars from 10 consequent measurements and the RMS momentum spread is shown with the red dots in (b). The measurements were done for the booster RF phases in the range from -28 degrees to +18 degrees with respect to the MMMG phase with the step width of 2 degree, 24 momentum projections in total.

The green curve shows in Fig. 8.3 (a) the beam momentum as a function of the booster RF phase according to the acceleration model described by Eq. (2.42) and partly coincides with the measured data. Parameters for this curve were taken from the maximum mean momentums downstream the gun and booster.

The set point RF phase of the booster cavity at the PITZ facility is flipped with respect to the mathematical phase used in numerical simulations. Therefore all momentum phase scans shown in this Chapter are flipped in order to have mathematical phase on the horizontal axis and easy compare with the simulations.

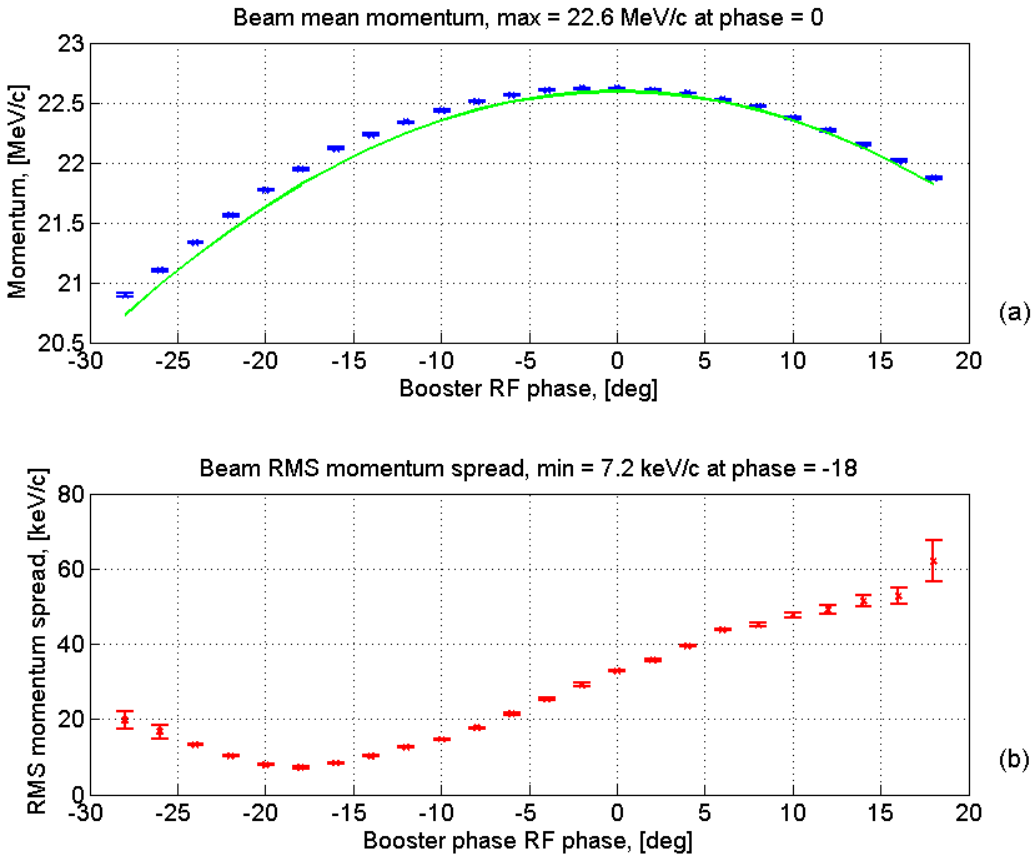

Fig. 8.3: Measured mean beam momentum at the HEDA1 section (a), the blue dots with error bars, and RMS momentum spread (b), the red dots with error bars, as a function of the booster RF phase, for 20 pC bunch charge generated with a Gaussian temporal laser profile. The green curve in (a) is the beam momentum according to the acceleration model described by Eq. (2.42).

The resulting momentum distributions are scaled and normalized according to the procedure introduced in section 6.3. Final data, ready for tomographic reconstruction, are shown in Fig. 8.4 as momentum distributions for different booster RF phases.

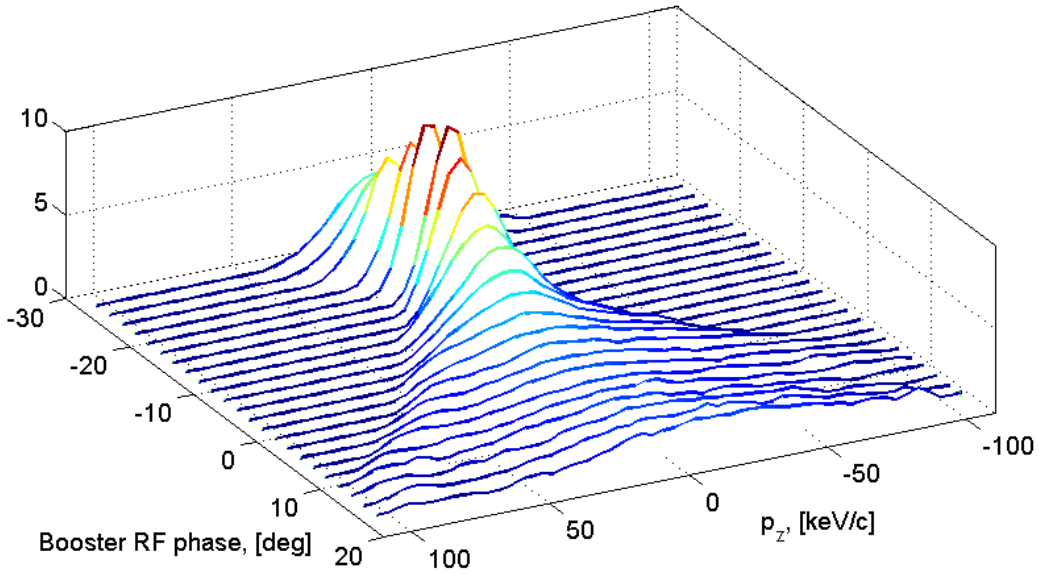

Fig. 8.4: Measured momentum distribution for different booster RF phases. 20 pC bunch charge generated with a Gaussian temporal laser profile.

The longitudinal phase spaces reconstructed using momentum measurements in the HEDA1 and the HEDA2 sections after 100 iterations starting from a zero initial guess are shown in Fig. 8.5. For the HEDA1 it was used 24 momentum projections with the booster RF phase step of 2 degrees and for the HEDA2 it was used 47 momentum projections with the booster RF phase step of 1 degree. The phase spaces are plotted as contour plots without contour lines. The color map corresponds to 64 contour levels with the first level shown as a white color. The results are looking very similar to each other despite of the fact that for the HEDA2 measurements a three times better momentum resolution is expected than for the HEDA1.

The simulated longitudinal phase space upstream the booster cavity at 2.5 m downstream the gun is shown in Fig. 8.6. The numerical simulation was done for the machine parameters adjusted to be close to the parameters used for the measurements. These include: beam momentum downstream the gun, beam momentum downstream the booster, bunch charge, transverse and temporal laser profiles and the main solenoid current, section 7.1.

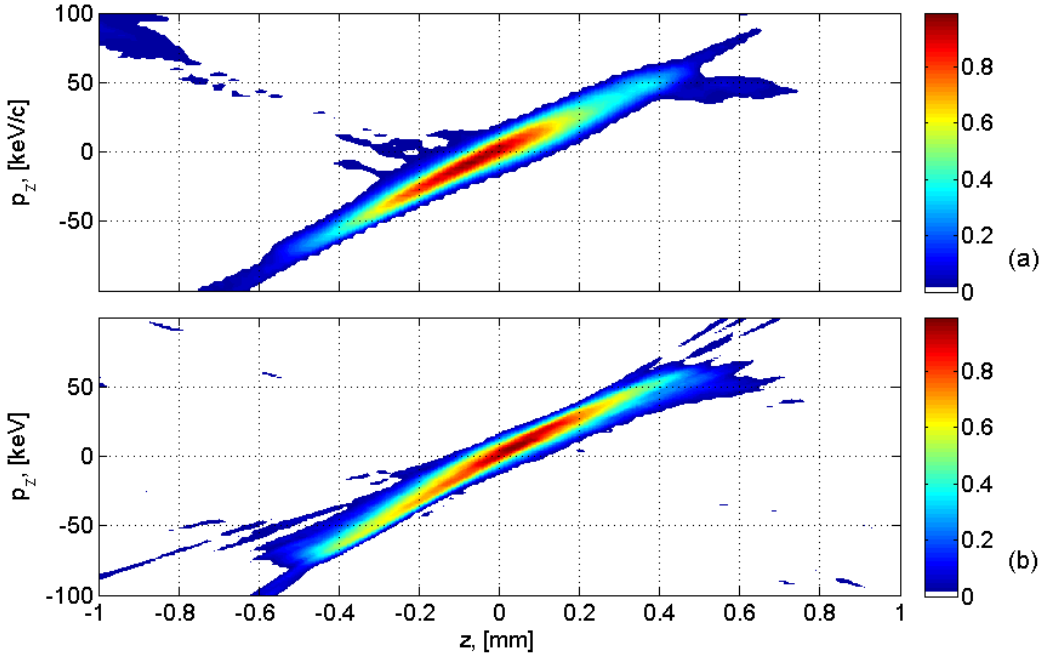

Fig. 8.5: Reconstruction results of the longitudinal phase space upstream the booster cavity for 20 pC bunch charge using the HEDA1 (a) and HEDA2 (b) dispersive sections. For the longitudinal coordinate a bin size of 0.01 mm was used to reconstruct both phase spaces.

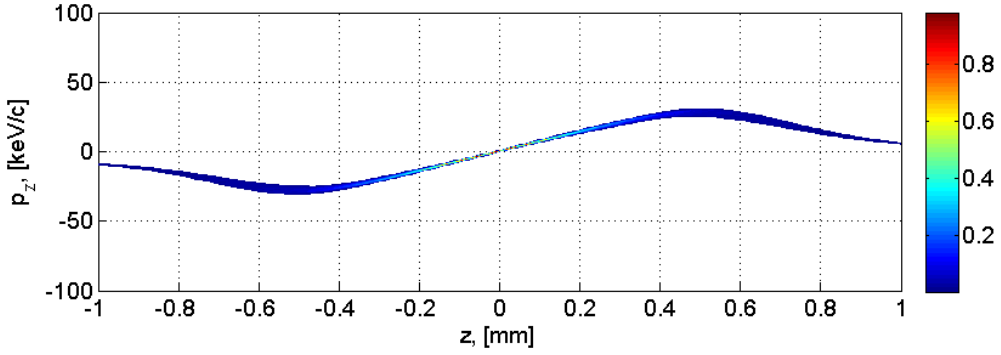

Fig. 8.6: Simulated longitudinal phase space upstream the booster cavity at 2.5 m downstream the gun, for 20 pC bunch charge.

Compared to the measured phase spaces the simulated one looks significantly more narrow: the slice momentum spread at the central part of the simulated phase space is about 1.2 keV/c, whereas the measured ones have about 6-7 keV/c for the same longitudinal slice length of 40 μm taken in the analysis, see Fig. 8.7.

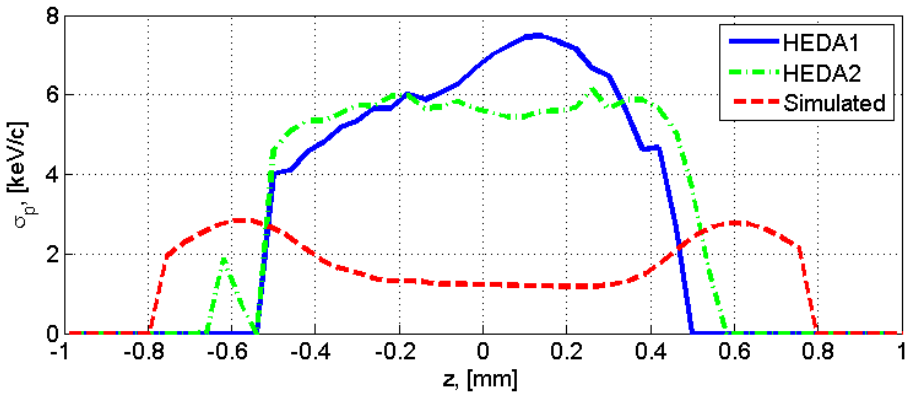

Fig. 8.7: The slice momentum spread calculated from the measured longitudinal phase spaces (Fig. 8.5) is shown with the blue curve for HEDA1 and with the green dot-dashed curve for HEDA2, and the simulated one is shown with the red dashed curve.

The measured slice momentum spread was calculated applying 15% charge cut to the longitudinal phase space in order to remove reconstruction artifacts. This difference between the measured and simulated slice momentum spread, Fig. 8.7, can be explained by insufficient momentum resolution in the used reconstruction momentum distributions. For the HEDA1 measurements the binning of the momentum axis was 4 keV/c. Such a bin size is already three times worse than the simulated slice momentum spread. The HEDA2 section should give better result than HEDA1 as the momentum binning of the measured momentum distribution is 1.5 keV/c versus 4.0 keV/c. But because of not fine optimized beam transport for a good momentum resolution (see section 3.6) the resulted longitudinal phase space has the quality close to the one obtained from the measurements in the HEDA1 section, see Fig. 8.5.

The comparison of the reconstructed current profiles with the measured temporal laser profile is shown in Fig. 8.8. The current profiles was calculated from the reconstructed phase spaces shown in Fig. 8.5 as a horizontal profile applying 15% charge cut in order to remove reconstruction artifacts. The bunch is shorter than the laser pulse, what is in contradiction with the simulation, Fig. 8.9. According to the simulation the bunch should be slightly longer than the laser pulse. One of the possible explanations, it is because of the applied charge cut which cut the tails of the distributions. Another possible one is that the real laser pulse length is a bit shorter than the measured one using the OSS [17]. This will also explain why the location of the measured minimum RMS momentum spread is more far away from the MMMG phase than expected from the numerical simulations, compared Fig. 7.2 and Fig. 8.3.

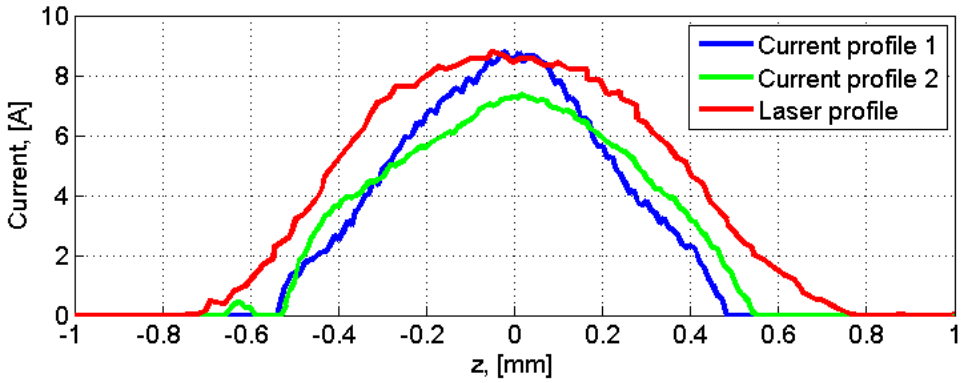

Fig. 8.8: Current profiles calculated from the reconstructed phase spaces shown in Fig. 8.5 (a) – the blue curve, in (b) – the green curve, and the corresponding measured temporal laser profile, the red curve, flipped as compared with Fig. 8.1. The laser profile was scaled vertically to have the same maximum as the first current profile.

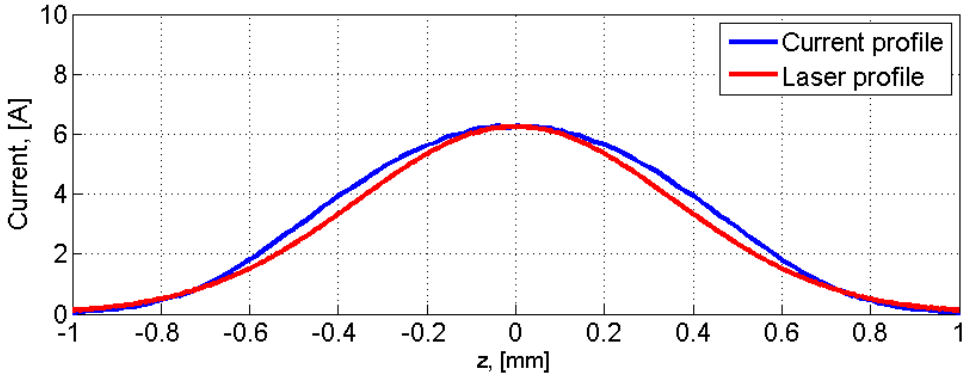

Fig. 8.9: Current profile calculated from the simulated particles distribution shown in Fig. 8.6, the blue curve, and the corresponding temporal laser profile used for the simulation, the red curve. The laser profile was scaled vertically to have the same maximum as the current profile.

8.2.2 Measurements with 100 pC bunch charge

The longitudinal phase spaces reconstructed using momentum measurements in the HEDA1 and the HEDA2 sections are shown in Fig. 8.10. For these reconstructions were used 56 and 46 momentum projections for the HEDA1 and the HEDA2, respectively, with the booster RF phase step of 1 degree. Whereas the reconstructed phase spaces looks differently, the slope (momentum chirp) and the core part are similar. The long tales for both reconstructed phase spaces can be explained by the incorrect range of the booster RF phases used for these

measurements. This, in result, causes insufficient rotation of the bunch longitudinal phase space for the complete tomographic reconstruction.

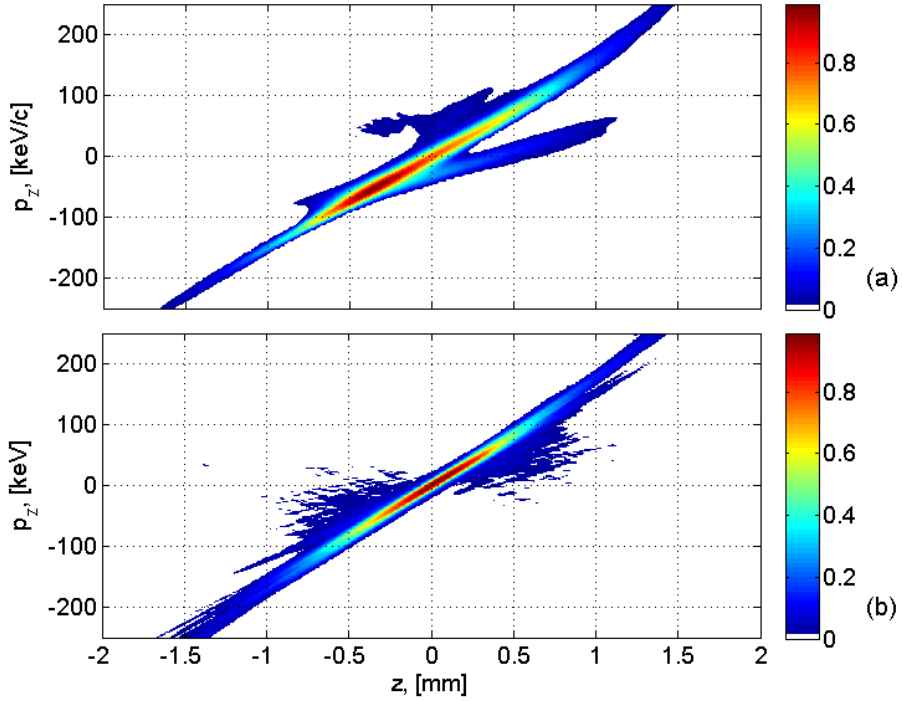

Fig. 8.10: Reconstruction results of the longitudinal phase space upstream the booster cavity for 100 pC bunch charge using HEDA1 (a) and HEDA2 (b) dispersive sections. For the longitudinal coordinate a bin size of 0.02 mm was used to reconstruct both phase spaces.

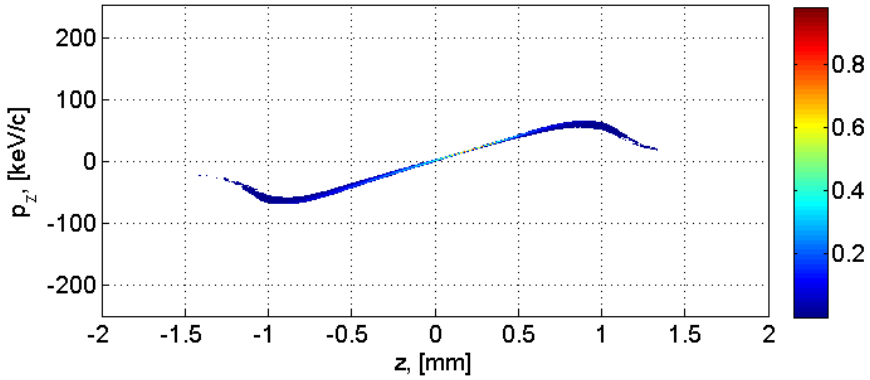

Fig. 8.11: Simulated longitudinal phase space upstream the booster cavity at 2.5 m downstream the gun, for 100 pC bunch charge.

As compared to the simulated longitudinal phase space the reconstructed ones have a higher slope, about 150 keV/mm versus 100 keV/mm, Fig. 8.10 versus Fig. 8.11. The slope of the phase spaces are close to the 20 pC case, Fig. 8.5, but the bunch is longer for 100 pC. This can be explained by the space charge forces, which start to stretch the bunch for the higher charge.

Both calculated longitudinal profiles from the HEDA1 and HEDA2 data are longer than the laser pulse, Fig. 8.12, what is also expected from the numerical simulation for this case, Fig. 8.13.

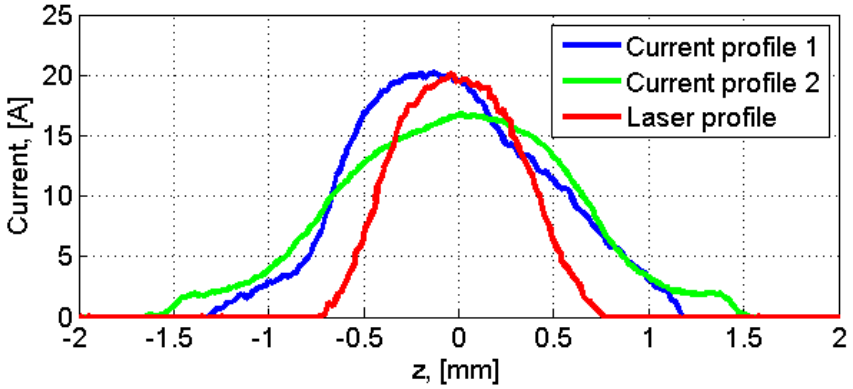

Fig. 8.12: Current profile calculated from the reconstructed phase space shown in Fig. 8.10 (a) – the blue curve, in (b) – the green curve, and the corresponding measured temporal laser profile, the red curve, flipped as compared with Fig. 8.1. The laser profile was scaled vertically to have the same maximum as the current profile.

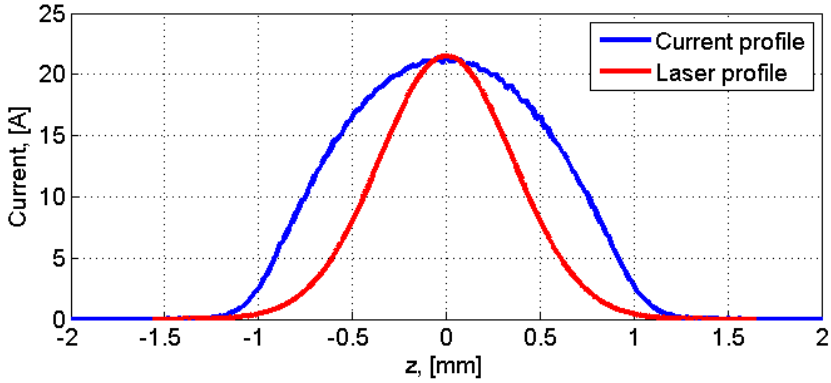

Fig. 8.13: Current profile calculated from the simulated particles distribution shown in Fig. 8.11, the blue curve, and the corresponding temporal laser profile used for the simulation, the red curve. The laser profile was scaled vertically to have the same maximum as the current profile.

8.2.3 Measurements with 400 pC bunch charge

Results of the reconstructed longitudinal phase spaces using momentum measurements in the HEDA1 and the HEDA2 sections are shown in Fig. 8.14 (a) and (b), respectively. For these reconstructions were used 54 and 47 momentum projections for the HEDA1 and the HEDA2, respectively, with the booster RF phase step of 1 degree. Result of the simulated longitudinal phase space with the corresponding machine parameters is shown in Fig. 8.15.

The reconstructed phase space from the HEDA1 data, Fig. 8.14 (a), looks different from the simulated one, shown in Fig. 8.15. Vertically wider reconstructed phase space comes from the insufficient momentum resolution of 24 keV/c, Table 8.2. The reason of such big difference between the phase spaces reconstructed from different dispersive section is not clear. One of the possible explanations it is the instability of the RF source of the gun, which causes different rotation of the longitudinal phase space at the gun exit during the measurements. The reconstructed phase space from the HEDA2 data, Fig. 8.14 (b), looks more close to the simulated one. Most probably during these measurements the RF stability was much better. Also vertically thinner phase space comes from the better momentum resolution of the HEDA2 section.

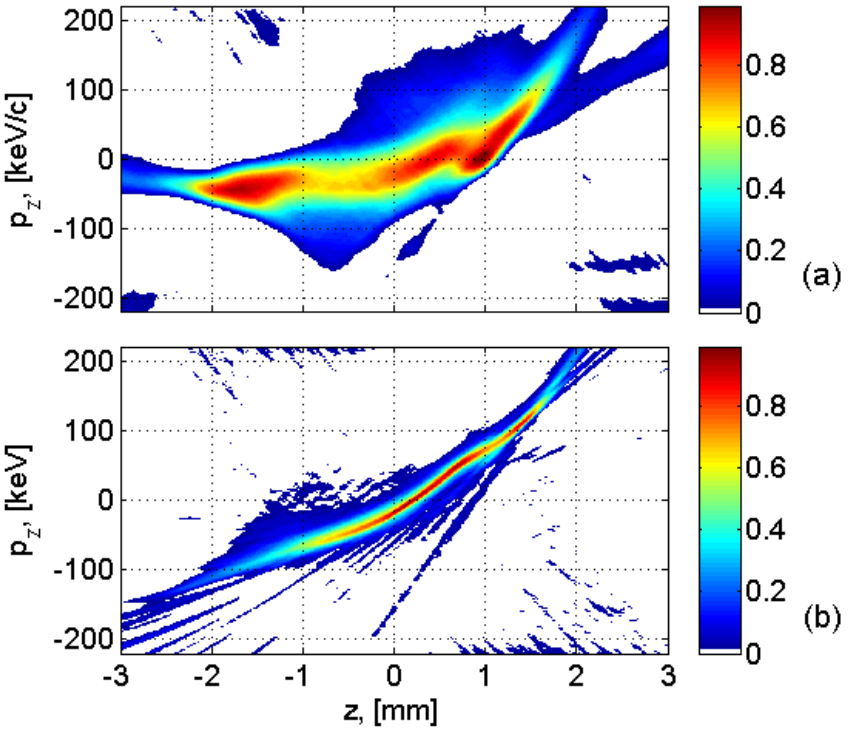

Fig. 8.14: Reconstruction results of the longitudinal phase space upstream the booster cavity for 400 pC bunch charge using HEDA1 (a) and HEDA2 (b) dispersive sections. For the longitudinal coordinate a bin size of 0.025 mm was used to reconstruct both phase spaces.

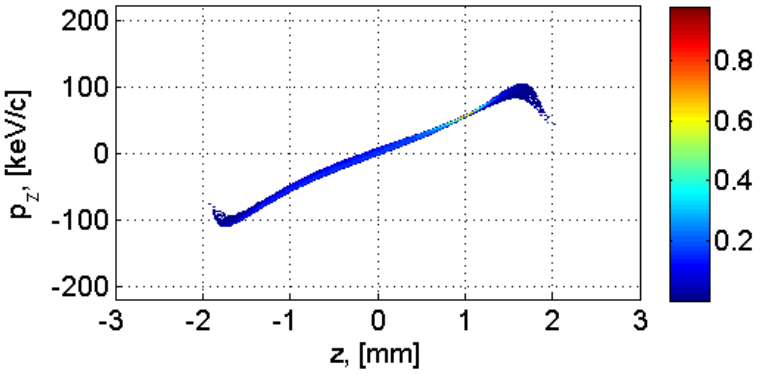

Fig. 8.15: Simulated longitudinal phase space upstream the booster cavity at 2.5 m downstream the gun, for 400 pC bunch charge.

Calculated bunch longitudinal profiles are much longer than the laser profile, Fig. 8.16, what is also predicted by the numerical simulation, Fig. 8.17.

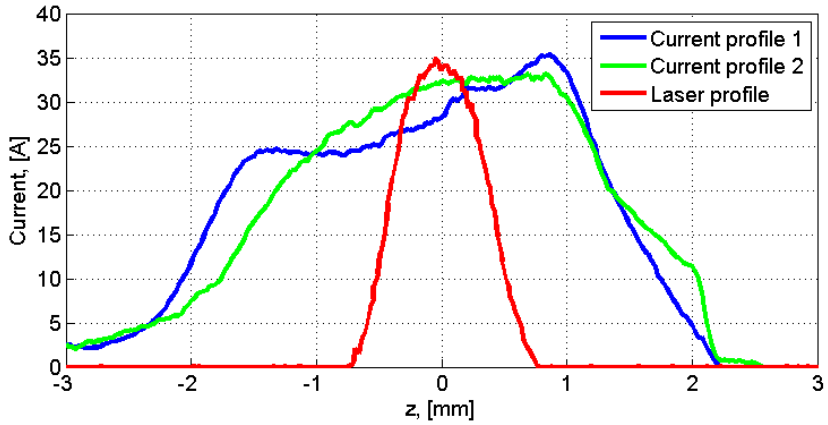

Fig. 8.16: Current profiles calculated from the reconstructed phase spaces shown in Fig. 8.14 (a) – the blue curve, in (b) – the green curve, and the corresponding measured temporal laser profile, the red curve, flipped as compared with Fig. 8.1. The laser profile was scaled vertically to have the same maximum as the first current profile.

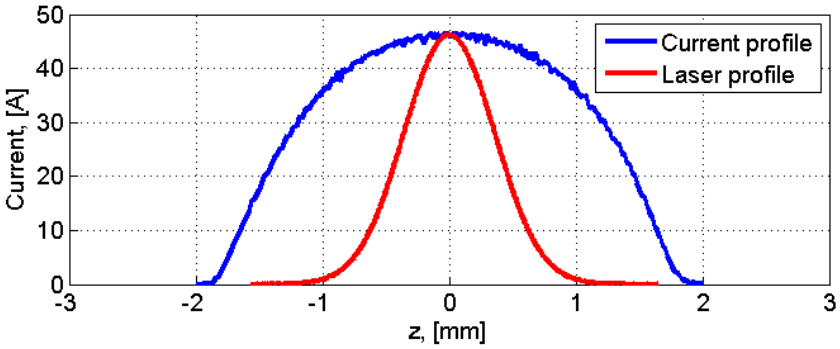

Fig. 8.17: Current profile calculated from the simulated particles distribution shown in Fig. 8.15, the blue curve, and the corresponding temporal laser profile used for the simulation, the red curve. The laser profile was scaled vertically to have the same maximum as the current profile.

8.2.4 Measurements with 700 pC bunch charge

Results of the reconstructed longitudinal phase spaces calculated using momentum measurements at the HEDA1 and the HEDA2 sections are shown in Fig. 8.18 (a) and (b) correspondingly. For these reconstructions were used 48 and 47 momentum projections for the HEDA1 and the HEDA2, respectively, with the booster RF phase step of 1 degree. The corresponding simulated longitudinal phase space is shown in Fig. 8.19. The result from the HEDA1 section, Fig. 8.18 (a), looks vertically wider than from the HEDA2 section and the simulated one because of low momentum resolution. Another difference compared to the simulated phase space is the two hills of the phase space barely noticeable in this figure. In the three-dimensional view they are more pronounced, Fig. 8.20. Also this temporal structure can be seen in the current profile shown in Fig. 8.21. This two hills structure can be explained by the presence of strong space charge forces during charge emission from the cathode. The head of the bunch, already released by the cathode, produces strong electric field on the cathode surface and does not allow the tail of the bunch to be released. This electric field is decreasing with the distance between the cathode and the head of the bunch and, as a result, later the tail of the bunch is leaving the cathode as well. Finally, the bunch will have two hills structure, as shown in Fig. 8.20. But the reconstructed phase space using the momentum measurements from the HEDA2 section doesn't show such effect, Fig. 8.18 (b).

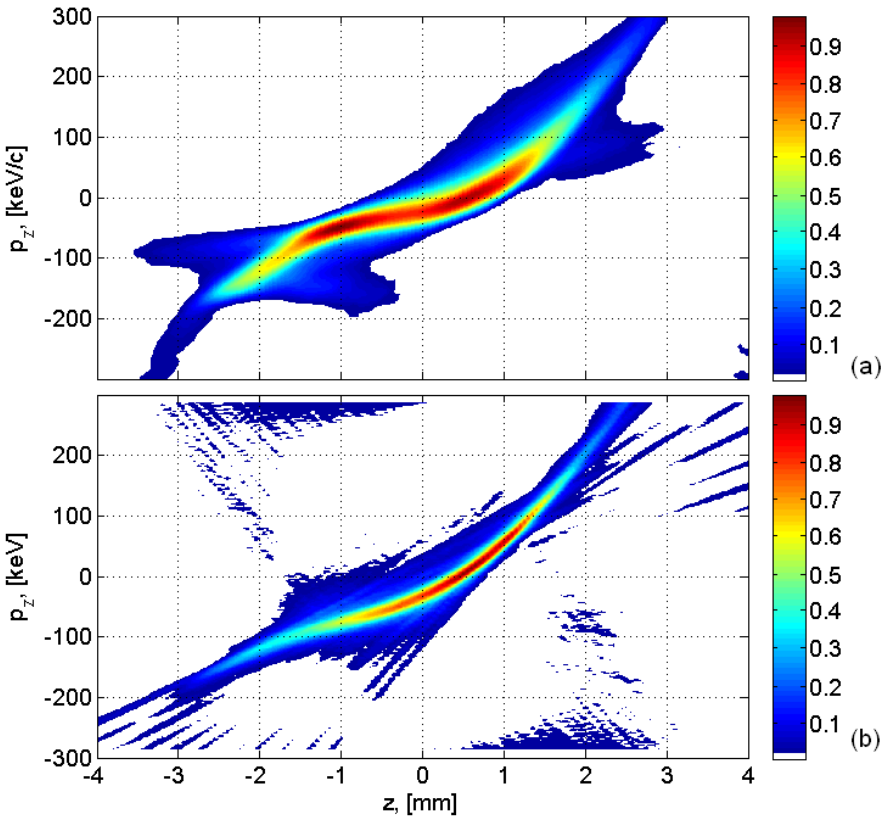

Fig. 8.18: Reconstruction result of the longitudinal phase space for 700 pC bunch charge using HEDA1 (a) and HEDA2 (b) dispersive sections. For the longitudinal coordinate a bin size of 0.05 mm was used to reconstruct both phase spaces.

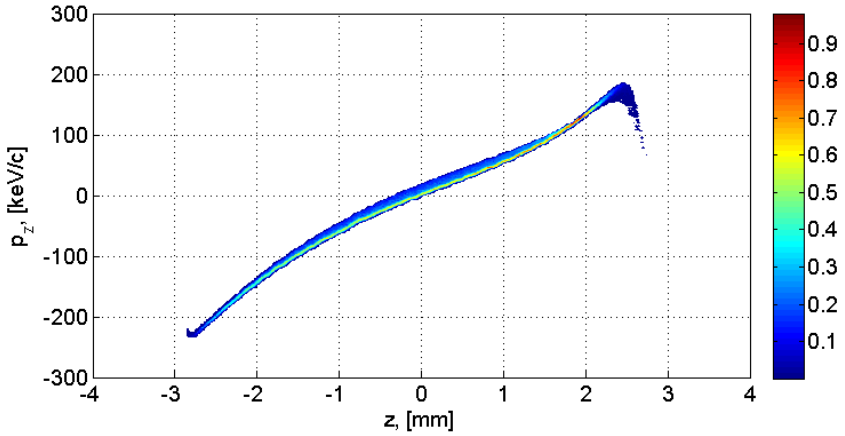

Fig. 8.19: Simulated longitudinal phase space upstream the booster cavity at 2.5 m downstream the gun, for 700 pC bunch charge.

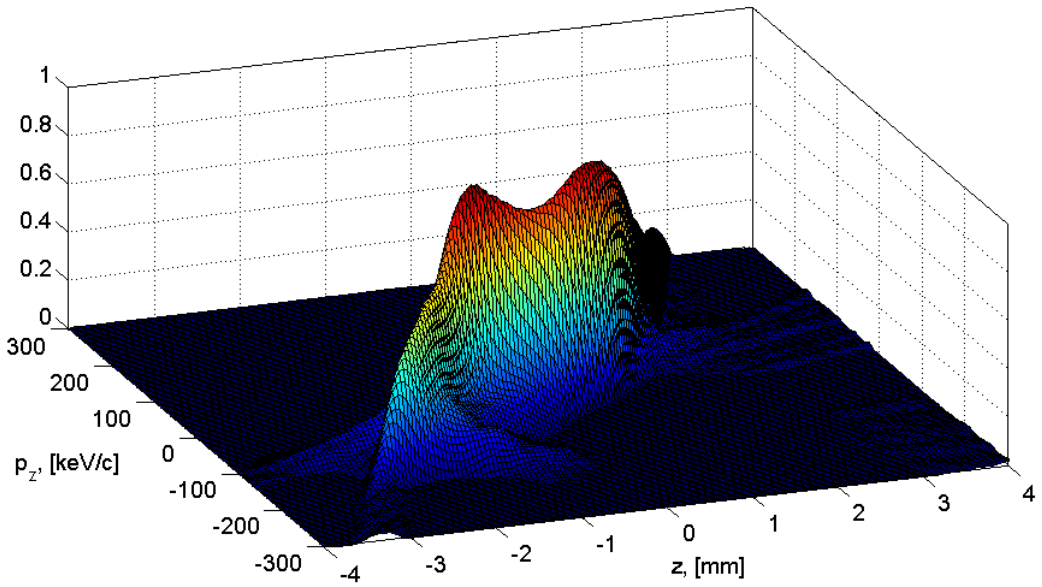

Fig. 8.20: Three-dimensional view of the reconstructed longitudinal phase space shown in Fig. 8.18 (a).

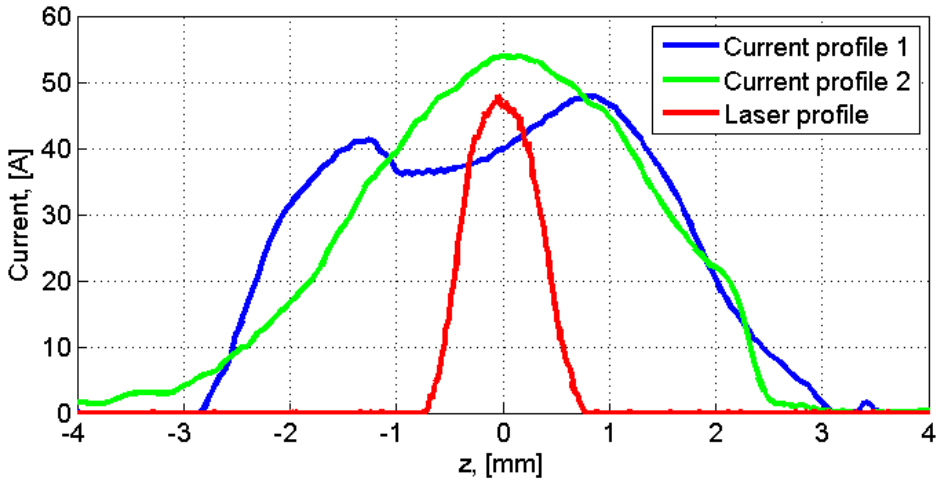

Fig. 8.21: Current profiles calculated from the reconstructed phase spaces shown in Fig. 8.18 (a) – the blue curve, in (b) – the green curve, and the corresponding measured temporal laser profile, the red curve, flipped as compared with Fig. 8.1. The laser profile was scaled vertically to have the same maximum as the first current profile.

Calculated bunch profiles for the both reconstructed longitudinal phase spaces are much longer than the photocathode laser pulse, Fig. 8.21. Such effect comes from the strong space charge forces which elongate the bunch during acceleration

and propagation along the beamline. This also can be seen in numerical simulation, Fig. 8.22.

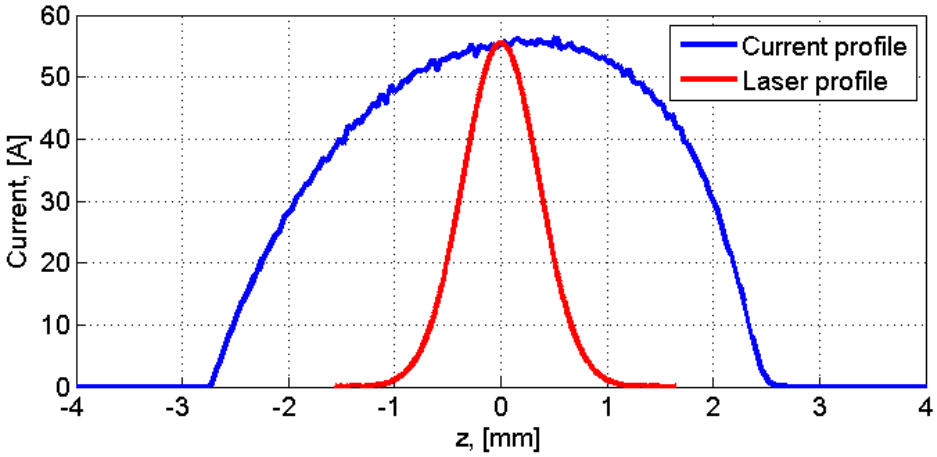

Fig. 8.22: Current profile calculated from the simulated particles distribution shown in Fig. 8.19, the blue curve, and the corresponding temporal laser profile used for the simulation, the red curve. The laser profile was scaled vertically to have the same maximum as the current profile.

Asymmetry in the simulated current profile of the bunch can be explained also by the strong space charge forces during emission, when the emitted head of the bunch pushing back the tail. As a result tail of the bunch become longer, causing such asymmetry. Similar asymmetry can be found in the bunch profiles from the reconstructed phase spaces, Fig. 8.21. For the smaller charge of 400 pC this effect is not seen in simulation, Fig. 8.17, but in the measurement results it is already present, Fig. 8.16.

8.3 Results for flat-top temporal laser profile

8.3.1 Measurements with 20 pC bunch charge

The result of the electron bunch mean momentum phase scan in the HEDA1 section is shown in Fig. 8.23 (a) as the blue dots with statistical error bars from 10 subsequent measurements and the RMS momentum spread is shown with the red dots in (b). The momentum measurements were done for the booster RF phases in the range from -23 to + 22 degrees with respect to the MMMG phase with the step width of 1 degree, 46 momentum projections in total.

The green curve in Fig. 8.23 (a) shows the mean beam momentum as a function of the booster RF phase according to the acceleration model described by Eq. (2.42) and partly coincides with the measured data. Parameters for this curve were taken from the maximum mean momentums measured downstream the gun and booster.

The resulting momentum distributions are scaled and normalized according to the procedure introduced in section 6.3. Final data, ready for tomographic reconstruction, are shown in Fig. 8.24 as momentum distributions for different booster RF phases.

The reconstructed longitudinal phase spaces using momentum measurements in the HEDA1 and the HEDA2 sections are shown in Fig. 8.25 (a) and (b) correspondingly. For the reconstructions were used 46 momentum projections at the HEDA1 and 39 projections at the HEDA2 with the booster RF phase step of 1 degree. The reconstructed phase spaces have a similar shape and temporal structure except that the one reconstructed from the HEDA1 data (a) is much wider than the one reconstructed from the HEDA2 data (b). This comes from the fact that the HEDA2 has a much higher performance for the momentum measurements than the HEDA1 (see sections 3.5 and 3.6). Also the phase space presented in Fig. 8.25 (b) can be improved if a 1.5 keV/c momentum binning would be used for the momentum measurements, which come from the readout optics of the screen station and the camera settings (see section 3.4). Such improvement would result in a phase space much closer to the one expected from the numerical simulation, see Fig. 8.26.

Applying the acceleration model to the reconstructed phase space the longitudinal phase space downstream the booster cavity can obtained. The results are shown in Fig. 8.27 and the corresponding simulated longitudinal phase space downstream the booster cavity is shown in Fig. 8.28.

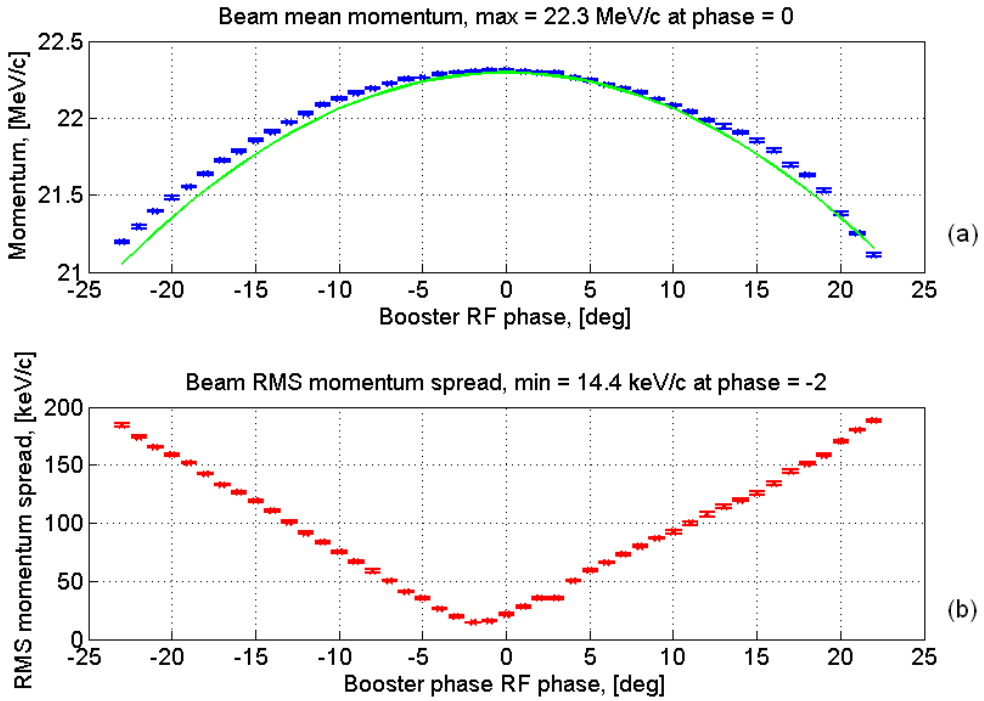

Fig. 8.23: Measured beam mean momentum (a), the blue dot with the error bars, and beam RMS momentum spread (b), the red dots with the error bars, as a function of the booster RF phase for the 20 pC bunch charge. The green curve (a) is the beam momentum according to acceleration model described by Eq. (2.42).

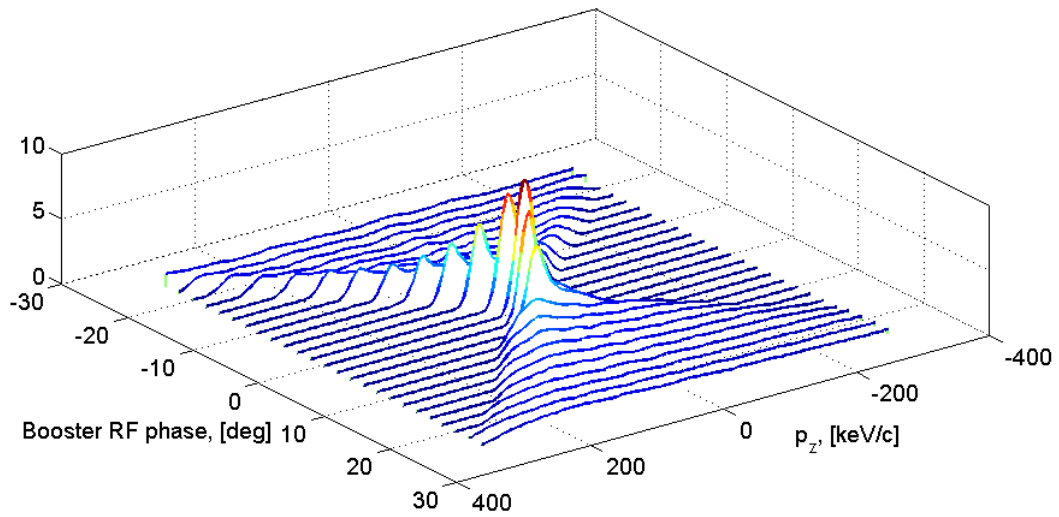

Fig. 8.24: Measured momentum distributions for different booster RF phases plotted with the RF phase step of 2 degrees.

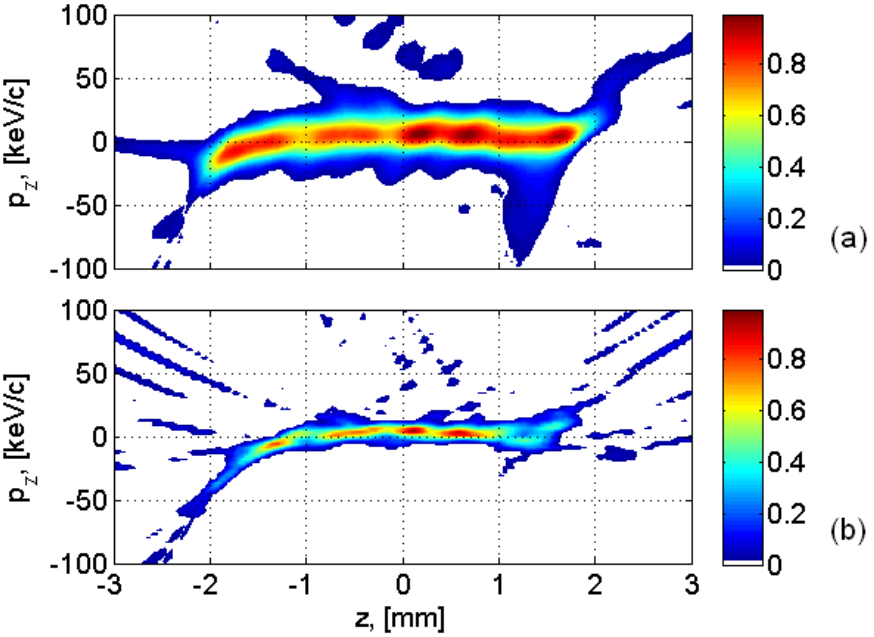

Fig. 8.25: Reconstruction result of the longitudinal phase space upstream the booster cavity using the HEDA1 (a) and the HEDA2 (b) dispersive sections. For the longitudinal coordinate a bin size of 0.025 mm was used to reconstruct both phase spaces.

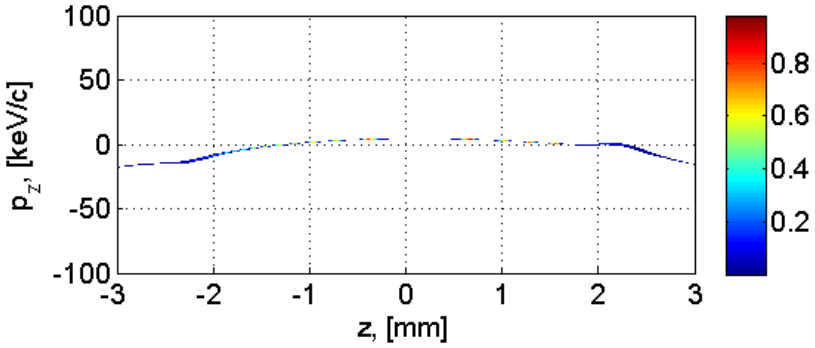

Fig. 8.26: Simulated longitudinal phase space upstream the booster cavity at 2.5 m downstream the gun.

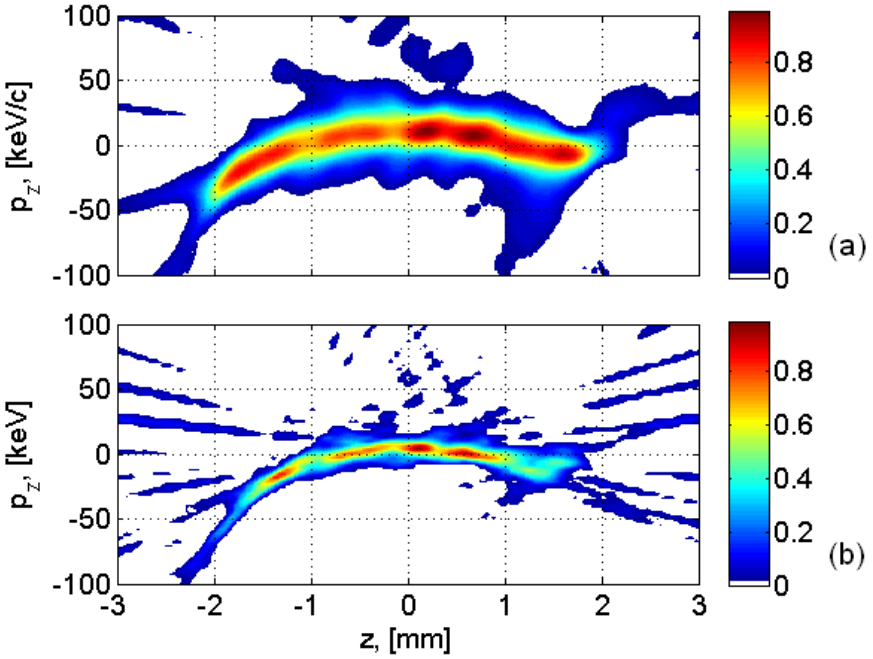

Fig. 8.27: Reconstruction result of the longitudinal phase space downstream the booster cavity using the HEDA1 (a) and the HEDA2 (b) dispersive sections.

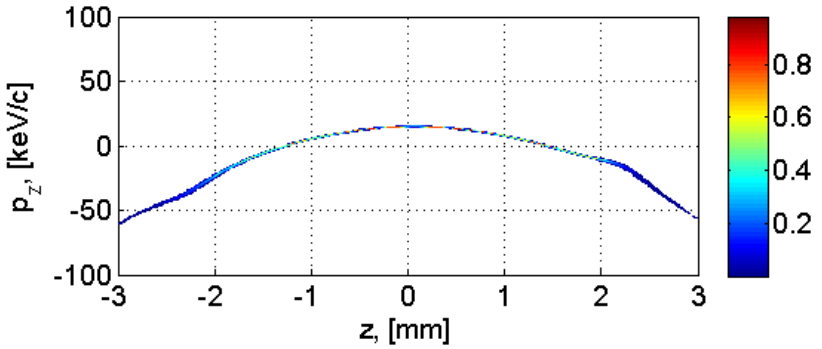

Fig. 8.28: Simulated longitudinal phase space downstream the booster at 8.92 m downstream the gun.

The temporal structures of the reconstructed phase spaces are in good agreement with the temporal laser profile, see current profiles in Fig. 8.29. The current profiles were calculated from the reconstructed longitudinal phase spaces shown in Fig. 8.25 applying 15% charge cut in order to remove the reconstruction artifacts.

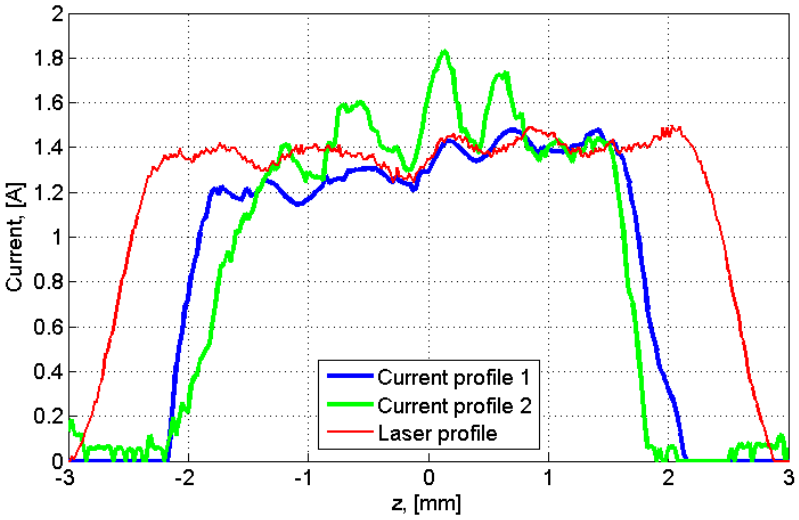

Fig. 8.29: Current profiles calculated from the reconstructed phase spaces shown in Fig. 8.25 (a) – the blue curve, in (b) – the green curve, and the corresponding measured temporal laser profile, the red curve, flipped as compared with Fig. 8.1. The laser profile was scaled vertically to have the same maximum as the first current profile.

Due to the fact that the bunch is slightly compressed during acceleration in the gun the current profile is shorter than the laser pulse [47]. Also this can be seen in the simulation, Fig. 8.30. As a result it is hard to directly compare the current profile with the temporal laser profile.

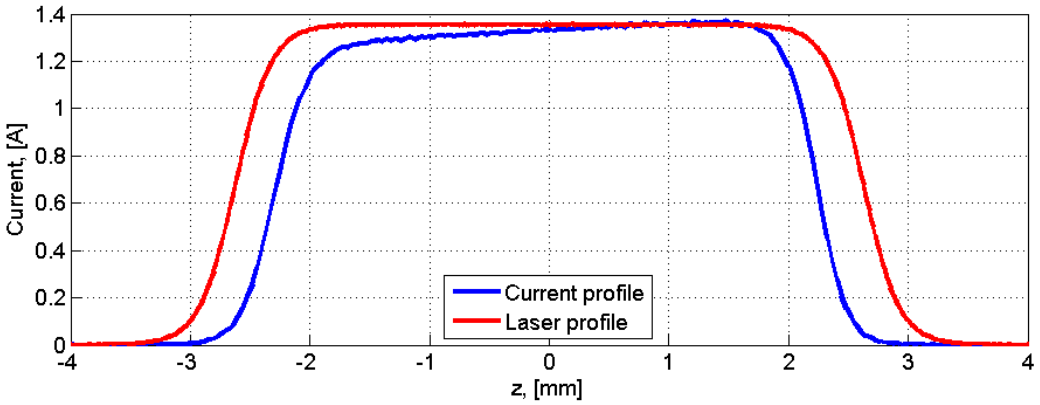

Fig. 8.30: Current profile calculated from the simulated particles distribution shown in Fig. 8.26, the blue curve, and the corresponding temporal laser profile used for the simulation, the red curve. The laser profile was scaled vertically to have the same maximum as the current profile.

This comparison can be simplified by applying the scaling of the temporal axis for the laser profile, see Fig. 8.31 where the temporal axis of the laser profile was scaled down by 0.75.

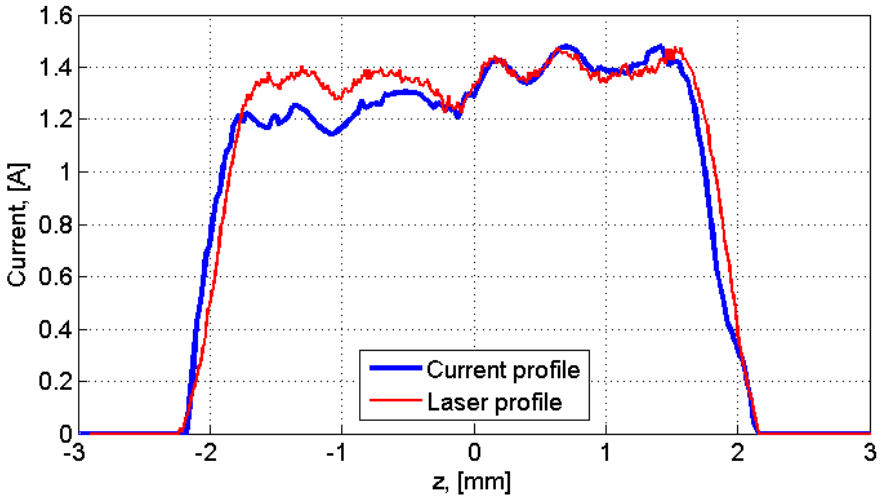

Fig. 8.31: Current profile and the squeezed temporal laser profile from Fig. 8.29.

In Fig. 8.31 in the head of the current profile from 0 to 1.6 mm three bumps are clearly seen which almost coincide with the three bumps in the laser profile. The two left bumps in the tail of the laser pulse, from -1.6 mm to 0, can be recognized in the current profile as well. Similar temporal structure can be observed in the current profile calculated based on the HEDA2 data, Fig. 8.29 the green curve.

8.3.2 Measurements with 100 pC bunch charge

The longitudinal phase spaces reconstructed from the momentum measurements in the HEDA1 and the HEDA2 sections are shown in Fig. 8.32, and the corresponding simulated longitudinal phase space is shown in Fig. 8.33. The phase space reconstructed from the HEDA2 data looks worse than one from the HEDA1 data. This can be explained by not optimum beam preparation for these HEDA2 momentum measurements, causing as a result a bad momentum resolution. Both phase spaces are much wider than the simulated one due to insufficient momentum resolution at both dispersive sections.

The corresponding current profiles calculated by applying 15% charge cut to the reconstructed phase spaces are shown in Fig. 8.34 together with the temporal laser profile used for these measurements. The current profile calculated from the HEDA1 data has some temporal structure but it is hard to compare it with the temporal laser profile. Nevertheless, in the reconstructed phase space shown in Fig. 8.32 (a) the structure of the temporal laser profile can be recognized.

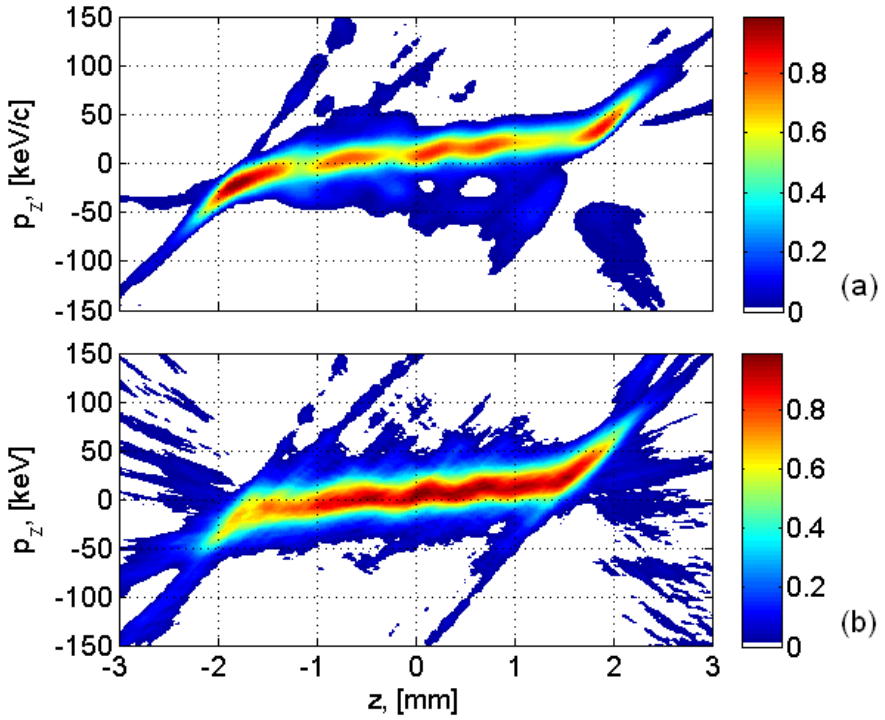

Fig. 8.32: Reconstruction result of the longitudinal phase space upstream the booster cavity using the HEDA1 (a) and the HEDA2 (b) dispersive sections. For the longitudinal coordinate a bin size of 0.05 mm was used to reconstruct both phase spaces.

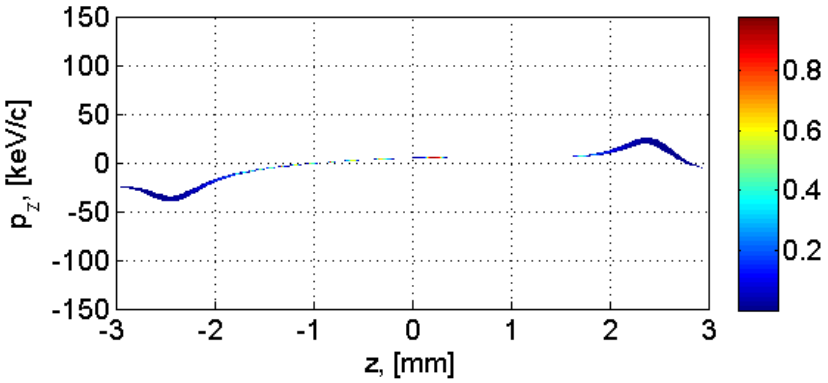

Fig. 8.33: Simulated longitudinal phase space upstream the booster cavity at 2.5 m downstream the gun.

The results of the current profile measurements show that the bunch gets shorter than the laser pulse for this charge as well as for 20 pC case, which also can be seen in the numerical simulations, Fig. 8.35.

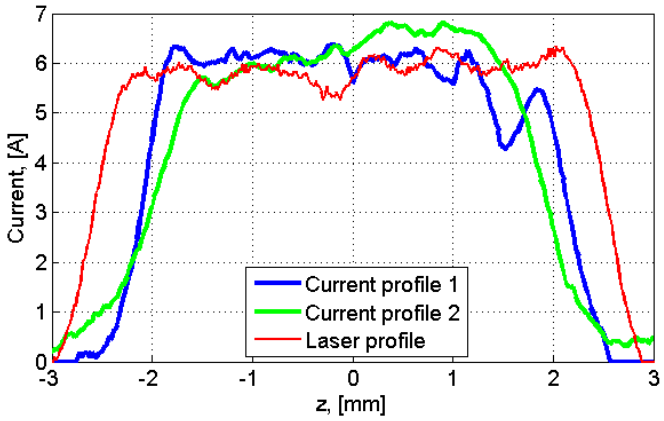

Fig. 8.34: Current profiles calculated from the reconstructed phase spaces shown in Fig. 8.32 (a) – the blue curve, in (b) – the green curve, and the corresponding measured temporal laser profile, the red curve, flipped as compared with Fig. 8.1. The laser profile was scaled vertically to have the same maximum as the first current profile.

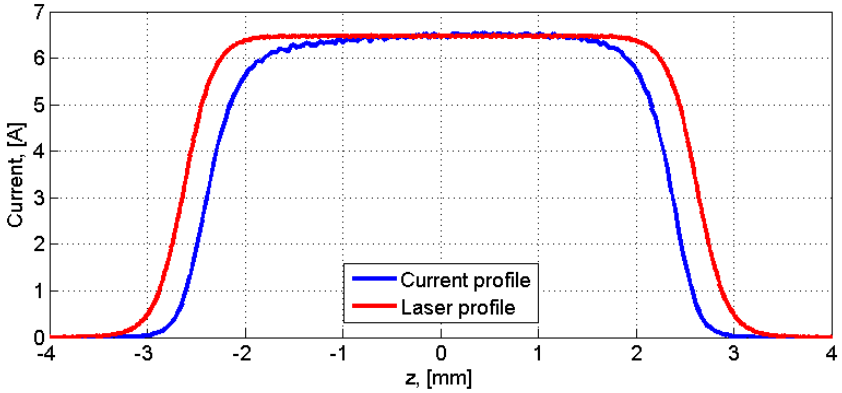

Fig. 8.35: Current profile calculated from the simulated particles distribution shown in Fig. 8.33, the blue curve, and the corresponding temporal laser profile used for the simulation, the red curve. The laser profile was scaled vertically to have the same maximum as the current profile.

8.3.3 Measurements with 1 nC bunch charge

The longitudinal phase spaces reconstructed from the momentum measurements in the HEDA1 and the HEDA2 sections are shown in Fig. 8.36 and the corresponding simulated longitudinal phase space is shown in Fig. 8.37. The both reconstructed phase spaces are much different from the simulated one, but the one reconstructed from the HEDA2 data has the similar trend, compared Fig. 8.36 (b) and Fig. 8.37. The wider phase space reconstructed from the HEDA1

data is expected from the worse momentum resolution of about 22 keV/c, see Table 8.2.

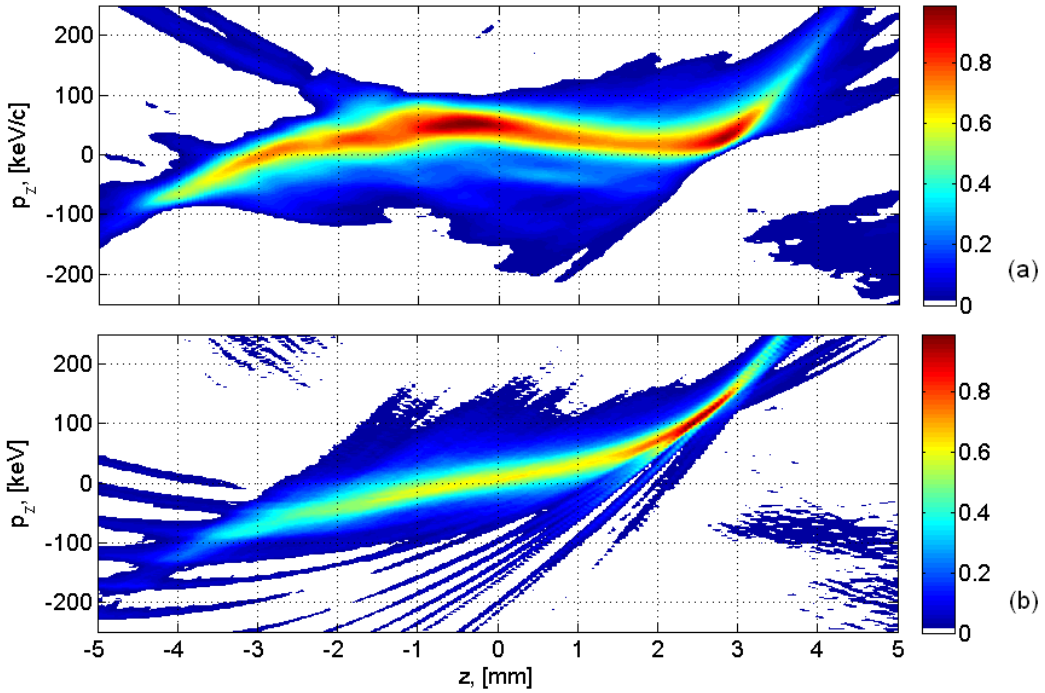

Fig. 8.36: Reconstruction result of the longitudinal phase space using the HEDA1 (a) and the HEDA2 (b) dispersive sections. For the longitudinal coordinate a bin size of 0.05 mm was used to reconstruct both phase spaces.

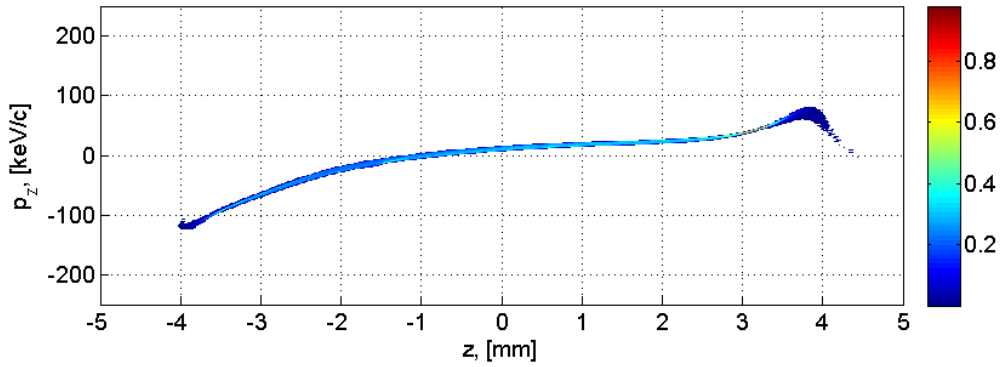

Fig. 8.37: Simulated longitudinal phase space upstream the booster cavity at 2.5 m downstream the gun.

The corresponding current profiles calculated by applying 15% charge cut to the reconstructed phase spaces are shown in Fig. 8.38 together with the temporal laser profile used for these measurements. The related profiles calculated from the simulated data are shown in Fig. 8.39. For the bunch charge of 1 nC the bunch current profile gets longer than the laser pulse what can be seen in the measurements, Fig. 8.38, and also in the numerical simulations, Fig. 8.39.

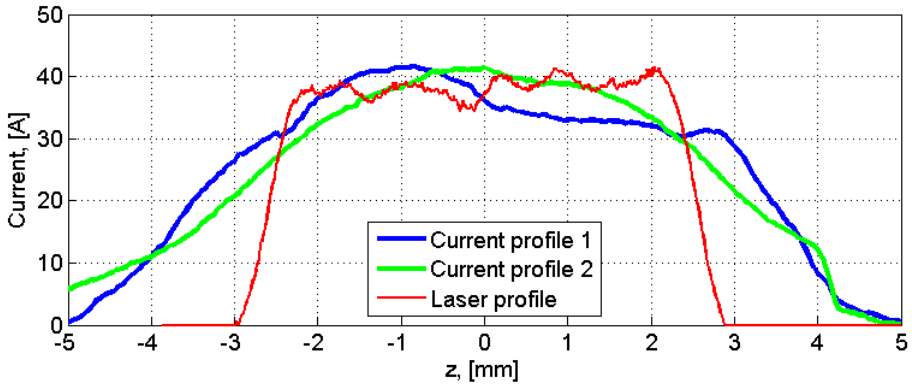

Fig. 8.38: Current profiles calculated from the reconstructed phase spaces shown in Fig. 8.36 (a) – the blue curve, in (b) – the green curve, and the corresponding measured temporal laser profile, the red curve, flipped as compared to Fig. 8.1. The laser profile was scaled vertically to have the same maximum as the first current profile.

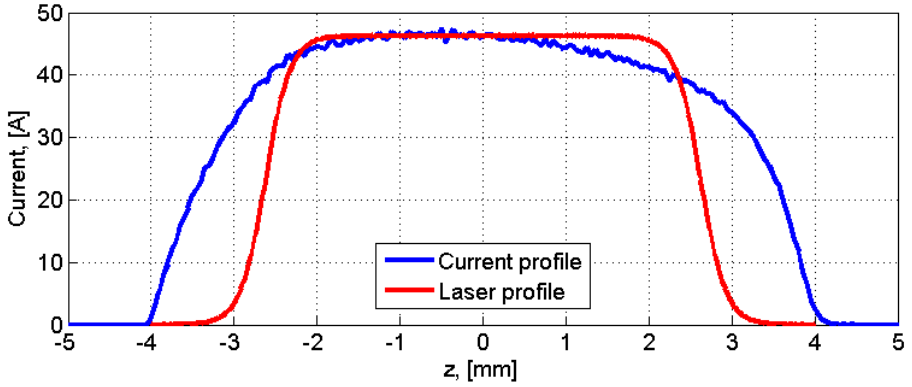

Fig. 8.39: Current profile calculated from the simulated particles distribution shown in Fig. 8.37, the blue curve, and the corresponding temporal laser profile used for the simulation, the red curve. The laser profile was scaled vertically to have the same maximum as the current profile.

8.4 Results for modulated flat-top temporal laser profile

The reconstructed longitudinal phase spaces upstream the booster cavity for 20 pC bunch charge using the momentum measurements in the HEDA1 and the HEDA2 sections are shown in Fig. 8.40. For these reconstructions 42 and 32 momentum projections were used, respectively, with the booster RF phase step of 1 degree.

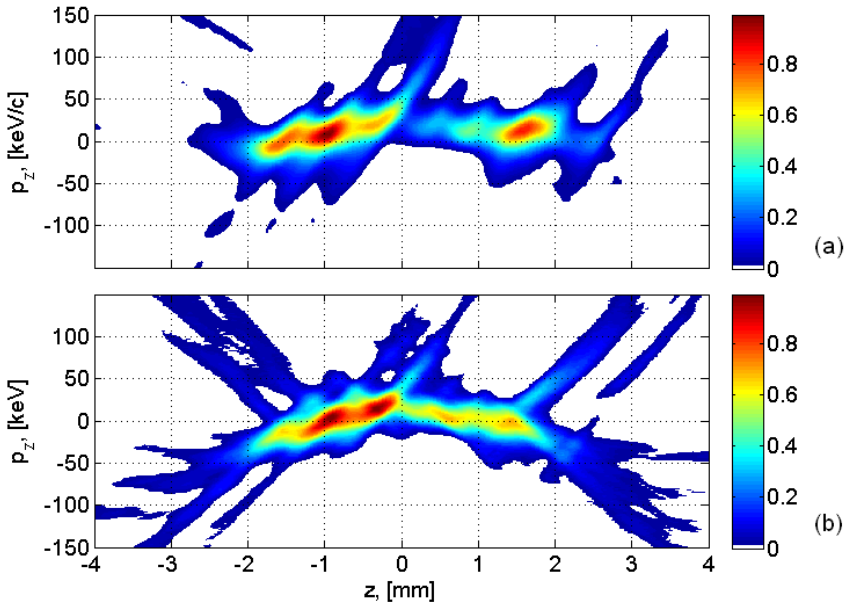

Fig. 8.40: Reconstruction results of the longitudinal phase space upstream the booster cavity for 20 pC bunch charge using momentum measurements in the HEDA1 (a) and HEDA2 (b). For the longitudinal coordinate a bin size of 0.05 mm was used to reconstruct both phase spaces.

The corresponding calculated current profiles are shown in Fig. 8.41 together with the temporal laser profile used for these measurements. Despite of the shapes of both current profiles are similar, they are far away from the structure of the temporal laser profile. Nevertheless, the temporal structure of the laser pulse can be partly recognized in the reconstructed longitudinal phase spaces shown in Fig. 8.40.

Less consistency, compared to the flat-top case, Fig. 8.31, can be explained by the much stronger modulations in the temporal laser profile, which cause significant space charge forces for each micro bunch and smear out the temporal laser structure. Also the bad temporal resolution in the reconstruction is expected from the worse momentum resolution of about 12 keV/c in these measurements compared to the flat-top case, where it was about 5 keV/c, Table 8.2.

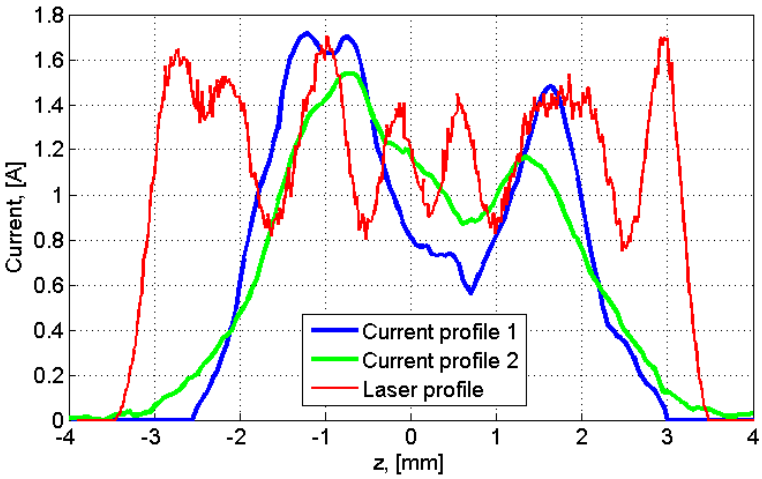

Fig. 8.41: Current profiles calculated from the reconstructed phase spaces shown in Fig. 8.40 (a) – the blue curve, in (b) – the green curve, and the corresponding measured temporal laser profile, the red curve, flipped as compared with Fig. 8.1. The laser profile was scaled vertically to have the same maximum as the first current profile.

Results of the tomographic reconstructions using the same temporal laser profile for the case of 1 nC bunch charge are shown in Fig. 8.42. 33 and 37 momentum projections were used for these reconstructions in the HEDA1 and the HEDA2 sections, respectively, with the booster RF phase step of 1 degree.

The current profiles calculated from the reconstructed longitudinal phase spaces are shown in Fig. 8.43 together with the measured temporal laser profile. The temporal structure of the laser pulse is completely smeared out for this case and cannot be seen in the longitudinal structure of the electron bunch.

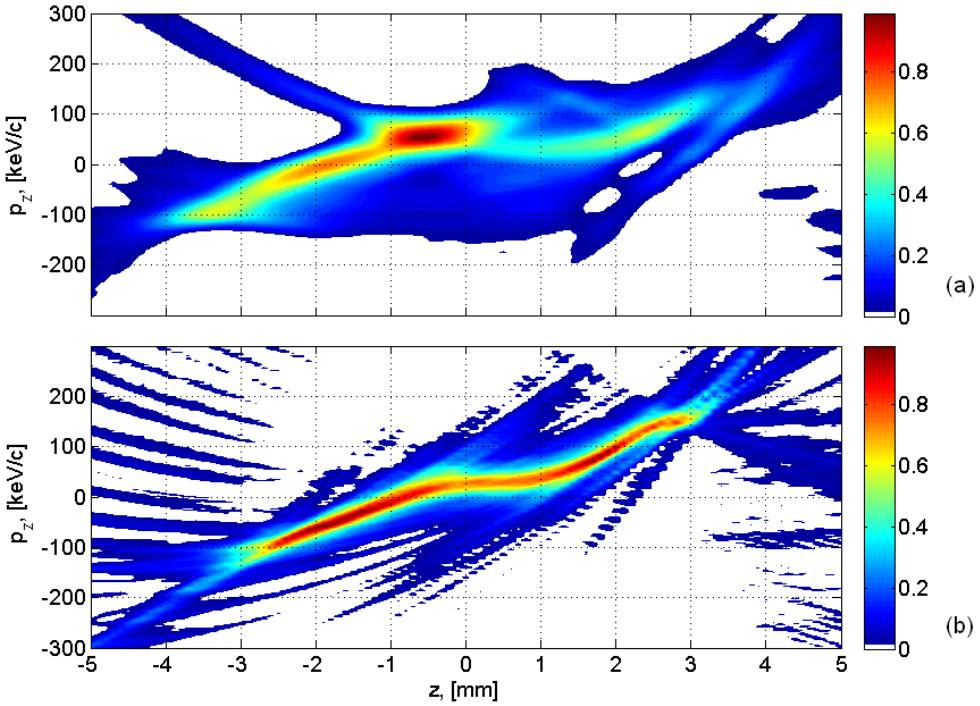

Fig. 8.42: Reconstruction results of the longitudinal phase space upstream the booster cavity for 1 nC bunch charge using momentum measurements in the HEDA1 (a) and HEDA2 (b). For the longitudinal coordinate a bin size of 0.1 mm was used to reconstruct both phase spaces.

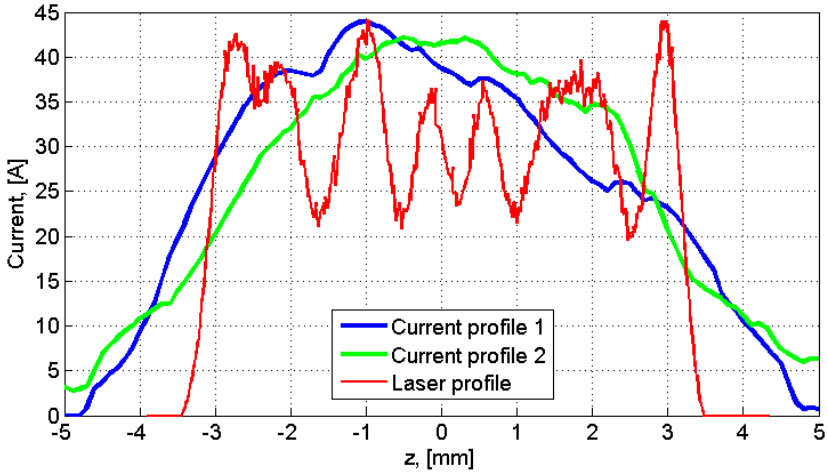

Fig. 8.43: Current profiles calculated from the reconstructed phase spaces shown in Fig. 8.42 (a) – the blue curve, in (b) – the green curve, and the corresponding measured temporal laser profile, the red curve, flipped as compared with Fig. 8.1. The laser profile was scaled vertically to have the same maximum as the first current profile.

8.5 Summary

Measurements of the longitudinal phase space using tomographic technique were performed at PITZ for three temporal laser profiles and several bunch charges. For the tomographic reconstruction the ART algorithm was used with acceleration model, described in section 6.2, which should give in result the electron bunch longitudinal phase space upstream the booster cavity. The ART algorithm was applied with 100 iteration steps starting from zero initial guess. This is sufficient for a good convergence, but in some cases the ART algorithm produces a lot of artifacts in the reconstructed phase spaces.

In most cases the reconstructed longitudinal phase spaces from the HEDA2 data show more details, for example, for 20 pC bunch charge and flat-top temporal laser profile. The phase space reconstructed from the HEDA2 data looks more narrow along the momentum axis than the one from the HEDA1 data. This effect can be explained by resolution, i.e. the dispersion at the HEDA2 observation screen is 0.905 m, what is 1.5 times higher than for the HEDA1 screen with a dispersion of 0.6 m. Another point is that for the used setups of optical readout one pixel of the camera used corresponds to about 110 μm at the observation screen of HEDA1 and about 64 μm at the observation screen of HEDA2. As a result, the measurement data for the HEDA2 case should have about 2.6 times higher precision than for HEDA1, assuming good beam transport optimization for the high momentum resolution in both dispersive sections. In the case of not perfect optimization the result from the HEDA2 data can be similar to the result from the HEDA1 or even worse.

A two hills structure of the bunch was observed for the maximum extractable charge of 700 pC generated with the Gaussian temporal laser profile. This effect can be explained by the strong space charge forces during charge emission from the photocathode.

For the case of flat-top temporal laser profile and 20 pC bunch charge the longitudinal structure of the reconstructed longitudinal phase space is in good agreement with the temporal laser profile including small deviation. For 100 pC this temporal structure is already less pronounced, the space charge forces start to smear out the longitudinal structure. And finally, for 1 nC charge this structure cannot be seen at all.

For the strong modulated temporal laser profile the corresponding charge density modulation in the bunch can be seen for the 20 pC bunch charge. And for 1 nC bunch charge this modulation is smeared out according to tomographic reconstructions.

The further analysis of the measurement data from HEDA1 which includes bunch longitudinal profile, slice energy spread and longitudinal emittance calculation can be found in Appendix B. In Table 8.3 results of the measured electron bunch parameters using the tomographic technique are summarized for the HEDA1 section momentum measurements.

Table 8.3: The measured electron bunch parameters.

Temporal laser profile	Laser FWHM, ps	Bunch charge, nC	Long. emittance, mm keV/c	RMS momentum spread, keV/c	RMS bunch length, mm
Gauss	2.8	0.02	1 ± 2	28 ± 3	0.2 ± 0.1
Gauss	2.8	0.70	45 ± 60	86 ± 35	1.3 ± 0.3
Flat-top	17.5	0.02	10 ± 7	10 ± 5	1.1 ± 0.1
Flat-top	17.5	1.00	87 ± 62	47 ± 22	2.1 ± 0.3
Modulated	21.4	0.02	27 ± 20	21 ± 12	1.3 ± 0.2
Modulated	21.4	1.00	103 ± 60	73 ± 20	2.1 ± 0.3

For these calculations a 20% of the charge was cut from the tails of the phase space distributions. The error of the RMS momentum spread measurements was estimated from the vertical beam size at the HEDA1 reference screen High1.Scr5 according Eq. (3.3). The error of the bunch length measurements was estimated according Eq. (6.13) using the already known error for the momentum measurements, Table 8.2, and the slice momentum spread calculated from the reconstructed phase space. The error of the longitudinal emittance calculation δ_ε was estimated as a sum of the three components:

$$\delta_\varepsilon = \sigma_l \cdot \delta_p + \sigma_p \cdot \delta_l + \delta_p \cdot \delta_l, \tag{8.1}$$

the RMS bunch length σ_l multiplied by the momentum measurement error δ_p, the RMS slice momentum spread σ_p multiplied by the error of the length measurement δ_l and multiplication of the momentum and length measurement errors.

Conclusions and Outlook

Two methods for longitudinal phase space measurements were presented and described in detail in this thesis: one using an RF deflector and the second one applying the tomographic technique to momentum measurements at different booster RF phases.

The RF deflector was reviewed in the thesis as a diagnostic device for various types of electron bunch measurements at PITZ. These measurements include: electron bunch temporal profile measurements, longitudinal phase space measurements and slice emittance measurements. Simulations for each type of measurements were performed and the expected resolutions were estimated. Simulations show reliable results and high momentum and longitudinal resolutions. For example, for longitudinal phase space measurements of 1 nC bunch charge the momentum resolution is expected to be better than 10 keV/c and the temporal resolution to be better than 0.3 ps. For the smaller charge is expected to have better momentum and temporal resolutions due to smaller transverse beam sizes.

Despite the fact that the transverse deflecting structure (TDS) is installed in the PITZ beamline since the end of 2011, the cavity is not in operation up to now. Due to safety limitation the delivered modulator for the TDS is not allowed to be put into operation. A new modulator is currently ordered and should be delivered to PITZ in autumn of 2014.

Additionally to the RF deflector, the electron bunch longitudinal phase space can be measured at PITZ using a tomographic technique. Such a technique was described and its application to the electron bunch longitudinal phase space measurements was introduced. Using the acceleration model of the booster cavity one can perform tomographic reconstruction upstream the booster based on momentum distribution measurements downstream. Applying the acceleration model to the reconstructed phase space the longitudinal phase space distribution downstream the booster cavity can be obtained as well. Simulations of measurements with the tomographic technique were performed with two temporal laser profiles and two electron bunch charges. The results of the simulations are consistent as well as they show high temporal resolution, comparable with the simulations of measurements using an RF deflector.

For the tomographic reconstruction the ART algorithm was used, which in some cases leads to a lot of additional artifacts in the reconstructed images. These artifacts can be avoided by using others reconstruction algorithms, for example, the maximum entropy algorithm (MENT). But a first test of the MENT algorithm didn’t show convergence with the iteration number and showed density oscillations in the reconstructed phase space. To use the MENT algorithm for a detailed reconstruction of the longitudinal phase space significantly more detailed studies are required.

Experimental measurements of the longitudinal phase space were done at the PITZ facility using the tomographic technique with the ART reconstruction algorithm for three temporal laser profiles and several bunch charges. The resolution of the method is sufficient to resolve non-flatness of the temporal laser profile in the reconstructed longitudinal phase space. This was shown in the measurements of the bunch with a small charge generated by a laser pulse with a slightly modulated flat-top temporal profile.

The TDS was originally installed at PITZ as a prototype of the RF deflecting structure for the European XFEL to test its efficiency and performance beforehand. Meanwhile, the TDS at PITZ is also planned to be used for the studies of electron bunch interactions with a plasma [48], [49]. The main goal of these studies is to observe an energy modulation in the electron bunch induced by the interaction with the plasma. Unfortunately, the tomographic technique described in the thesis cannot be used for this task, because the plasma cell will be installed downstream the booster cavity and therefore the resulting longitudinal phase space distribution cannot be rotated. Anyhow, the tomographic technique can be used for other studies at PITZ such as the characterization of the bunch with low charge, bunch longitudinal profile measurements and longitudinal phase space measurements while other techniques are not available yet. Also the tomographic technique can be used to control the longitudinal phase space in case a third harmonic cavity will be installed at PITZ in future for longitudinal phase space linearization. Compared with the measurements using the TDS, tomographic measurements are not direct measurements, i.e. some additional mathematical data treatments are needed for interpretation. But, on the other hand, with tomographic reconstructions the longitudinal phase space upstream the booster cavity can be obtained.

Appendix A

First-Order sector bending magnet transport matrix

The beam transport through a pure sector magnet with bending along the x axis and with a normalized field gradient in the dispersive direction n can be represented as a six-dimensional transport matrix [50]:

$$\begin{bmatrix} \cos k_x L & \frac{1}{k_x}\sin k_x L & 0 & 0 & 0 & \frac{h}{{k_x}^2}(1-\cos k_x L) \\ -k_x \sin k_x L & \cos k_x L & 0 & 0 & 0 & \frac{h}{k_x}\sin k_x L \\ 0 & 0 & \cos k_y L & \frac{1}{k_y}\sin k_y L & 0 & 0 \\ 0 & 0 & -k_y \sin k_y L & \cos k_y L & 0 & 0 \\ \frac{h}{k_x}\sin k_x L & \frac{h}{{k_x}^2}(1-\cos k_x L) & 0 & 0 & 1 & -\frac{h^2}{{k_x}^3}(k_x L-\sin k_x L)+\frac{L}{\gamma^2} \\ 0 & 0 & 0 & 0 & 0 & 1 \end{bmatrix}$$

where $h = {}^{1}/_{\rho}$, ${k_x}^2 = (1-n)h^2$, ${k_y}^2 = nh^2$, $\alpha = hL$ is the bending angle, L is the path length in the magnet, γ is the relativistic factor, ρ is the bending radius and the normalized field gradient in the dispersive direction $n = \frac{\rho}{B}\frac{dB_y}{dx}$.

In case of a bending magnet without gradient in the dispersive direction, i.e. $n = 0$, the transport matrix is simplified:

$$\begin{bmatrix} \cos\alpha & \rho\sin\alpha & 0 & 0 & 0 & \rho(1-\cos\alpha) \\ -\frac{1}{\rho}\sin\alpha & \cos\alpha & 0 & 0 & 0 & \sin\alpha \\ 0 & 0 & 1 & L & 0 & 0 \\ 0 & 0 & 0 & 1 & 0 & 0 \\ \sin\alpha & \rho(1-\cos\alpha) & 0 & 0 & 1 & -\rho(\alpha-\sin\alpha)+\frac{L}{\gamma^2} \\ 0 & 0 & 0 & 0 & 0 & 1 \end{bmatrix}.$$

Appendix B

Further analysis of the measurement data

In the following section further analyses of the measurement data were performed for the HEDA1 measurements and two bunch charges for each temporal laser profile. The acceleration model was used to reconstruct longitudinal phase space in front of the booster cavity. Bunch RMS momentum spread, current distribution, RMS bunch length, slice RMS momentum spread and longitudinal RMS emittance were calculated.

A check of the reconstructed data reliability was done by comparing the momentum distribution of the reconstructed longitudinal phase space with the measured momentum distribution downstream the gun at the LEDA section. In case of perfect and correct reconstruction these distributions should coincide.

Gaussian temporal laser profile and 20 pC bunch charge

In Fig. B.1 the reconstructed longitudinal phase space, momentum distribution, current distribution and slice RMS momentum spread are shown for a 20% charge cut applied to the reconstructed phase space. In the image of the longitudinal phase space for the vertical axis “n” means number of momentum bins used for the reconstruction and for the horizontal axis “n” means the number of bins used for the longitudinal coordinate. For this reconstructed phase space 54 momentum bins and 201 longitudinal bins were used to perform tomographic reconstruction. Calculated from the reconstructed longitudinal phase space the longitudinal RMS emittance is 1.2 mm keV/c, the RMS momentum spread is 28 keV/c and the RMS bunch length is 0.2 mm.

Fig. B.2 shows the measured momentum distribution at the LEDA section downstream the gun and the momentum distribution calculated from the reconstructed longitudinal phase space. From this plot one can see that the reconstructed and the measured electron bunch momentum distribution are quite different, the RMS size of the reconstructed one is 28 keV/c and the RMS size of the measured one is only 11 keV/c. Possible reason for the discrepancy is the space charge forces which increase the momentum spread in the bunch during the bunch propagation from the LEDA section to the HEDA1 section where the measurements for the tomographic reconstructions are performed.

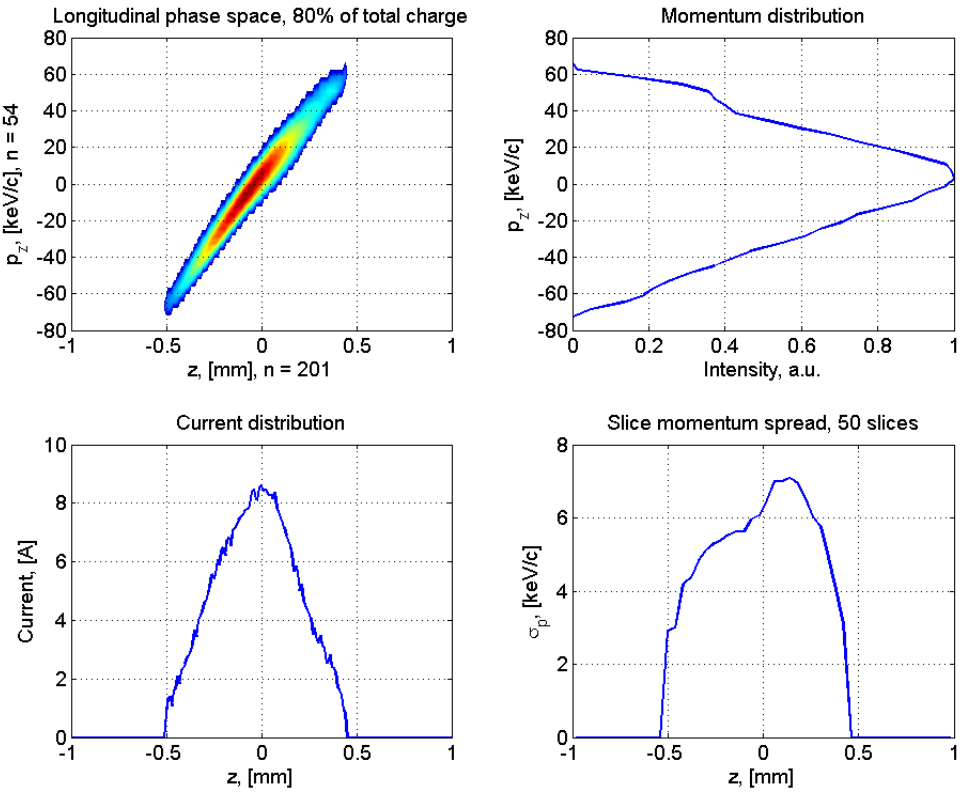

Fig. B.1: Reconstructed longitudinal phase space, momentum distribution, current distribution and slice momentum spread for 20 pC bunch charge. 20% of the charge was cut from the tails of the phase space distribution.

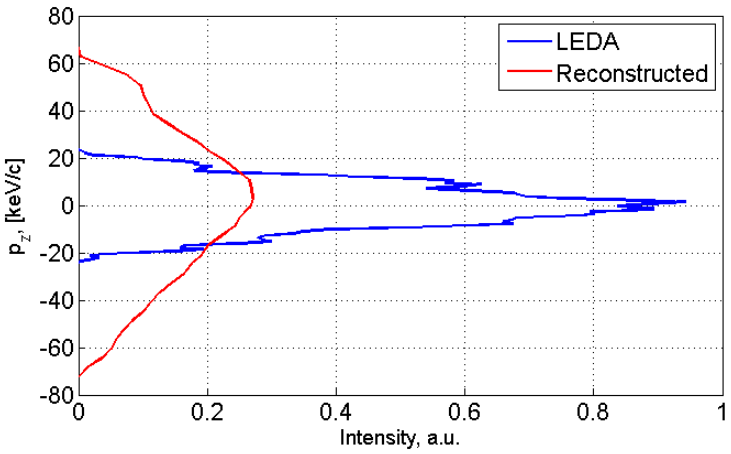

Fig. B.2: Measured momentum distribution at the LEDA section downstream the gun, the blue curve, and calculated momentum distribution from the reconstructed longitudinal phase space, the red curve. The distributions are normalized to have the same integral.

Gaussian and 700 pC bunch charge

In Fig. B.3 the reconstructed longitudinal phase space, momentum distribution, current distribution and slice momentum spread are shown for a 20% charge cut applied to the reconstructed phase space.

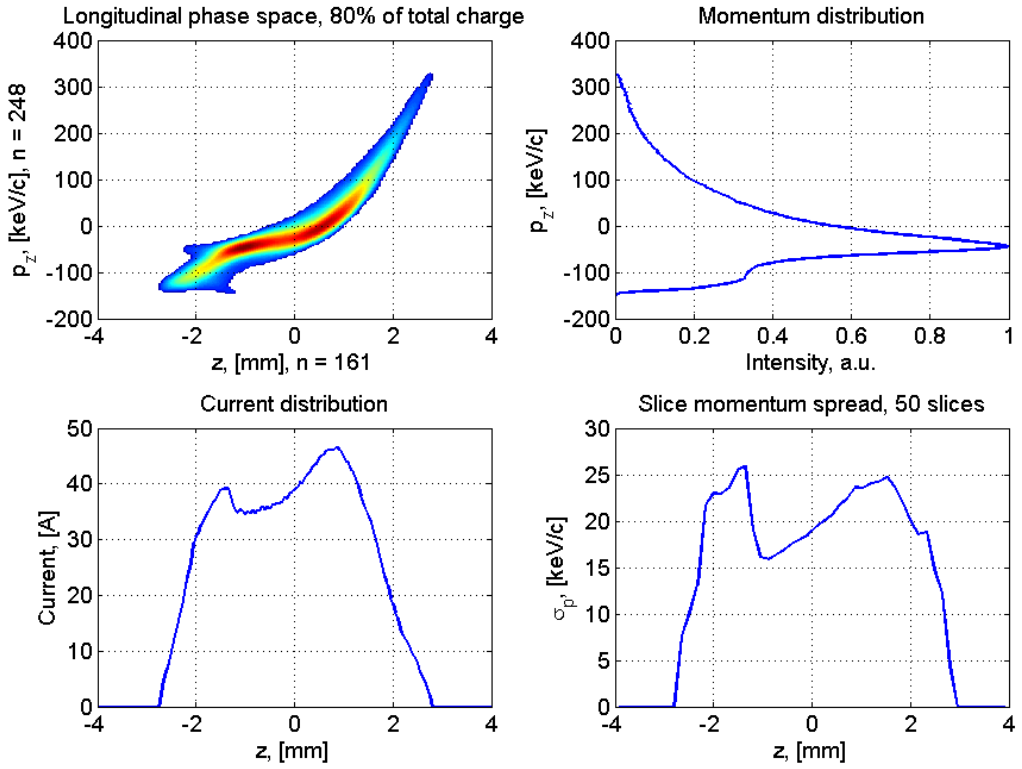

Fig. B.3: Reconstructed longitudinal phase space, momentum distribution, current distribution and slice momentum spread for 700 pC bunch charge. 20% of the charge was cut from the tails of the phase space distribution.

Calculated from the reconstructed longitudinal phase space the longitudinal RMS emittance is 45 mm keV/c, the RMS momentum spread is 86 keV/c and the RMS bunch length is 1.3 mm.

Fig. B.4 shows the measured momentum distribution at the LEDA section downstream the gun and the momentum distribution calculated from the reconstructed longitudinal phase space. From this plot one can see that reconstructed and measured electron bunch momentum distribution are quite different, the RMS size of the reconstructed one is 86 keV/c and the RMS size of the measured one is about 10 keV/c.

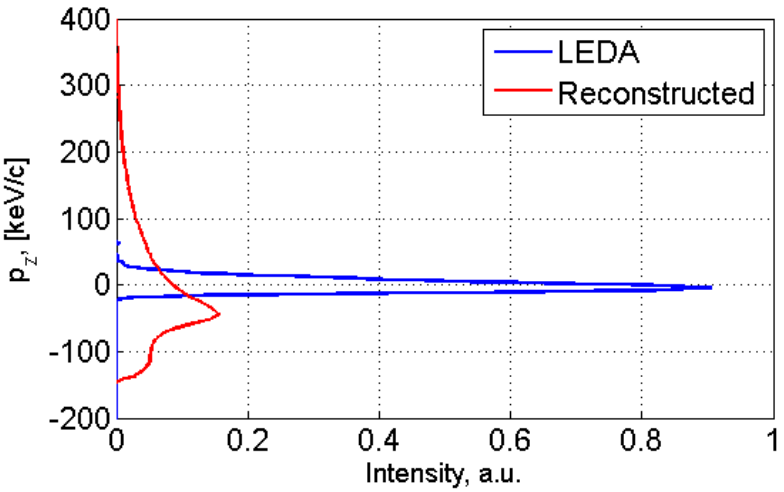

Fig. B.4: Measured momentum distribution at the LEDA section downstream the gun, the blue curve, and calculated momentum distribution from the reconstructed longitudinal phase space, the red curve. The distributions are normalized to have the same integral.

The same as for 20 pC case the discrepancy can be explained by the space charge forces which increase the momentum spread in the bunch during propagation. For the bunch charge of 700 pC this effect is expected to be much stronger. It is not clear why the measured RMS momentum spread for this case is smaller than for the 20 pC bunch charge. From the numerical simulation for the 700 pC bunch charge the bunch RMS momentum spread downstream the gun at 2.5 m is about 46 keV/c.

Flat-top temporal laser profile and 20 pC bunch charge

In Fig. B.5 the reconstructed longitudinal phase space, momentum distribution, current distribution and slice momentum spread are shown for a 20% charge cut applied to the reconstructed phase space (154 momentum bins and 241 longitudinal bins are used for reconstruction).

Calculated from the reconstructed longitudinal phase space the longitudinal RMS emittance is 10 mm keV/c, the RMS momentum spread is 10 keV/c and the RMS bunch length is 1.1 mm.

Fig. B.6 shows the measured momentum distribution at the LEDA section downstream the gun and the momentum distribution calculated from the reconstructed longitudinal phase space. From this plot one can see that the reconstructed and the measured electron bunch momentum distribution are close, RMS size of the reconstructed one is 10 keV/c and RMS size of the measured one is 8 keV/c. Compared to the Gaussian laser temporal profile, here the bunch is longer and as a result the longitudinal space charge forces are smaller.

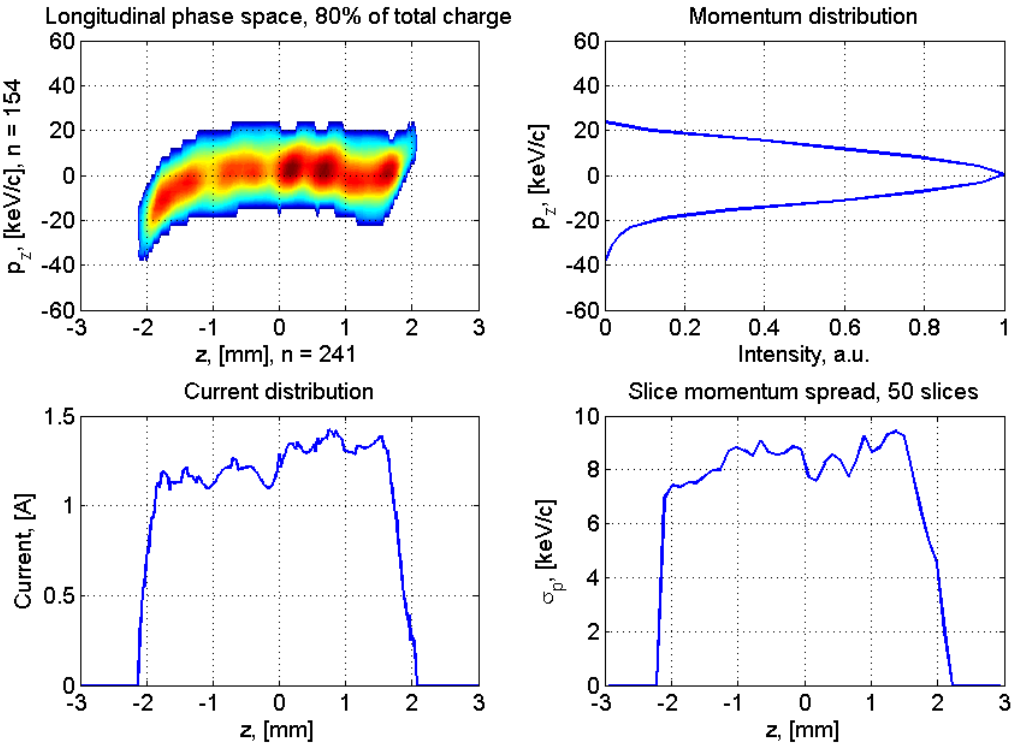

Fig. B.5: Reconstructed longitudinal phase space, momentum distribution, current distribution and slice momentum spread for 20 pC bunch charge. 20% of charge was cut from the tails of the phase space distribution.

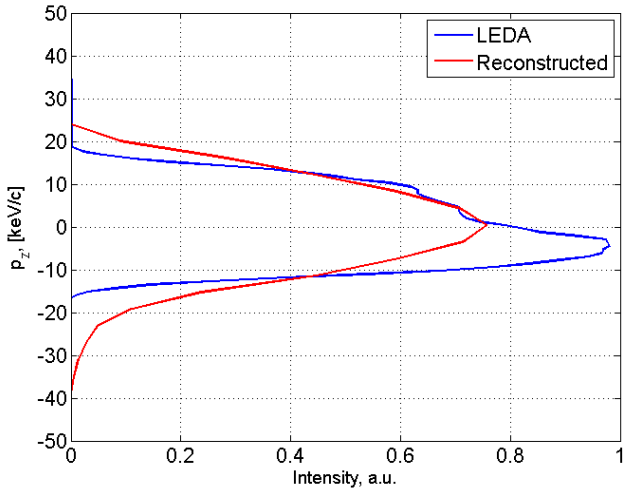

Fig. B.6: Measured momentum distribution at the LEDA section downstream the gun, the blue curve, and calculated momentum distribution from the reconstructed longitudinal phase space, the red curve. Distributions are normalized to have the same integral.

Flat-top temporal laser profile and 1 nC bunch charge

In Fig. B.7 the reconstructed longitudinal phase space and calculated momentum distribution, current distribution and slice momentum spread are shown for a 20% charge cut applied to the reconstructed phase space. Calculated from the reconstructed longitudinal phase space the longitudinal RMS emittance is 83 mm keV/c, the RMS momentum spread is 47 keV/c and the RMS bunch length is 2.1 mm.

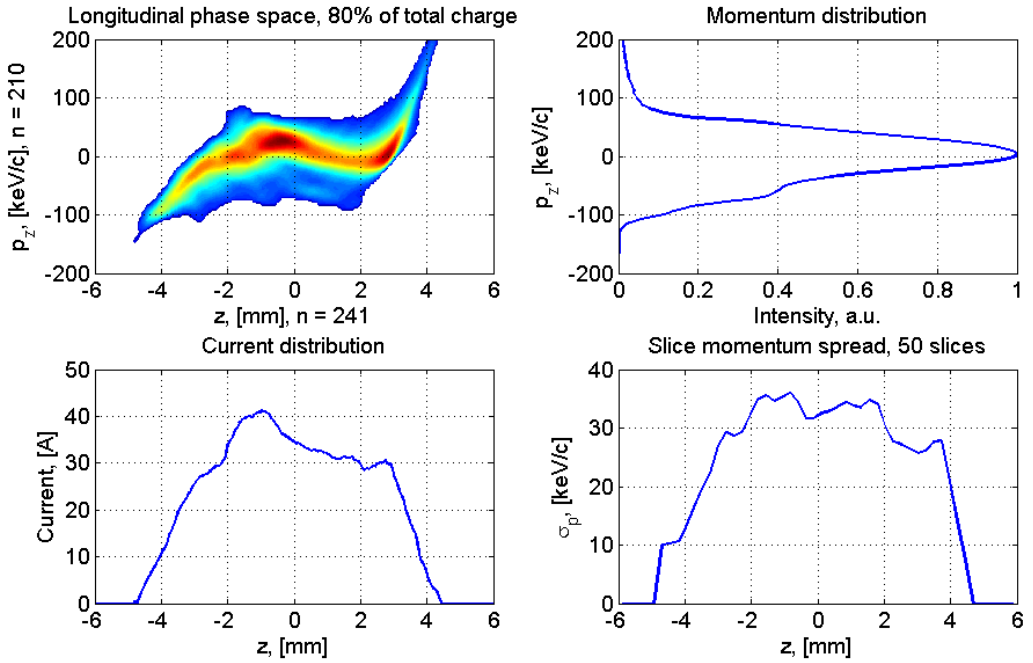

Fig. B.7: Reconstructed longitudinal phase space, momentum distribution, current distribution and slice momentum spread for 1 nC bunch charge. 20% of charge was cut from the tails of the phase space distribution.

Fig. B.8 shows the measured momentum distribution at the LEDA section downstream the gun and momentum distribution calculated from the reconstructed longitudinal phase space. From this plot one can see that the reconstructed and the measured electron bunch momentum distribution are different, the RMS size of the reconstructed one is 51 keV/c and the RMS size of the measured one is 18 keV/c. Compared to the previous case, the space charge forces is stronger here and increase the momentum spread in the bunch during propagation from the LEDA section to the HEDA1 section.

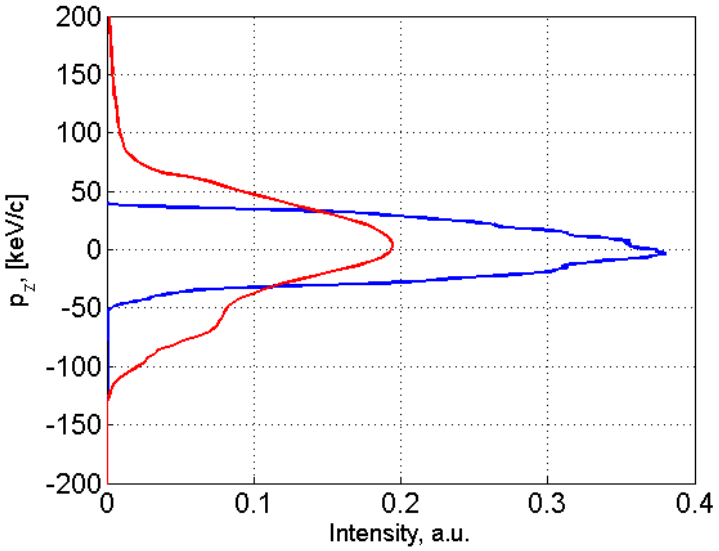

Fig. B.8: Measured momentum distribution at the LEDA section downstream the gun, blue curve, and calculated momentum distribution from the reconstructed longitudinal phase space, red curve. The distributions are normalized to have the same integral.

Modulated flat-top temporal laser profile and 20 pC bunch charge

In Fig. B.9 the reconstructed longitudinal phase space and calculated momentum distribution, current distribution and slice momentum spread from the reconstructed phase space are shown with a charge cut of 20% applied. Calculated from the reconstructed longitudinal phase space the longitudinal RMS emittance is 27 mm keV/c, the RMS momentum spread is 21 keV/c and the RMS bunch length is 1.3 mm.

Fig. B.10 shows the measured momentum distribution at the LEDA section downstream the gun and the momentum distribution calculated from the reconstructed longitudinal phase space. From this plot one can see that the reconstructed and the measured electron bunch momentum distribution are in good agreement, the RMS size of the reconstructed one is 20 keV/c and the RMS size of the measured one is 13 keV/c. Discrepancy can be explained by the space charge forces in each micro bunch within the whole bunch. Each micro bunch behaves like short Gaussian bunch and its momentum spread is increasing due to the space charge forces during propagation from the LEDA section to the HEDA1 section.

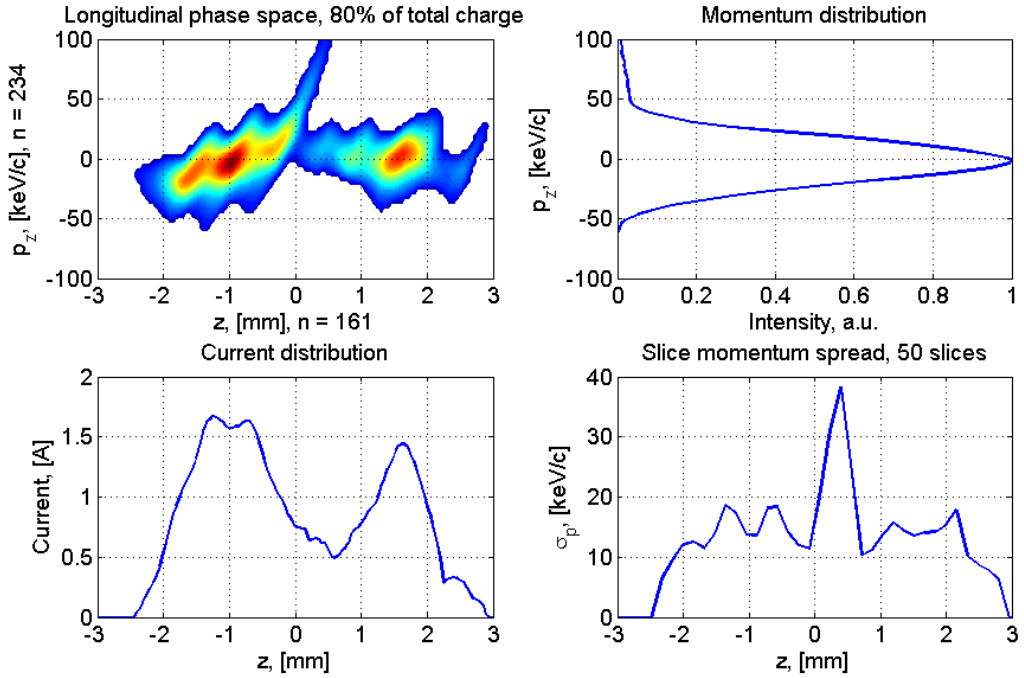

Fig. B.9: Reconstructed longitudinal phase space, momentum distribution, current distribution and slice momentum spread for 20 pC bunch charge. 20% of charge was cut from the tails of the phase space distribution.

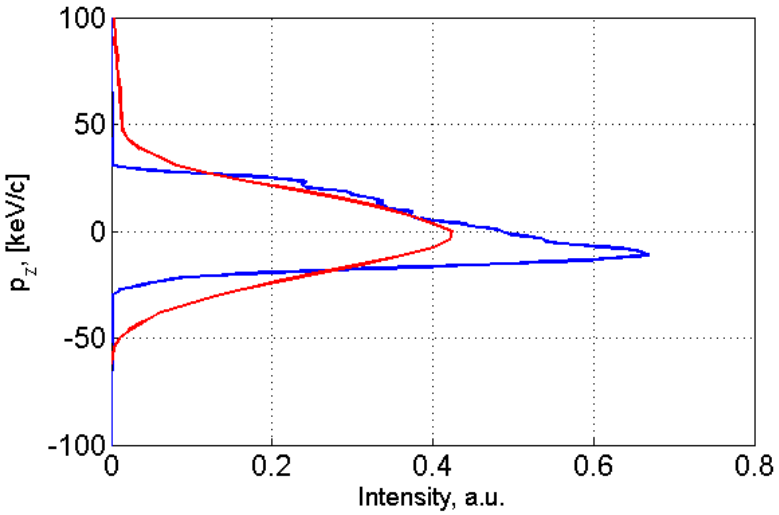

Fig. B.10: Measured momentum distribution at the LEDA section downstream the gun, blue curve, and calculated momentum distribution from the reconstructed longitudinal phase space, red curve. The distributions are normalized to have the same integral.

Modulated flat-top temporal laser profile and 1 nC bunch charge

In Fig. B.11 are shown the reconstructed longitudinal phase space and calculated momentum distribution, current distribution and slice momentum spread from the reconstructed phase space with applied 20% charge cut.

Calculated from the reconstructed longitudinal phase space the longitudinal RMS emittance is 103 mm keV/c, the RMS momentum spread is 73 keV/c and the RMS bunch length is 2.1 mm.

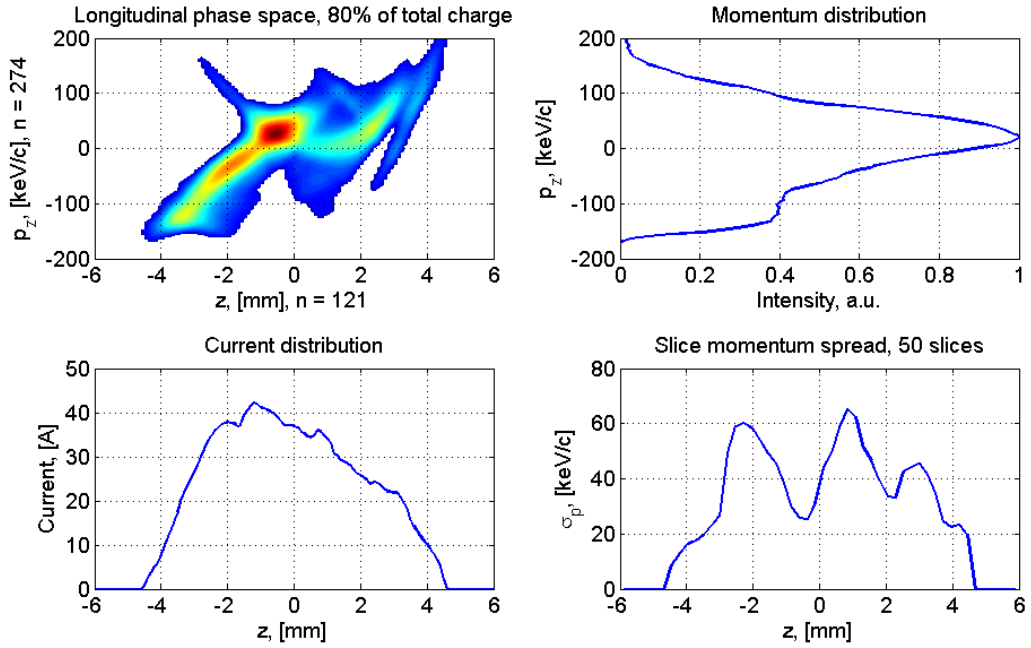

Fig. B.11: Reconstructed longitudinal phase space, momentum distribution, current distribution and slice momentum spread for 1 nC bunch charge. 20% of charge was cut from the tails of the phase space distribution.

Fig. B.12 shows the measured momentum distribution at the LEDA section downstream the gun and momentum distribution calculated from the reconstructed longitudinal phase space. From this plot one can see that the reconstructed and the measured electron bunch momentum distribution are much different, the RMS size of the reconstructed one is 73 keV/c and the RMS size of the measured one is 18 keV/c. For this case the space charge is much stronger than for 20 pC bunch charge. As a result the reconstructed momentum distribution is much wider than the measured one at the LEDA section.

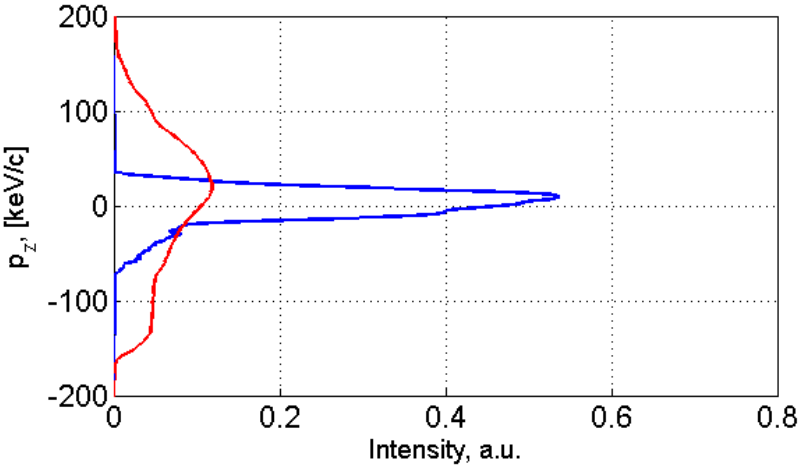

Fig. B.12: Measured momentum distribution at the LEDA section downstream the gun, blue curve, and calculated momentum distribution from the reconstructed longitudinal phase space, red curve. The distributions are normalized to have the same integral.

Bibliography

[1]. P. Schmueser, M. Dohlus and J. Rossbach, *Ultraviolet and Soft X-Ray Free-Electron Lasers: Introduction to Physical Principles, Experimental Results, Technological Challenges*. Springer Tracts in Modern Physics, Springer, 1st ed., 2008.

[2]. M. Hogan et al., Measurements of high gain and intensity fluctuations in a SASE free-electron laser. *Phys. Rev. Lett.* 80, 289 (1998) 109.

[3]. M. Hogan et al., Measurements of gain larger than 10^5 at 12 μm in a self-amplified spontaneous-emission free-electron laser. *Phys. Rev. Lett.* 81, 4867 (1998) 109.

[4]. F. Stephan, C. H. Boulware, M. Krasilnikov, J. Bähr et al., Detailed characterization of electron sources yielding first demonstration of European X-ray Free-Electron Laser beam quality. *Phys. Rev. ST Accel. Beams* 13, 020704 (2010).

[5]. The Technical Design Report (TDR) of the European XFEL. http://xfel.desy.de/

[6]. L. Stayakov. *Characterization of the transverse phase space at the photo-injector test facility in DESY, Zeuthen site.* PhD thesis 2012. Hamburg University.

[7]. J. Roensch, *Investigations on the electron bunch distribution in the longitudinal phase space at a laser driven RF electron source for the European X-FEL.* PhD thesis 2009. Hamburg University.

[8]. M. Mahgoub et al., Application and design of the streak and TV readout, systems at PITZ, *Proceedings of FEL2011.*

[9]. H. Loos et al., "Longitudinal phase space tomography at the SLAC Gun Test Facility and the BNL DUV-FEL", *Nucl. Instrum. Meth. A* 528 (2004) 189.

[10]. H. Wiedmann, *Particle accelerator physics*, Springer, 3rd edition. 1999.

[11]. M. Altarelli et al., DESY, Hamburg, Report No. DESY 2006-097, 2006.

[12]. G. Asova et al., Implementation of tomographic diagnostics at PITZ. *Proceedings of DITANET2011.*

[13]. G. Asova, *Tomography of the electron beam transverse phase space at PITZ,* PhD thesis. INRNE, Bulgarian Academy of Sciences, Sofia, 2012.

[14]. I. Will, G. Koss, I. Templin, The upgraded photocathode laser of the TESLA Test Facility, *Nucl. Instrum. Meth. A* 541 467-477, 2005.

[15]. I. Will and G. Klemz, Generation of flat-top picosecond pulses by coherent pulse stacking in a multicrystal birefringent filter. *Opt. Express* 16, 14922 (2008).

[16]. S. Lederer et al., Investigation on the increased lifetime of the photocathodes at FLASH and PITZ. *Proceedings of PAC2009.*

[17]. M. Haenel, *Experimental investigations on the influence of the photocathode laser pulse parameters on the electron bunch quality in an RF - photoelectron source*. PhD thesis 2010. Hamburg University.
[18]. V. Paramonov et al., The PITZ booster cavity – a prototype for the ILC positron injector cavities. *Proceedings of PAC2005.*
[19]. V. Paramonov et al., The PITZ CDS booster cavity RF tuning and start of conditioning. *Proceedings of LINAC2010.*
[20]. S. Rimjaem et al., Comparison of different radiators used to measure the transverse characteristics of low energy electron beams at PITZ, *Proceedings of DIPAC2011*, TUPD54.
[21]. L. Staykov et al., Measurement of the projected normalized transverse emittance at PITZ, *Proceedings of FEL2007,* MOPPH055.
[22]. S. Khodyachykh et al., Design of multipurpose dispersive section at PITZ, *Proceeding of FEL2006.*
[23]. Ye. Ivanisenko, *Investigation of slice emittance using an energy-chirped electron beam in a dispersive section for photo injector characterization at PITZ.* PhD thesis 2012. Hamburg University.
[24]. S. Rimjaem et al., Physics and technical design for the second high energy dispersive section at PITZ, *Proceedings of DIPAC2009*, MOPD26.
[25]. P. Emma et al., A transverse RF Deflecting Structure for Bunch Length and Phase Space Diagnostics. LCLS-TN-00-12. 2000.
[26]. M. Roehrs, C. Gerth, H. Schlarb, Measurement of the slice energy spread induced by a transverse deflecting RF structure at FLASH, *Proceedings of FEL2006.*
[27]. D. Alesini et al., RF deflector design and measurements for the longitudinal and transverse phase space characterization at SPARC. *Nucl. Instrum. Meth. A* 568 (2006) 488 - 502.
[28]. C. Vaccarezza et al., Slice emittance measurements at SPARC photoinjector with a RF deflector, *Proceedings of EPAC2008.*
[29]. O. H. Altenmueller, R. R. Larsen, and G. A. Loew, Investigations of Traveling-Wave Separators for the Stanford Two-Mile Linear Accelerator, *The Review of Scientific Instruments,* Vol. 35, Number 4, April 1964.
[30]. M. Roehrs, C. Gerth, Electron beam diagnostics with transverse deflecting structures at the European X-ray Free Electron Laser, *Proceedings of FEL2008.*
[31]. L. Kravchuk et al., Layout of the PITZ transverse deflecting system for longitudinal phase space and slice emittance measurements, *Proceedings of LINAC2010.*
[32]. D. Malyutin et al., Commissioning of new diagnostic devices at PITZ, *Proceedings of RuPAC2012.* WEPPD057.
[33]. D. Denisenko, V. Paramonov, Transverse Deflecting Structures parameters study, *Proceedings of RuPAC 2008.*

[34]. M. Roehrs, *Investigations of the Phase Space Distribution of Electron Bunches at the FLASH-Linac Using a Transverse Deflecting Structure.* PhD thesis 2008. Hamburg University.
[35]. D. Alesini, RF deflector based sub-ps beam diagnostics: Application to FEL and advanced accelerators, *Int. J. Mod. Phys. A* 22, 3693 (2007).
[36]. W. K. H. Panofsky, W. A. Wenzel, Some consideration concerning the transverse deflection of charged particles in radio-frequency field. *Rev. Sci. Instrum.,* 27:967, 1956.
[37]. M. Cornacchia and P. Emma, Transverse to longitudinal emittance exchange, *Phys. Rev. ST Accel. Beams* 5, 074401.
[38]. K. Floettmann, A space charge tracking code - ASTRA, http://desy.de/~mpyflo/
[39]. C. Behrens, C. Gerth, On the limitations of longitudinal phase space measurements using a transverse deflecting structure, *Proceedings of DIPAC2009.*
[40]. C. Behrens, C. Gerth, Measurement of the slice energy spread induced by a transverse deflecting RF structure at FLASH, *Proceedings of DIPAC2011.*
[41]. J. Radon, *On the Determination of Functions from Their Integral Values along Certain Manifolds, Medical Imaging*, IEEE Transactions on, 5(4):170–176, Dec. 1986.
[42]. A.C. Kak, M. Slaney, *Principles of Computerized Tomographic Imaging*, IEEE Press, 1979.
[43]. S. F. Gull and T. J. Newton, Maximum entropy tomography, *Appl. Opt.,* 25(1):156–160, 1986.
[44]. H. Loos, Longitudinal phase space tomography and its implementation in energy recovery linacs. *Nucl. Instrum. Meth. A* 557 (2006) 309 - 313.
[45]. M. Rehders et al., Beam dynamics studies for the generation of short SASE pulses at FLASH, *Proceedings of FEL2012*, THPD37.
[46]. B. Marchetti et al., Compression of a 20 pC e-bunch at the European XFEL for Single Spike Operation. *Accepted at Physics procedia.* 2013.
[47]. D. Malyutin et al., First results of the longitudinal phase space tomography at PITZ, *Proceedings of FEL2013.* TUPSO47.
[48]. A. Martinez de la Ossa et al., Self-modulation of long electron beams in plasma at PITZ. *AIP Conf. Proc.* 1507, 588 (2012); June 2012, Austin, Texas, USA.
[49]. M. Gross et al., Preparations for a plasma wakefield acceleration (PWA) experiment at PITZ. *Nucl. Instrum. Meth. A.* 740 (2014) 74-80.
[50]. K.L. Brown and F. Rothacker, "Third-Order TRANSPORT with MAD Input - A Computer Program for Designing Charged Particle Beam Transport Systems", *SLAC-R-530 Fermilab-Pub-98-310*, October 1998.

Acknowledgments

I would like to express my sincerest gratitude to all people who have contributed to the success of this work:

- Prof. Dr. J. Roßbach, Dr. M. Krasilnikov and Dr. F. Stephan for supervising this work;

- Prof. Dr. J. Roßbach, Dr. F. Stephan, Dr. M. Krasilnikov, Dr. T. Rublack, Dr. M. Groß, Dr. G. Asova, Dr. G. Vashchenko, Dr. M. Otevrel and G. Koukafas for thoroughly proofreading of my thesis, for their useful comments, suggestions and advices;

- Dr. M. Krasilnikov for suggesting the subject for the experimental part of the thesis, while the TDS system was not in operation;

- shift staff, technical staff and IT department of DESY in Zeuthen for doing their best for the experiments at PITZ.